VRIJE UNIVERSITEIT BRUSSEL

imec

Graduation thesis submitted in partial fulfilment of the requirements for the degree of Master in Physics and Astronomy

ELEMENTAL ANALYSIS OF SELF-SUPPORTING THIN FILMS WITH PARTICLE INDUCED X-RAY EMISSION

Tobi Vanmeerbeek

2024-2025

Under the guidance of Prof. Dr. Michael Tytgat and Dr. Johan Meersschaut

Faculty of Sciences and Bio-Engineering Sciences

Abstract

Material characterization is of great importance in various fields of research. Existing ion beam analysis methods that are used to characterize thin films exhibit certain limitations for the detection of light and similar atomic mass elements. This is for example the case in thin films containing the InGaZnO (IGZO) elemental combination. IGZO-thin films have the potential to counter the low device performances in future small-scale transistors. State of the art particle induced X-ray emission spectroscopy (PIXE) can be used to distinguish between similar mass elements and has the potential to detect low concentrations of light elements, but suffers from a continuous background. To solve these problems there is a need for new approaches to investigate semiconducting thin films with high-energy ion beams. In this thesis, the ability of state of the art PIXE to characterize IGZO and GeAsSe thin films is investigated. The work is focused on investigating potential improvements for the analysis of these types of samples using PIXE with self-supporting thin films, which has the potential to significantly reduce the background.

Contents

Chapter 1

Motivation

1.1 The importance of material characterization

Semiconductors have become an important building stone for innovative technology in today's society. The rapid need for more energy efficient, more robust and faster devices challenges the Si-based technologies of today. This led to the fall of Moore's law that scientists currently observe. Moore [1, 2] predicted in 1975 that the complexity of electrical circuits would double every two years, which caused the exponential trend that is shown in Figure 1.1. Devices became more energy

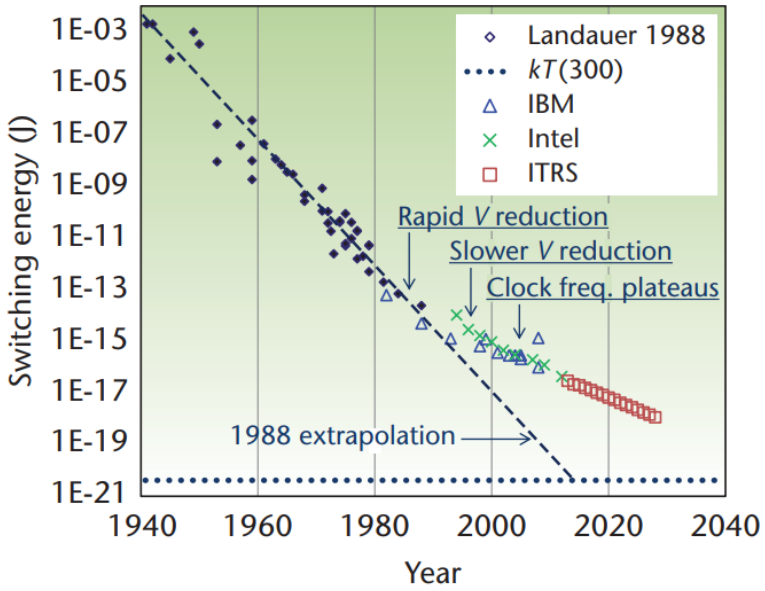

Figure 1.1: The decline of Moore's law. Taken from [3].

efficient due to the lower switching energies that were obtained by scaling down the

size of the transistors that were used in the circuits. The devices also possessed an improved clock speed. One of the reasons for the end of the exponential trend was that devices based on small scale Si-based transistors exhibited low performances [4, 5, 6]. Some of these performance problems are caused by the low electron mobility in the thin silicon conductive channels.

Scientists at R&D facilities such as Imec are investigating the performance of devices based on novel semiconducting materials that have the potential to counter the low conductivity of silicon. Thin film transistors fabricated with a thin layer of InGaZnO (IGZO) [7, 8] are components based on one of these novel materials. The influence of the relative concentrations of gallium and zinc on the performance of IGZO-based devices is still a part of modern day research [9]. This concentration ratio offers the possibility to change and tune the electron mobility. In order to quantify the concentrations of the IGZO elements, material characterization methods that can distinguish the corresponding signals are required.

On the other hand, the rise of big data impacts the demand for innovative storage systems. A three-dimensional memory with structures of large crossbar arrays has proven to be extremely efficient [10]. An example of such a 3D array is visualized in Figure 1.2. An important aspect of this memory technology is the selectors that are serially connected to their respective memory cell. These selectors are made of ovonic treshold switching (OTS) [11] materials that have a unique IV-curve. An OTS material starts in a high-resistive state when it is biased with a voltage lower than the critical voltage V_{th}. After surpassing V_{th}, the OTS material will transition to a conductive low-resistive state [11]. This principle is used in 3D memory arrays to prevent leakage currents to the unselected cells.

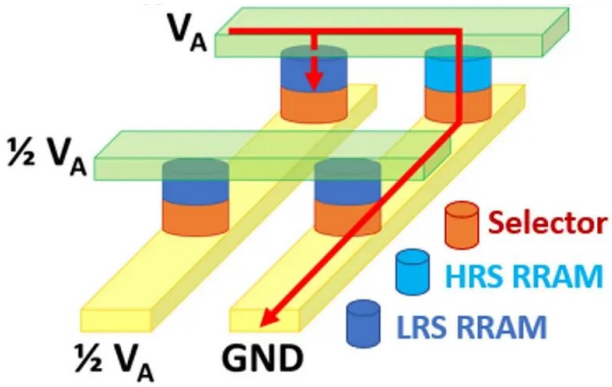

Figure 1.2: Cross-point architecture with resistive memory elements. Selected memory cell is shown in light blue while the unselected cells are dark blue. Taken from [12].

The OTS-selectors [12] of the unselected memory cells are biased with a voltage $V_{th}/2$ such that they block any leakage current. This makes the memory array more energy efficient. The OTS principle is still an active area of research and recently there has been an increased interest for GeAsSe (GAS) [11, 13, 14]. GAS exhibits a low leakage current and high endurance performance compared to other OTS materials. This is shown in Figure 1.3.

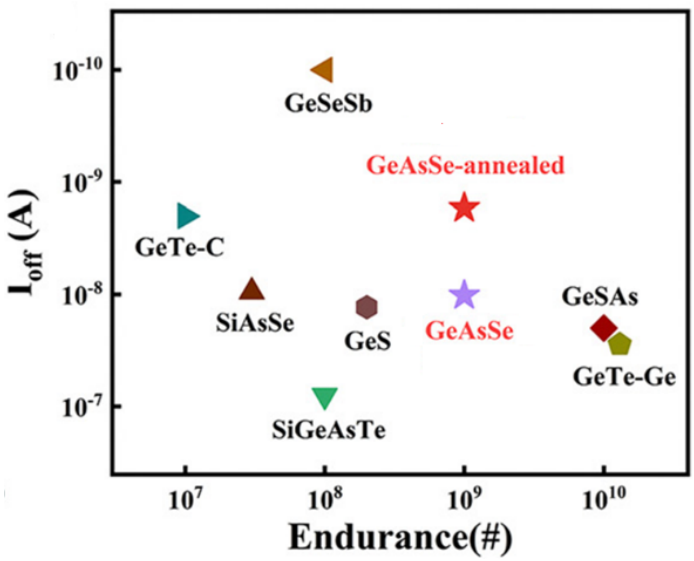

Figure 1.3: Endurance and leakage current comparison of different OTS-materials. Taken from [11].

The influence of the elemental concentrations of GAS on these properties is not yet fully understood. Material characterization is again an important part of future GAS research. IGZO and GAS thin films can thus be seen as examples of the importance of material characterization. The accuracy of the analysis is then determined by the ion beam analysis (IBA) technique used for the characterization.

1.2 Material characterization techniques

Particle induced X-ray emission spectroscopy (PIXE) [15] is an ion beam analysis technique which uses the characteristic X-rays from the elements in a target to determine the elemental composition [16]. These X-rays are created when a MeV proton beam impinges on the target under investigation. Today, PIXE has many applications in archaeology, painting dating and environmental studies [17, 18]. The goal of this work is to investigate the benefits that PIXE could offer for the semiconductor industry, in terms of sample characterization.

Currently, Rutherford backscattering spectrometry (RBS) [19] is routinely used for the characterization of thin films [20]. This technique utilizes a MeV He-ion beam to probe the elemental composition of the thin film. Here, the energy of the backscattered He-ions is used as a parameter to obtain the elemental information, but this results in poor mass resolution. This is especially important for a thin film with Ga and Zn atoms because of their similar mass. PIXE has the potential to overcome these limitations by using the characteristic X-rays of the similar atomic mass elements.

Additionally, to obtain information about the light elements inside a film, elastic recoil detection (ERD)[21] measurements are typically performed. This technique uses a heavy ion beam to eject the nuclei of different elements from the material. These nuclei are then characterized based on their energy and velocity. The current use of ERD is supported by the fact that RBS is not sensitive to light elements inside a thin film. However, PIXE has the potential to surpass the sensitivity of RBS and ERD to oxygen, Cl and other light elements.

Conventional PIXE is limited in the characterization of these light elements by an intense experimental background, which hinders the analysis of their X-rays. Thus, in addition to investigating the potential of conventional PIXE to characterize semiconducting thin films, this thesis also aims to construct a modified setup that eliminates the background contribution. This as an attempt to push the current state of the art of PIXE and could allow one to use the full potential of PIXE.

Chapter 2

Elemental analysis with PIXE

The discussion of this chapter is oriented towards a general understanding of how particle induced X-ray emission can be used to characterize a semiconducting thin film. First, the basic picture of PIXE is introduced together with its ability to convert characteristic X-ray counts or yields to elemental concentrations. Next, the ionization cross section and the fluorescence yield, which make up the total X-ray production cross section, are discussed. Lastly, the chapter ends by illustrating the current understanding of the continuous X-ray background that is observed in PIXE spectra.

2.1 Basic picture

The focus of this work is to investigate particle induced X-ray emission (PIXE) spectroscopy, which is an ion beam analysis method used for characterization of elemental concentrations inside a thin film. A typical PIXE experiment is performed using a MeV proton or He-ion beam that is made to impinge the target sample. As opposed to RBS, the messengers that are used for the characterization are characteristic X-rays instead of elastically backscattered He-ions. A simplified picture of the underlying X-ray production process is illustrated in Figure 2.1.

Here, the MeV proton ionizes a K-shell electron while passing through the target and leaves behind a vacancy or hole in the K-shell. The vacancy can be filled through a deexcitation process where an electron from the L-shell transitions to the K-shell. This would be followed by the emission of a characteristic X-ray with an energy that is determined by the binding energy difference between the two participating shells. The characteristic X-ray that is emitted in this case is referred to as K_α radiation due to the initially created K-shell vacancy. The unique energies that correspond to the characteristic X-rays from different target atoms

provide a fingerprint that can be used to identify the different elements that are present in the target sample.

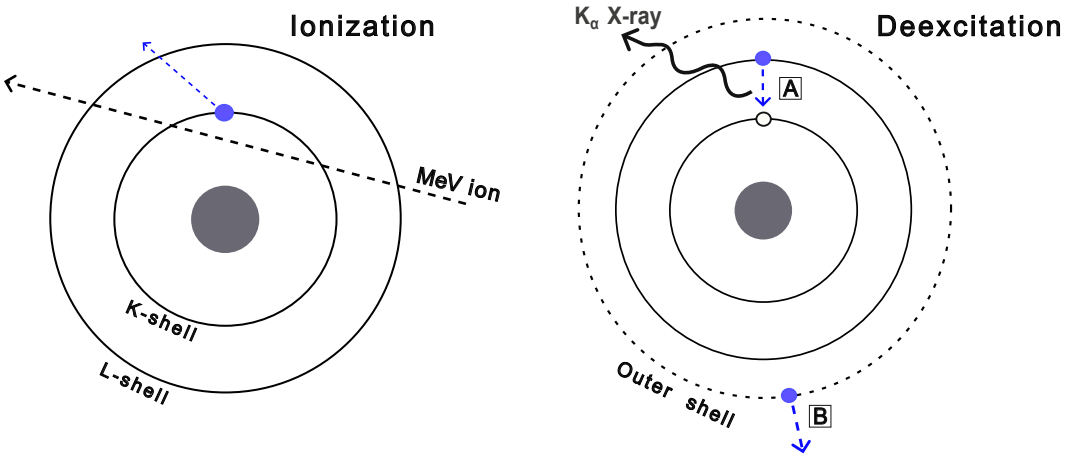

Figure 2.1: Simplified picture of the mechanisms which are behind the production of characteristic X-rays.

There is however a competing process in the deexcitation phase of the atom, where the excess in energy is transferred to an orbital electron that is then ejected from the atom. This electron is called an Auger electron which is shown on the bottom right of Figure 2.1.

Measuring the energy of the characteristic X-rays with a silicon drift detector or HPGe detector allows for the characterization of the target sample based on the amount of measured characteristic X-rays from each element.

The intensity of the signals in a PIXE spectrum are determined by the X-ray production cross section σ_{PIXE}. Experimental values of this cross section are shown in Figure 2.2 as a function of atomic number Z. Important to note from Figure 2.2 is the comparison with the cross section from RBS. First of all, PIXE can be done using X-rays that were created from a K-shell, L-shell or M-shell vacancy which each have their own production cross section. This enables PIXE to be sensitive to elements across a wide range of atomic numbers Z. Here, the K-shell X-rays provide the most accurate results in a quantitative analysis due to the low uncertainties in the production cross section databases [22]. The L-lines and M-lines can still be used for the heavier elements but due to the complex nature of the X-ray production mechanism for these cases the databases show uncertainties between 5-15 % [23]. The large X-ray production cross section for the K-shell of light elements could make PIXE a strong candidate to characterize the light elements inside a sample. The cross section dependence on the material shows again that

RBS is mostly sensitive to the heavier elements.

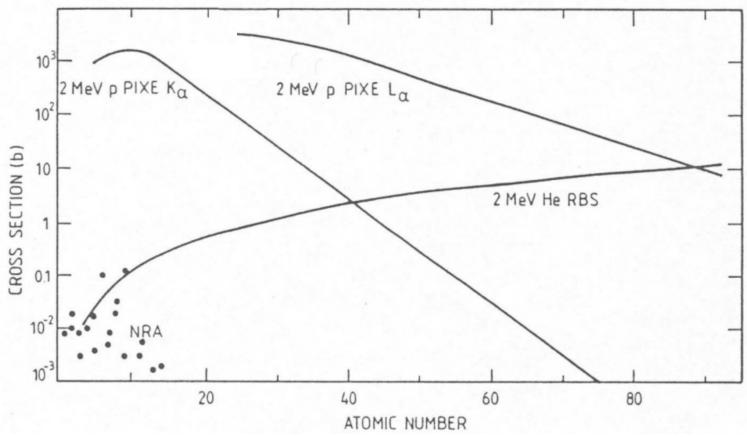

Figure 2.2: X-ray production cross section as a function of atomic number Z. Taken from [19].

The X-ray production cross section σ_{PIXE} is defined as [24]

$$\sigma_{PIXE} = \omega_X \cdot \sigma_{ion},$$

where ω_X is the fluorescence yield which is related to the deexcitation process and σ_{ion} the ionization cross section for an inner shell electron. Quantification of the elements inside a sample is obtained from the intensity of the characteristic X-ray signals. The intensity or yields from a K-shell X-ray signal of element with atomic number Z can be converted into elemental concentrations using the expression [24]

$$Y(Z) = \frac{N_{\mathrm{av}}\omega_{\mathrm{K},Z} b_{\mathrm{K},Z} t_{\mathrm{K},Z} \varepsilon^i_Z \, (\Omega/4\pi)}{A_Z} N_p C_Z \int_{E_0}^{E_F} \frac{\sigma_{ion,Z}(E) T_Z(E)}{S_M(E)} \, dE, \qquad (2.1)$$

where t_Z is the transmission through a possible absorber, ϵ^i_Z is the detector detection efficiency, Ω the detector solid angle and σ_{ion} the ionization cross section of the shell that was involved in the production process. ω_K is the fluorescence yield for the shell and b is the branching ratio. N_{av} is the Avogadro's number, A_Z the atomic mass of the element, N_P the number of incident ions, E_0 the initial energy ions and E_f the final energy. The integral over these energies takes into account that the ions experience energy loss which is determined by the global stopping cross section $S_M(E)$ of the sample. Lastly, $T_Z(E)$ accounts for the fact that the emitted X-rays can be attenuated while leaving the material.

An example of a typical PIXE spectrum from an unknown sample is shown in

Figure 2.3. Note that the K-lines of the lighter element appear at the lower energies while the higher energy characteristic X-rays correspond to the heavier element. Additionally, there is also a continuous background which is clearly visible in Figure 2.3 together with a strong Si X-ray signal. This background limits the detection of the low energy X-rays that correspond to the lighter elements and is the result of the fact that thin films are generally fabricated on a thick silicon substrate. On the other hand, conventional PIXE is able to distinguish the signals from the similar mass elements which is not possible with RBS due to a poor mass resolution.

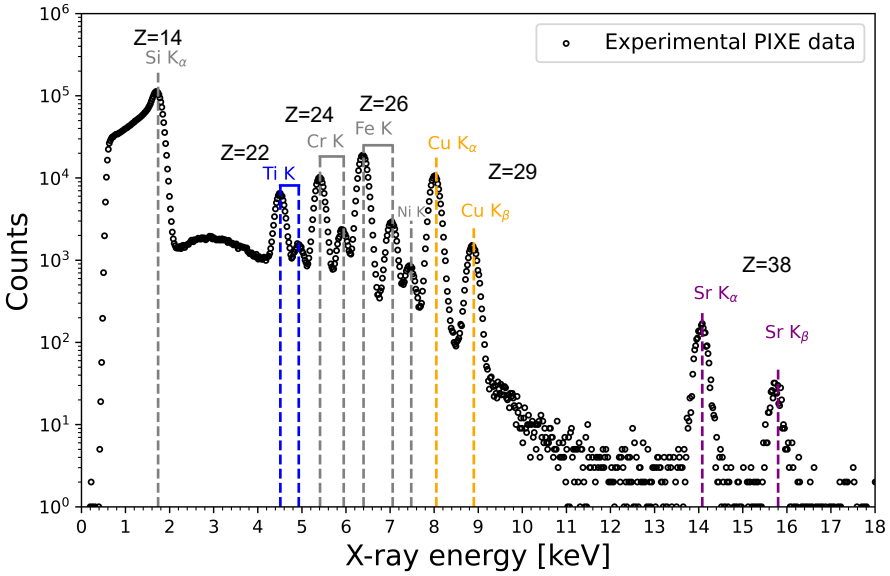

Figure 2.3: Conventional PIXE spectrum of an arbitrary thin film which is mounted on a silicon substrate.

2.2 Ionization cross section

The first part of the X-ray production mechanism is the ionization of an inner shell electron. Understanding the physics of this ionization process is crucial to determine the optimal conditions for X-ray production. There are two different frameworks that are used to describe the ionization cross section. The first one is based on a semi-empirical scaling law, which suggests that there is some underlying mechanism in the ionization process that is valid for each target-ion beam combination. The second framework is based on the current best theory for the ionization cross section. Here, only the semi-empirical model is introduced because it offers a fundamental understanding of the parameters that influence the

ionization cross section. The theoretical model will be introduced in Chapter 5.

For simplicity one can start by considering the case of an inelastic collision between an impinging electron and an inner shell electron. It can be shown for the scattering of an electron with velocity v in a central force field that the amount of transferred momentum ΔP to the target electron is given by [19]

$$\Delta P = \frac{2e^2}{bv},$$

where b is the impact parameter. This inelastic scattering process is illustrated in Figure 2.4.

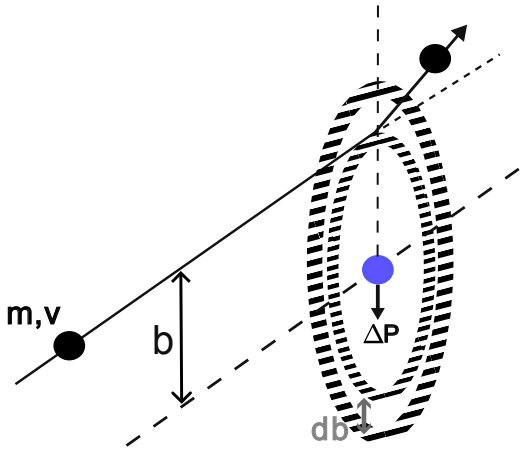

Figure 2.4: The inelastic scattering of a beam electron (black) and an atomic inner shell electron (blue). Inspired from [19].

The energy that is transferred by the electron can be written as

$$T = \frac{(\Delta P)^2}{2m} = \frac{e^4}{Eb^2}, \tag{2.2}$$

which allows for the definition of the differential cross section $\sigma(T)$ for an energy transferred between T and $T + dT$ as [19]

$$d\sigma(T) = -2\pi b db. \tag{2.3}$$

Rewriting Equation (2.2) to an expression for the impact parameter b, inserting this in Equation (2.3) and integrating over the allowed energy transfers results in the total cross section for ionization by an electron with energy E given by [19]

$$\sigma_e = \int_{T_{min}}^{T_{max}} d\sigma(T) = \int_{T_{min}}^{T_{max}} \frac{\pi e^4}{E} \frac{dT}{T^2} = \frac{\pi e^4}{E} \left(\frac{1}{T_{min}} - \frac{1}{T_{max}} \right) \tag{2.4}$$

Here, T_{max} can be seen as the initial energy of the beam particle in the case of an electron. This is typically much larger than $T_{min} = E_B$, which allows one to approximate Equation (2.4) as

$$\sigma_e \approx \frac{\pi e^4}{E E_B} = \frac{\pi e^4}{U E_B^2},$$

where $U = E/E_B$ and E_B is the binding energy of the orbital electron. This approximation shows that the ionization cross section for an electron beam with $E >> E_B$ decreases for the higher beam energies.

In general, the ionization cross section becomes maximal for an electron beam with a beam energy that is two or three times larger than the binding energy of the inner shell electron [19]. Taking into account the general magnitude of the binding energies for different elements, this corresponds to an electron beam with an energy of order keV. The energy dependence of the ionization cross section is shown in Figure 2.5. This energy dependence implies that heavier atoms would require a higher beam energy because the binding energy for K-shell electrons scales with Z^2 [19].

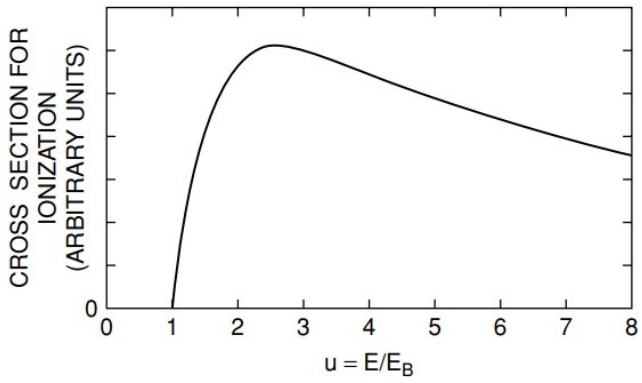

Figure 2.5: Electron ionization cross section as a function of reduced energy U. Taken from [25].

One can now use these dependencies that show up in the calculation of the electron ionization cross section to obtain a semi-empirical description of the ionization cross section for a proton beam [19]. This method is based on the idea that the time-dependent electric field created by a charge passing near an atom will be the same for a proton and electron of the same velocity. Using the electron and proton mass this corresponds to protons that have an energy which is a factor 1836 larger than the electron energy. This implies that the ionization cross section for a proton beam will be maximal at beam energies of a few MeV instead of keV.

Starting from experimental K-shell ionization cross sections for different elements and rescaling them using the K-shell binding energy of the corresponding element, one can study the energy dependence of these cross sections as shown in Figure 2.6.

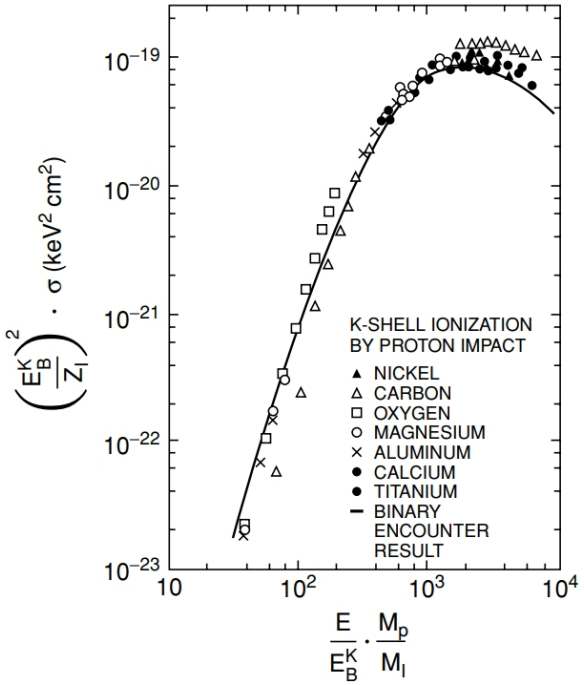

Figure 2.6: Semi-empirical model for the K-shell ionization cross section of different elements with different ionizing particles as a function of beam energy. E_B^K is the binding energy of the K-shell electrons from different elements. Taken from [19].

Here, the experimental proton beam ionization cross sections for different elements seem to follow the same behavior in terms of the reduced beam energy. For the proton beam case one has $Z_1 = 1$ and $M_p/M_I = 1$, which implies that the ionization cross section becomes maximal for proton beam energies of a few MeV. This universal behavior allows one to determine a semi-empirical parameterization of the ionization cross sections of different elements as a function of the reduced beam energy U by means of a fit to the scaled experimental data. For the case of a He-ion beam, one would have $M_p/M_I \approx 1/4$ for the scaling of the x-axis. This means that heavier ion beams require a higher beam energy E to achieve the maximal value of their ionization cross section. At the maximal value however, the ionization cross section for a given element would be larger compared to the proton beam case due to the larger value of Z_1. Similar methods can be used for L-shell and M-shell electron ionization and the current databases for these semi-empirical models can be found in the literature [26, 27].

2.3 Fluorescence yield

After the ionization of a specific inner shell, the ionized atom is left with a primary vacancy. When this vacancy is filled by the transition of an electron from a higher energy level, it is called a radiative transition [24]. There are different transitions possible depending on the deep electron structure of the atom, which are shown in Figure 2.7. The characteristic X-rays that are emitted in the transition processes are labeled according to the shell in which the primary vacancy was located. Figure 2.7 also shows that this shell label is accompanied by alpha or beta which refers to the initial state of the transitioned electron.

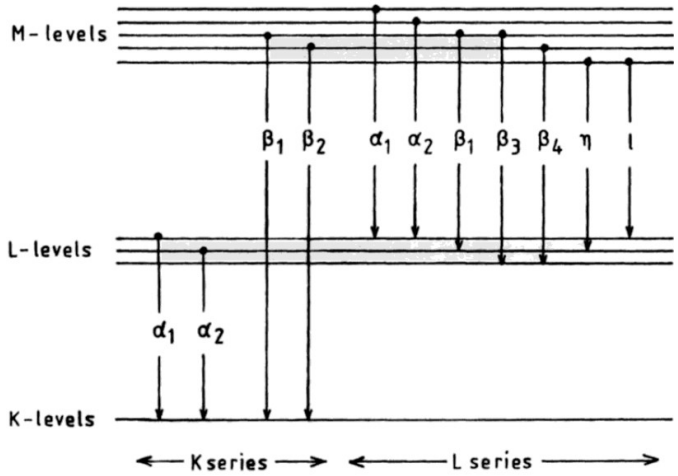

Figure 2.7: General definition of characteristic X-rays that result from different atomic transitions. Taken from [24].

Using these radiative transition definitions one is able to define the fluorescence yield for each shell. The radiative deexcitation process involving a primary vacancy in shell i is described using the fluorescence yield $\omega_{X,i}$. The fluorescence yield of the K-shell ω_K is defined as [28]

$$\omega_{X,K} = \frac{W_X}{W_X + W_A},$$

where W_X is the radiative transition rate and W_A the Auger electron transition rate. The K-shell fluorescence yield can be experimentally determined by measuring the amount of K-shell characteristic X-rays and Auger electrons that are emitted against the total created vacancies. Measuring the fluorescence yields for different elements results in the experimental values [29] that are shown in Figure 2.8. The experimental values are shown together with measured fluorescence yields from the other shells and compared with a semi empirical model [29]. First, it is

important to note that the K-shell fluorescence yield increases for the heavier elements, which means that they will undergo more radiative transitions compared to the lighter elements. The L-shell fluorescence yields are only shown for the heavier elements but this is due to the fact that an atom needs to have electrons in the M subshells for these radiative transitions. A similar thing can be concluded about the reported M fluorescence yields but it is most important to notice the small magnitude of these L- and M-shell fluorescence yields. They imply that secondary effects which are produced after the emission of a K-shell X-ray are relatively small. An example of this is the case of K_α emission, where a secondary vacancy is created in the L_3 subshell. This vacancy would then most often be compensated by the ejection of an Auger electron instead of an X-ray. Secondary X-rays that don't directly result from the primary vacancy would otherwise serve as a strong secondary effect in a PIXE measurement.

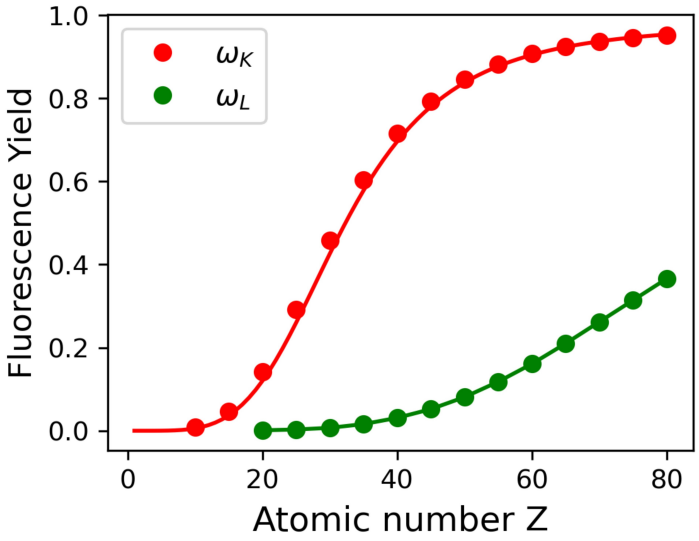

Figure 2.8: Experimental fluorescence yield values for the K-shell and L-shell as a function of atomic number Z.

One notices the different behavior of the K-shell X-ray production cross section from Figure 2.2 compared to the K-shell fluorescence yields from Figure 2.8. Lighter elements are intrinsically less likely to undergo radiative transitions compared to heavier elements. However, at the start of this section it was stated that PIXE could be very sensitive to light elements, which could seem contradicting at first sight. This difference illustrates how the ionization cross section must have an even stronger dependence on the atomic number to compensate for the small fluorescence yield values. For the elements lighter than oxygen one can observe that the small fluorescence yield values start to overcome the large ionization cross

section corresponding to the lighter elements.

Figure 2.8 may seem to show the fluorescence yield of different atomic shells but one should be careful with the way that these are defined. The K-shell fluorescence yield was straight forward to define but things become more complex when trying to do the same for the L-shell. In this case, the fluorescence yield is defined as an average fluorescence yield $\bar{\omega_L}$ given by [28]

$$\bar{\omega_L} = N_1\omega_1 + N_2\omega_2 + N_3\omega_3, \tag{2.5}$$

where N_i is the amount of primary vacancies in subshell i relative to the amount of total L-shell primary vacancies. The L-shell fluorescence yield can not be defined in the same manner as the K-shell case because it is very hard to ionize only one of the three subshells from the L-shell. This different definition also makes it harder to measure the fluorescence yields of X-rays that are created from primary vacancies in the different subshells. From the definition of Equation (2.5), one can conclude that $N_1 + N_2 + N_3 = 1$ so the average fluorescence yield is consistent with the general fluorescence yield definition [28].

In order to measure the ω_1, ω_2 and ω_3 quantities, one needs to perform three different measurements [28] of the average L-shell fluorescence yield. With these three measurements it is possible to obtain the ω_i quantities from the three equations that are given by the average fluorescence definition. This is only possible if the primary vacancy distributions N_1, N_2 and N_3 are known for the three experiments. However, the situation is more complex than mentioned so far because in the case of primary L-shell vacancies there is an additional competing process other than deexcitation through the emission of Auger electrons. The additional competing transitions are called Coster-Kronig (CK) transitions [30] which are defined as electron transitions between subshells of the same shell. These transitions don't result in the ejection of an electron or the emission of X-rays. Together, the complex nature of the L-shell fluorescence yield and the possibility of CK transitions cause large uncertainties [30, 31] in the databases of these quantities which are larger compared to the K-shell fluorescence yield. This is one of the reasons why K-shell X-rays result in a more accurate quantitative analysis of the elemental concentrations inside a thin film.

2.4 Background radiation

Having acquired an understanding of the quantities which determine the intensity of the signals in a PIXE spectrum, it is also important to introduce the background contributions of a measurement. In experiments where a beam of charged particles

is used to ionize the inner shell electrons, there will always be a contribution from bremsstrahlung X-rays [32] that are produced by the slowing down of the beam particles. The deceleration is caused by the interaction between the ions and the target nuclei. The probability for bremsstrahlung P behaves as $P \approx 1/M^2$ [33], where M is the mass of the radiating beam particle. This mass dependence implies that there will be intense bremsstrahlung production in experiments where an electron beam is used to ionize the inner shell electrons. This is for example the case in scanning electron microscopy (SEM) [19], which is typically performed with keV electrons. In the case of PIXE, one utilizes a proton beam which reduces the bremsstrahlung contribution drastically. Comparing the intensity of the bremsstrahlung for experiments with a MeV proton to a keV electron beam results in an intensity that is reduced by a factor of $1/(1836)^2$. However, there is still a continuum background contribution in PIXE experiments. The difference is that this background comes from the interaction between the ion beam and the electrons in the silicon substrate on which the thin film is mounted.

The remaining background has been the focus of many different studies [34, 35, 36] aimed at finding the processes that contribute to it. This resulted in the conclusion that the total background, in experiments with a proton beam up to 3 MeV, can consist of three different physical processes. They are referred to as quasi-free electron bremsstrahlung (QFEB), secondary electron bremsstrahlung (SEB) and atomic bremsstrahlung (AB). The relative intensities of each contributing process are illustrated in Figure 2.9.

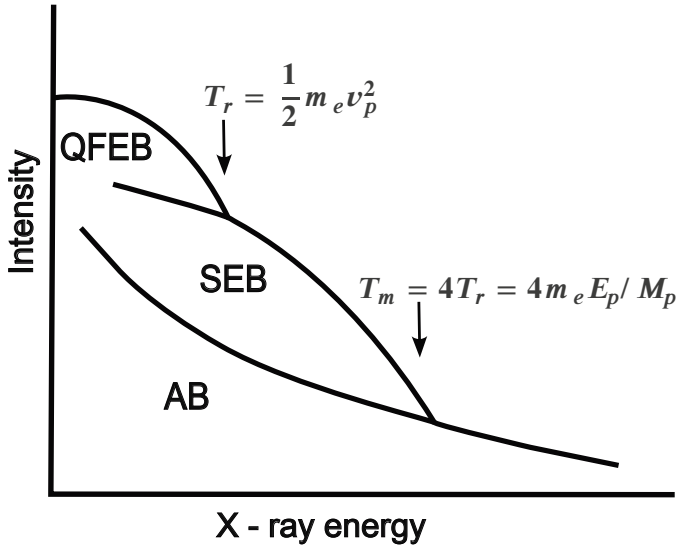

Figure 2.9: Intensity of the tree main electron bremsstrahlung processes for a proton beam with energy E_p. Taken from [24].

QFEB [37] involves the production of X-rays due to the interaction between the quasi free electrons in the sample and the proton beam. The process only has a contribution when the velocity of the electrons is negligible compared to the beam particle energy E_p. The process is then described in the rest frame of the proton such that the electrons are quasi free with respect to the beam particle at rest. Figure 2.9 shows that this contribution is dominant at very low X-ray energies but becomes negligible for X-ray energies that are larger than the kinetic energy T_r of the quasi free electrons in the proton rest frame, which is when the quasi free approximation breaks down. Electrons with a larger energy can thus not contribute to the production of X-rays which sets a limit for the QFEB X-rays because bremsstrahlung X-rays can not have a larger energy than the energy of the quasi free electron due to energy conservation.

SEB arises from electrons, ionized from their shell, that interact with the nuclei of the target material [24]. This causes the electrons to slow down and produce a continuum of secondary electron bremsstrahlung X-rays. Figure 2.9 indicates that this is the dominant contribution over a wide range of X-ray energies which means that it will largely determine the shape of the bremsstrahlung background. The intensity of the SEB contribution starts to fall off at an energy E_m, which is the maximal energy that a proton of energy E can transfer to an electron at rest. The literature describes the bremsstrahlung X-rays with higher energies than this value to be the product of electrons that already had a significant energy.

The last contribution of AB is a complex process arising from the atomic structure inside the target material. It is described as the radiation that is produced when an electron is excited to a continuum of energy states and then eventually transitions back to the initial energy state [38]. The promotion to a continuum of states implies that AB also produces a continuum of X-rays. Although there is a good agreement between theoretical and experimental cross sections of these background processes, this has not resulted in a model that can be used to subtract the background from PIXE measurements [24].

In this research, one of the goals is to investigate the effect that substrateless PIXE could have on this bremsstrahlung background. Eliminating the substrate could reduce the bremsstrahlung continuum background and potentially also reduce the intense Si X-ray that was shown in the conventional PIXE measurement from Figure 2.3. With less intense background, one could utilize the large X-ray production cross section that was mentioned at the start of this section to characterize the light elements in a thin film.

Chapter 3

PIXE measurement

The energy deposition process that the X-rays undergo in the detector can be complex. This third chapter starts by covering the X-ray interaction mechanisms with matter that govern the energy measurement. Understanding the interaction between X-rays and the detector medium is crucial to describe the detection mechanism. Then, two important detector types are introduced. Combining the fundamental aspects of these sections allows for the introduction of the initial test setup that was constructed to perform PIXE measurements. Lastly, the chapter ends with a discussion of the first scientific results that were obtained with this setup.

3.1 Interaction of X-rays with matter

3.1.1 Photoelectric effect

Detection systems [39] often rely on the interaction of the particle or radiation of interest with some kind of detector medium. A charged particle will ionize the active detector medium of a semiconductor detector to create electron-hole pairs that induce a signal in the electronic circuit of the detector. X-rays however, don't carry a charge and can thus not deposit their energy in the same manner as a charged particle can. One of the interaction mechanisms that is fundamental for the detection of X-rays is the photoelectric effect.

Here, the X-ray is absorbed in the material and a photoelectron is ejected. This photoelectron carries a large fraction of the energy of the absorbed X-ray and will create charge carriers in the detector medium. In order to maximize the detection efficiency, one needs to understand how certain parameters influence the photoelectric cross section. A simplified way of thinking of the photoelectric effect [19]

is to approximate the atomic potential that acts on the bound electron to be a 1D potential square well, as shown in Figure 3.1.

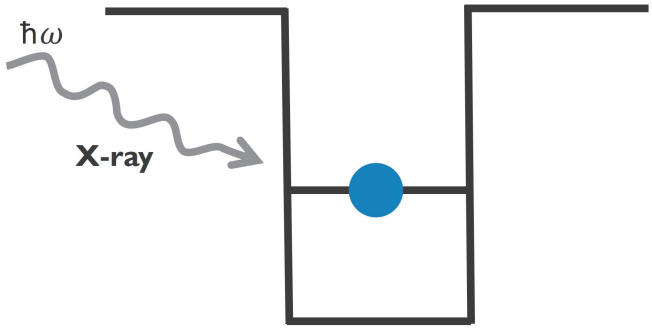

Figure 3.1: Simplified illustration of the photoelectric effect.

The depth of the well would reflect the binding energy of the specific atomic shell. For a K-shell electron, the incoming X-ray energy should be sufficient enough to overcome the K-shell binding energy in order to break the bound state. The photoelectric cross section can be estimated using the square well approximation [19] which yields an expression that indicates the dependency of the cross section on the energy of the photon and the binding energy of the K-shell. To obtain a more complete expression for the photoelectric cross section, one needs to use the 3D hydrogenic wave function to describe the initial bound state of the electron.

Consider a K-shell electron in an atom with atomic number Z, that is being ejected after the absorption of an X-ray with energy $\hbar\omega$ [40]. One can assume that $\hbar\omega > E_b$ which results in an ejected electron energy of $\hbar^2k^2/2m = \hbar\omega\text{-}E_b$. Here, the photoelectric cross section can be derived using first order time dependent perturbation theory. In this framework one can define the transition probability w using Fermi's golden rule [40] given by

$$w = \frac{2\pi}{\hbar} p(k) \left\langle \psi_f | H' | \psi_i \right\rangle^2 ,$$

where $p(k)$ is the density of final states, k is related to the momentum of the final state electron $p = \hbar k$ and the final factor is the matrix element of the transition. The initial state ψ_i of the bound electron is described by the hydronic wave function [19]

$$\psi_i = \pi a^3 e^{-r/a},$$

where $a = a_0/Z$ and $a_0 = \hbar^2/(me^2)$ with the electron mass m. The electron final state ψ_f in the matrix element can be approximated by a planar wave $\psi_f = L^{-3/2} \exp(i\vec{k}\cdot\vec{r})$. This approximation is called the planar wave Born approximation

(PWBA) [40] and is only valid for high energy photons and for light to medium atomic number elements. The transition between these states is induced by the perturbation Hamiltonian that contains the description of the X-ray as an EM-wave. This perturbation Hamiltonian is the first order perturbation term in the total Hamiltonian from a charge inside an electric field that is described by the vector potential $\vec{A}$. From this transition probability per unit time one obtains the total cross section σ_{ph} for a K-shell electron given by [40]

$$\sigma_{ph} = \frac{w}{I} = \frac{128\pi\hbar e^2}{3mc}\frac{E_B^{5/2}}{E^{7/2}}, \tag{3.1}$$

where $E = \hbar\omega$ is the energy of the interacting X-ray and E_B is the binding energy of the K-shell of an element with atomic number Z. I represents the incident photon flux determined by dividing the Poynting vector, defined by the vector potential, by one energy quanta. Two main conclusions can be obtained from the photoelectric effect cross section of Equation (3.1). First of all, the ability of a detector material to detect an X-ray through the photoelectric effect, will depend on the atomic number of the material because the binding energy of the K-shell increases as a function of atomic number Z^2. Secondly, each given material will become less efficient in detecting X-rays that have a large energy. The strong binding energy dependence also implies that a photon will have a higher probability to be absorbed by a K-shell electron instead of a L-shell electron. The derivation of Equation (3.1) was performed using PBWA and specifically for K-shell electrons, but generally the relation [39]

$$\sigma_{ph} \sim \frac{Z^4}{E^3}$$

is valid for X-rays in the keV regime.

3.1.2 Compton scattering and pair creation

Other than the photoelectric effect, the X-ray can also interact with the detector medium through Compton scattering or pair creation [39]. The case of Compton scattering on an electron at rest in the lab frame is shown in Figure 3.2. Here, the photon starts with an energy $h\nu$ and after the scattering this changes to $h\nu'$. A certain fraction of the X-ray energy is transferred to the electron which can deposit its energy in the detector material and the scattered X-ray could again interact via the photoelectric effect or Compton scattering. The different energies that the scattered X-ray can have are dictated by Compton's formula which can be derived by utilizing conservation of energy and momentum. This formula is given by [39]

$$h\nu' = \frac{h\nu}{1 + \frac{h\nu}{m_e c^2}(1 - \cos\theta)},$$

where θ is the scattering angle of the interacting X-ray in the rest frame of the electron, as shown in Figure 3.2. Compton scattering can in theory happen but the probability is very low.

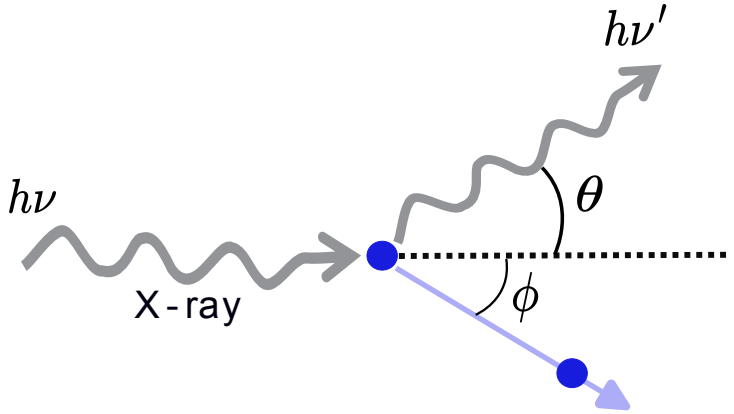

Figure 3.2: The process of compton scattering in the rest frame of a target electron.

For pair creation to occur, the interacting X-ray needs to be able to create an electron-positron pair that then interacts gradually with the detector medium. However, energy conservation implies that this can only occur when the X-ray has an energy that is twice the rest mass of the electron. The characteristic X-rays from a PIXE experiment typically have energies below 20 keV, which implies that they will never be able to interact via this mechanism. The absorber material and X-ray energy regimes in which each of the three mechanisms are dominant are illustrated in Figure 3.3.

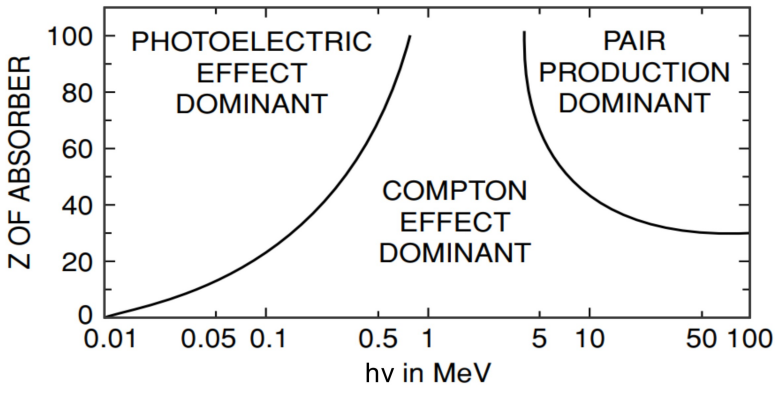

Figure 3.3: Classification of the dominant X-ray interaction process for different combinations of material atomic numbers and the energy of the interacting X-ray. Taken from [19].

Figure 3.3 illustrates how the combination of a Ge or Si detector for the detection of X-rays with an energy of a few keV implies that the photoelectric effect is the dominant interaction mechanism in the case of PIXE. Apart from Compton scattering, there also exists a small probability that the X-ray scatters in a coherent way with an atom of the detector material [39]. Here, there would not be any energy loss and only a change in direction of the scattered X-ray. This effect is often ignored because it is very unlikely to happen in a Ge or Si crystal, which are generally used as detector media.

3.1.3 Attenuation coefficient

The attenuation coefficient μ_i of a given detecting or absorbing material is defined by the expression [19]

$$I = I_0 e^{-\mu_i x},$$

where I_0 is the incident intensity of an X-ray beam with a certain energy, x the thickness of the material and I the intensity which is left after traversing a distance x inside the material. The magnitude of the attenuation coefficient in the case of keV X-rays, is determined by the photo electric effect cross section that was previously introduced. Here, the attenuation coefficient μ can be defined in terms of the photo electric cross section σ_{ph} as [19]

$$\mu = n_s \cdot \sigma_{ph} \cdot N,$$

where n_s is the number of electrons in shell s and N is the areal density of the element inside the detecting or absorbing material. This relation is valid because the cross section does not take into account that there are multiple bound electrons in a given shell. The total amount of scattering centers in the case of this interaction is the total number of bound electrons which also motivates the multiplication with the atomic areal density. Important to note is that the previous discussion of the cross section in terms of the K-shell and L-shell electrons did not take into account that there are generally more bound electrons in the L-subshells compared to the K. The attenuation coefficient does take this into account but the strong binding energy dependence of the ionization cross section still results in a higher probability for the ionization of a K-shell electron.

With the definition of the attenuation coefficient, it is possible to introduce the concept of an absorption edge [19]. Figure 3.4 shows the attenuation coefficients of different elements as a function of X-ray energy. Each attenuation coefficient seems to show a discontinuous increase at certain X-ray energies, which diverges from the general $1/E^4$ behavior. These features are called absorption edges and characterize the energy at which the interacting X-ray would have enough energy

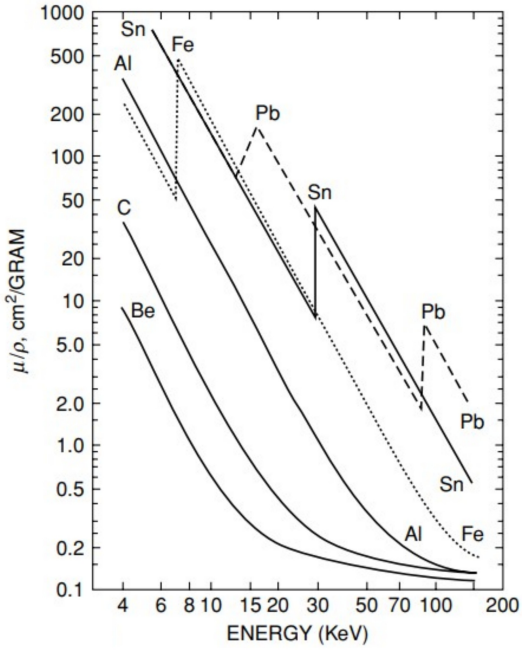

Figure 3.4: Attenuation coefficients from different detection or absorber materials as a function of X-ray energy. Taken from [19].

to overcome the binding energy of a shell that it was not able to ionize before. This causes a sudden increase in the attenuation coefficient after which the energy behavior restores to the expected $1/E^4$ shape of the attenuation coefficient. These absorption edges can be utilized in absorbers for the intense attenuation of characteristic X-rays that have an energy which is slightly higher than one of the absorption edges of the absorber material.

3.2 Detection mechanism

With the photoelectric effect as the dominant interaction, the X-ray detection mechanism is determined by the measurement of the energy of the photoelectron. The general layout of a planar semiconducting X-ray detector is shown in Figure 3.5. The detector consists of a p doped anode, a n doped cathode and a region which is less heavily doped in between them. This region becomes the active detector area when a reverse bias is applied to the pn junction [39]. With the reverse bias applied, a depletion region is created which extends into the intrinsic part where no remaining free charge carriers are left. The absence of free charge carriers is what makes this intrinsic region the active area of the detector.

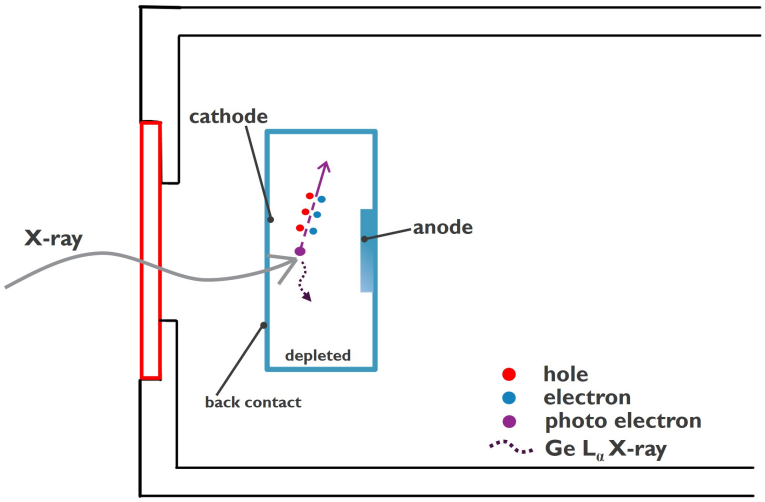

Figure 3.5: Detection principle of keV X-rays in a semiconducting Ge detector.

The X-ray detection principle is also illustrated in Figure 3.5, where an X-ray interacts in the active area through the photoelectric effect. The generated photoelectron slowly ionizes the atoms in the detector crystal and creates electron hole pairs in the process. The electric field in the depletion region, which results from the applied bias voltage, will cause the electrons to drift towards the anode and the holes towards the cathode. The amount of electron-hole pairs is proportional to the energy of the photoelectron [39] and the drift of these induced charge carriers will generate a charge pulse or current in the detector electronics.

However, the X-ray will not transfer all of the energy to the photoelectron. Here, the remaining excess of energy is given to Auger electrons which also generate charge carriers that contribute to the total amplitude of the charge pulse. Depending on the detector material and the initial X-ray energy, it is also possible that the remaining energy results in the emission of a characteristic X-ray. In the case of the Ge-crystal shown in Figure 3.5, this can be the L_α X-ray which has the possibility to undergo the same energy deposition process as the initial X-ray and thus also contribute to the total charge pulse amplitude.

3.3 Data acquisition and electronics

3.3.1 Detector electronics

The charge pulse that is produced by the drifting of the created charge carriers is integrated over a charge sensitive capacitor. This is done using the preamplifier

circuit shown in Figure 3.6. Here, the integrated charge pulse from a given X-ray results in a voltage increase across the charge sensitive capacitor. The capacitor voltage as a function is the output of this preamp circuit. Figure 3.6 also shows that the capacitor voltage seems to have a strong reset behavior. This is caused by a switch that resets the capacitor voltage by grounding the system for a very short time, when the dynamic range of the capacitor is reached. This circuit is called a transistor reset preamplifier (TRP) [39] and is often used for the detection of low energy X-rays. The TRP also has limitations because the reset causes the

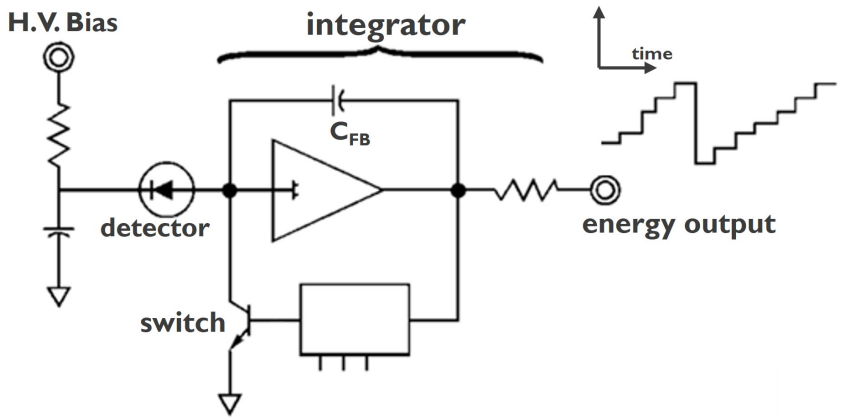

Figure 3.6: The electronic circuit connected to a semiconducting X-ray detector.

system to be inactive for a small amount of time. This reset occurs in a time of less than 2 μs which allows the electronic circuit to resume the measuring process in a quick manner. However, the dynamical range of the capacitor can be swiftly reached in the case of high energy X-rays or large event throughput. The effect of the reset frequency is quantified in the detector dead time DT given by

$$DT = \frac{\text{Real time} - \text{Live time}}{\text{Real time}} \times 100,$$

where Live time is the active measuring time of the detector and Real time is the total time which also includes the detector dead time due to the reset process. A measurement with a detector dead time of 0 % is the ideal case because the Real time would be the same as the Live time. In the case of PIXE with keV X-rays, one can generally interpret a detector dead time of around 1 % to not significantly affect the measurement. The TRP is able to process almost 1000 pulses between resets in the case of 5.9 keV/event .

3.3.2 Digital signal analyzer

The voltage pulses that are acquired from the TRP preamplifier have to be discritized in order to determine the corresponding voltage increase which is proportional to the energy of the initial X-ray. This is done using a trapezoidal filter [41] which computes a trapezoidal pulse for each voltage step which has a magnitude above a certain threshold value. An example of this conversion is shown in Figure 3.7. The flat top part of this trapezoidal pulse is very important because this corresponds to the digitization of the voltage pulse amplitude.

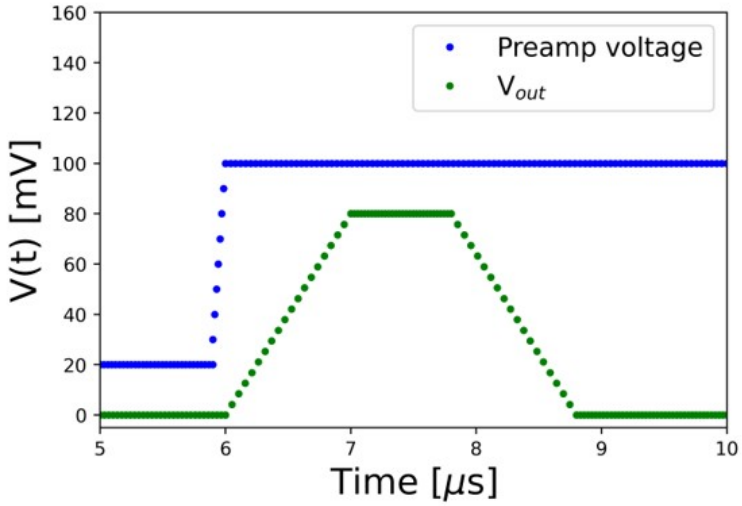

Figure 3.7: Digitization of a voltage step across the charge sensitive capacitor. The voltage is digitized at the flat top part of the converted trapezoidal pulse.

The trapezoidal pulse from Figure 3.7 is characterized by a certain rise and flat top time which dictate the shape of the pulse. This pulse is obtained by the subtraction of two moving averages [41] that the data acquisition software will calculate while the time series of the preamp voltage is being received. The output V_{out} is then calculated as

$$V_{out}(i) = V_{ma1}(i) - V_{ma2}(i),$$

where $V_{ma1}(i)$ is the result of a moving average that averages the preamp voltage in a fixed interval while it goes over the signal. $V_{ma2}(i)$ is a second moving average which is offset by a well defined time t_f with respect to the first moving average. A simplified illustration of the trapezoidal pulse conversion based on two moving averages is shown in Figure 3.8. Initially, the two moving averages are both averaging the preamp voltage in a regime where there is no voltage step. This results in $V_{out} = 0$ which can also be observed in Figure 3.7. Then, the rising part of the

trapezoid starts to form because the averaging interval of V_{ma1} starts to include some of the increased voltage values which results in an increasing V_{out} voltage. This rising part is defined by the time t_r, after which the first moving average will only average the preamp voltage after the voltage step. Here, the flat top part of the trapezoidal pulse is generated which is defined by the offset between the two moving averages. At some point, the second moving average will also start to average a part of the voltage step resulting in a decrease in the voltage V_{out} towards the baseline value of $V_{out} = 0$. This process keeps repeating for every voltage increase in the preamp voltage.

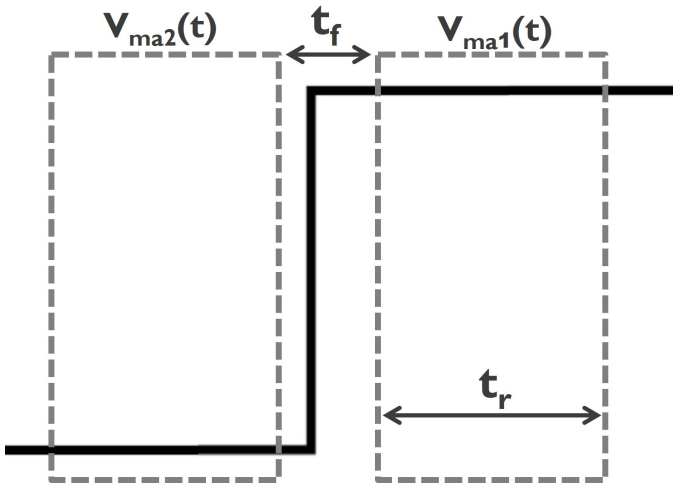

Figure 3.8: Schematic illustration of the moving average differentiator that is used in the trapezoidal filter.

The digitized voltage values from each pulse are then stored in different channels according to their voltage value. For PIXE measurements with the Ge-detector from Figure 3.5, the literature [42] illustrates that a flat top time $t_f = 0.8$ μs and rise time $t_r = 5.6$ μs result in a good measurement performance. These are also the data acquisition parameters that are used in this work. Important to note is that a long rise time can cause interference between two or multiple voltage increases due to the large averaging window of the filter, whereas a short rise time can cause the measurement to become extremely sensitive to electronic noise.

3.4 SSD versus HPGe detectors

3.4.1 Detector build

The detector that was shown in Figure 3.5 is the Canberra GUL0055 high-purity germanium (HPGe) detector [43]. It contains a 25.4 μm Be entrance window that protects the detector from any outside contamination. This entrance window already affects the low energy X-rays significantly. An alternative option to the HPGe detector is the silicon drift detector (SDD) from rayspec [44]. The SDD is not available during the time frame of this work but will be available for future research, which makes it interesting to compare it to the HPGe detector that is used in this research. The build and detection mechanism are shown in Figure 3.9 [44], which is a bit different compared to the HPGe. It contains a small anode which is surrounded by thin circular metal strips to which a voltage is applied. The voltage is applied with a gradient, starting from the inside strip towards the outside strip, that will induce a non-uniform electric field in the active area of the detector. This is what allows the small dimensions of the anode as can be seen in Figure 3.9, where the charge carriers are guided along the electric field lines towards the anode.

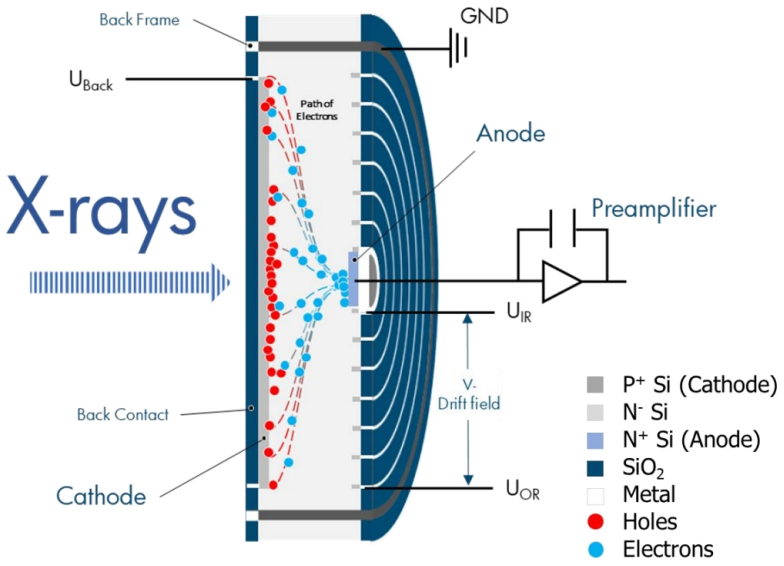

Figure 3.9: Schematic overview of the detection of an X-ray in a SDD detector.

One of the reasons as to why SDD are used in PIXE experiments is the small detector capacitance [45]. This is the result of the small anode and is important because the electronic noise that impacts the performance of the detector scales with this capacitance. Another thing that can make the SDD from rayspec useful

is the thin 1 μm CH entrance window. This implies that the detector is intrinsically designed to be able to measure low energy X-ray better than the HPGe detector. The small detector capacitance can also allow the SDD to measure the signals from these low energy X-rays.

The detection mechanism that was described in Section 3.2 only performs well if the active area is free of any free charges. However, due to the small Ge bandgap of 0.66 eV, valence electrons can promote from the valence band to the conduction band. These free charges could cause recombination with the charge carriers from the X-ray or produce a dead current under the influence of the electric field across the depletion region. The Ge detector is cooled to -185°C (88 K) in order to reduce the probability of thermal excitation [39]. This is done using a cooltip [46] that is built in with the detector. The cooltip system consists of a cold head that transfers heat away from the Ge detector. The Si detector on the other hand has a bandgap of 1.5 eV which is larger than the Ge case. Nonetheless, the SDD from rayspec also has a cooling system which cools it to 15°C. Both of these temperatures of the Ge and SDD are preset by the manufacturer and can not be changed.

3.4.2 Detection efficiency

The detector efficiency can be determined as a function of X-ray energy with the expression [24]

$$\epsilon_i = \frac{\left[\prod_1^3 \exp(-\mu_i x_i)\right] \cdot [1 - \exp(-\mu_{Ge} D)] \cdot f_E}{(1 + z/d)^2}, \tag{3.2}$$

where μ_i denotes the absorption coefficients from a layer of element i and D is the thickness of the HPGe active layer. f_E accounts for the potential escape of X-rays from the active area. Absorption coefficients are energy dependent and are retrieved from the XCOM database [47] of NIST. The first layer is the 25.4 μm Be window and the second and third layer are respectively a 100 nm Al electrode and a 10 nm Ge dead layer. A possible ice layer on top of the detector is neglected in this expression [24]. An important part of the expression from Equation (3.2) is the Ge absorption coefficient. The high density of Ge results in a good detector efficiency over a wide range of X-ray energies. This is illustrated in Figure 3.10, where the efficiency of the Ge detector is compared to a Si detector.
The Si attenuation coefficients will be lower for the higher X-ray energies. In the lower energy regime, the detector efficiency is limited by the layers in front of the detector active area.

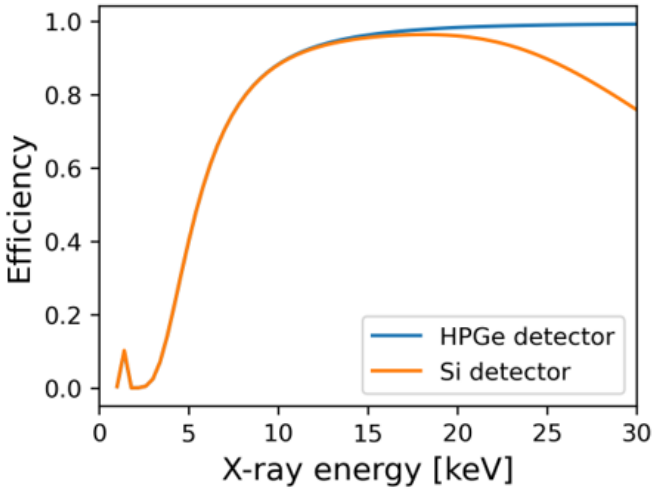

Figure 3.10: Efficiency comparison between a HPGe detector and a Si detector of the same thickness.

3.4.3 Detector lineshape

The expected result of measurement with an X-ray detector which stores the amplitudes of the voltage pulses, originating from each X-ray, in discrete channels is illustrated in Figure 3.11. In this figure, the channel numbers have already been converted to X-ray energies which make up the X-axis of the PIXE spectrum. The vertical axis indicates the amount of counts that were obtained in each channel.

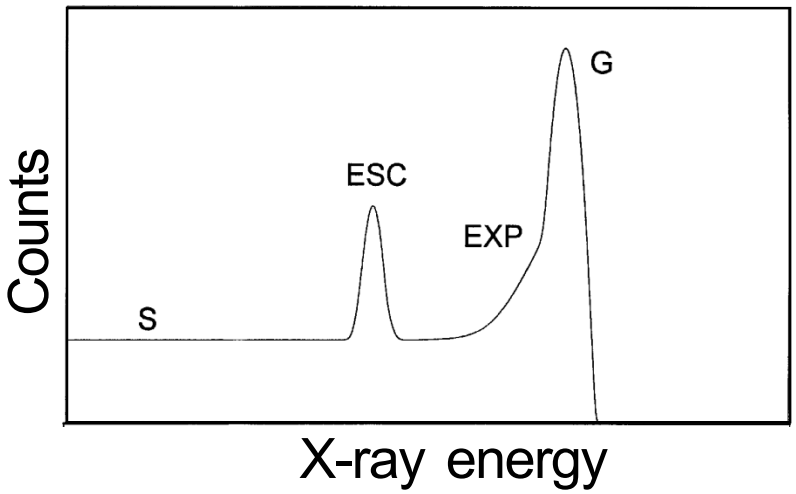

Figure 3.11: The expected detector lineshape from a monochromatic X-ray beam in the case of detection through the photoelectric effect. Inspired from [48].

Important to note is that the theoretical measurement from Figure 3.11 resembles a measurement of a monochromatic X-ray beam, where no other X-ray energies are present, that interacts with the detector medium through the photoelectric effect. The resulting shape of the signal is referred to as the lineshape [48] of the detector. The main feature of the lineshape is called the photopeak which is centered around the energy $E_{\text{X-ray}}$ of the monochromatic X-ray beam. However, the lineshape also contains an exponential low energy tail that extends from the photopeak onto a shelf with a more or less constant height. This low energy feature is caused by the incomplete charge collection (ICC) [48] that occurs when the Auger electrons or photoelectrons that originate from the X-ray escape the detector medium. The intensity of the shelf and low energy tail is expected to be below 1 % of the total intensity of the photopeak when the detector is designed to measure the energy $E_{\text{X-ray}}$ with a good performance.

The final feature from Figure 3.11 is referred to as an escape peak [48]. This signal is the result of an escaping characteristic X-ray that is created in the energy deposition process. The discrete energies of the characteristic X-rays is what results in a discrete signal instead of a continuous signal. To illustrate this, one has to start from Figure 3.5, where the characteristic Ge L-shell X-ray can escape the detector medium without contributing to the induced charge pulse in the electronics. This results in the escape signal centered around an X-ray energy of $E_{\text{X-ray}} - E_{L\alpha}$. The escape signals are expected to be more intense than the shelf due to the large attenuation lengths of X-rays.

The photopeak from Figure 3.11 exhibits a certain width which defines the energy resolution of the detector. The energy resolution reflects the ability of the detector to separate similar energy values from different X-rays. Generally, the detector energy resolution ΔE can be written as [49]

$$\Delta E = \sqrt{\Delta E_{st}^2 + \Delta E_{el}^2},$$

where ΔE_{st} reflects the statistical nature of the charge carrier formation process and ΔE_{el} resembles the contribution from the electronic noise. The lower limit of the energy resolution is mostly defined by the statistical fluctuation in the amount of charge carriers that X-ray of the same energy produce in the detector medium. This statistical contribution is defined as [49]

$$\Delta E_{st} = 2.355\sqrt{F \cdot w \cdot E},$$

where F is the Fano factor, w the energy that is needed to produce an electron-hole pair in the detector medium and E the energy of the interacting X-ray. The Fano

factor [39] describes how significantly the fluctuation in charge carrier production differ from what is expected from Poisson statistics. The Fano factors of a HPGe and SDD detector are respectively 0.12 and 0.08 [50]. Additionally, the values for w [39] are 2.96 eV in the HPGe case and 3.5 eV for the SDD. These similar values result in a lower limit for the energy resolution of these detectors which is just above 100 eV. However, it is important to note that the total energy resolution of the SDD is expected to be smaller than the HPGe detector due to the smaller detector capacitance. This results in a lower contribution from detector noise to the energy resolution.

In terms of the intensity of the escape peaks it is possible to make a clear distinction between the HPGe and the SDD case. In the case of a SDD, the X-rays will generally have enough energy to overcome the binding energy of the Si K-shell which is only 1.8 keV [19]. But, due to the very small fluorescence yield of a Si atom this vacancy will have a small probability to be filled through the emission of a characteristic K_α Si X-ray. A similar thing can be said about the L_α X-rays from the Ge crystal case. This is important because these characteristic X-rays would otherwise create intense escape peaks next to the X-ray signal because they have a high probability to escape. However, X-rays with an energy that is large enough to overcome the Ge K-shell binding energy of 11 keV [19], can produce Ge K_α characteristic X-rays which have a large probability to escape the system due to their energy of around 11 keV. Additionally, the K-shell fluorescence yield of Ge has a larger magnitude compared to the K-shell of Si which means that the escape peaks induced by the escape of the K_α Ge X-rays will be more intense. Note that this will only significantly affect the PIXE X-rays that have an energy above 10 keV.

To conclude this subsection, it is important to note that every X-ray signal in a PIXE spectrum will have a lineshape that resembles the theoretical illustration from Figure 3.11.

3.5 Conventional PIXE setup

3.5.1 Setup layout

During the time of this research, the lab only had access to the HPGe detector that was described in the previous sections. With this detector and the corresponding electronics and data acquisition system that were described in Section 3.3, the experimental setup shown in Figure 3.12 was constructed during this research. Here, an existing vacuum setup was used such that the detector could be attached to one of the connection points of the experiment chamber. The angle between the beamline and the detector is 30°, which is important to minimize the intensity of the electron bremsstrahlung.

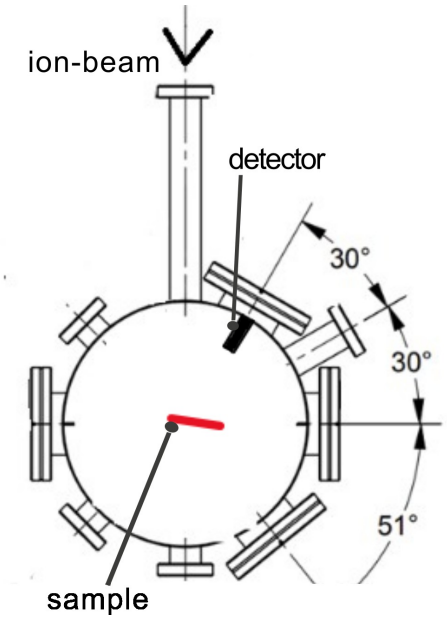

Figure 3.12: Top view of the experimental chamber in which the HPGe detector was installed to create a conventional PIXE setup.

The angular dependence of the bremsstrahlung has been investigated in many studies [51] and indicates that the intensity of this background is maximal around a detector lab frame angle of 90°. The existing IBA setup allows the user to change the vertical position of the sample holder, which is important when different PIXE measurements have to be performed on different samples. It is also possible to rotate the sample holder around the vertical rotation axis such that the angle between the sample normal and the beam direction can be adjusted. The first goal of the research is to perform PIXE test measurements and to verify the performance of the HPGe detector. The existing vacuum chamber provided the ideal option

for this purpose because one can change certain setup parameters and investigate whether the expected behavior is observed in the measurement.

Before performing any experiment, it is important to install an additional absorber layer in front of the detector. As the absorber material, we choose Mylar due to its composition of $C_8H_6O_4$ and because we had the option to increase the absorber thickness by stacking multiple 13 μm layers. The absorber is necessary to attenuate the very intense Si signal from the substrate, without affecting the higher energy X-rays too much. Without an absorber in front of the detector, the large count rate of the unfiltered Si signal would saturate the detector, cause large dead times and intense pile up peaks. The second important purpose of the absorber is to stop any beam particles that are backscattered in the sample towards the detector. These particles can damage the HPGe detector or induce signals that influence the measurement. The thickness of the Mylar absorber had to be just enough to stop the particles and attenuate a larger part of the Si X-rays. Here, the Ruthelde [52] software was used to simulate the energy loss of a 2 MeV backscattered proton and He-ion. The result of the simulations is shown in Figure 3.13 and indicates that one needs 52 μm absorber thickness in order to perform experiments with a proton beam.

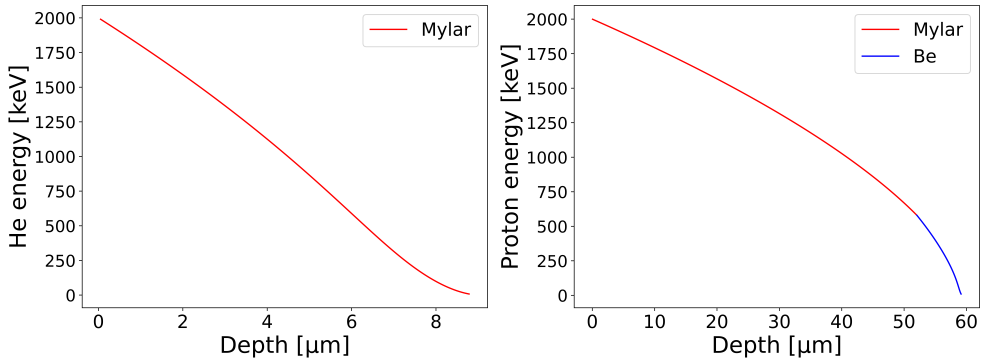

Figure 3.13: Energy loss simulations of a 2 MeV He-ion (left) and a 2 MeV proton (right) in the Mylar absorber with a thickness of 52 μm.

The energy loss calculations are performed using Bragg's rule [19] and the SRIM-2013 [53] stopping cross section values. Bragg's rule states that the total energy loss that a particle experiences in a compound is determined by the sum of the energy loss values in their individual components, weighted using the elemental concentrations. The energy loss that a 2 MeV particle would experience in the Mylar is determined at the start and is applied over the distance of one monolayer. This process is repeated with the decreased energy value for the next monolayer, until the particle is stopped. An experiment with a He-ion beam could allow for a

thinner absorber thickness but this would not sufficiently attenuate the Si X-rays, which have an energy of 1.74 keV. This can be seen from the transmission curves for different absorber thickness values shown in Figure 3.14. Transmission T of a certain X-ray energy through an absorber is defined as I/I_0, with I_0 the initial intensity of the beam. The curves are obtained using experimental attenuation coefficients from the XCOM database [47] of NIST.

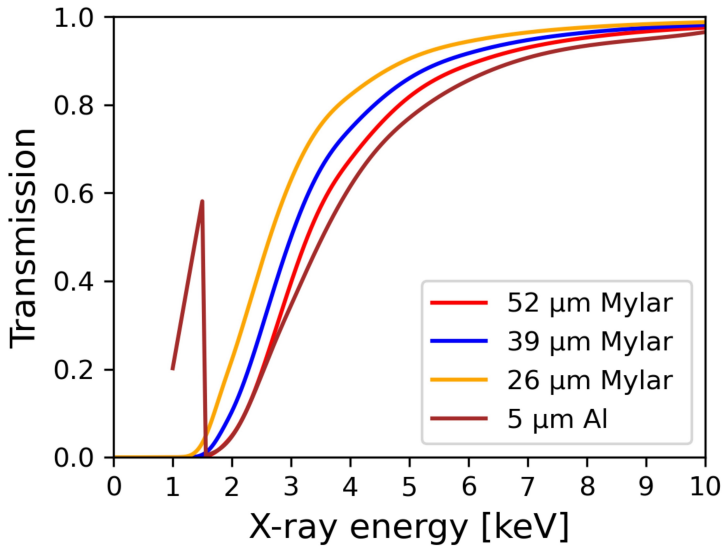

Figure 3.14: Transmission curves for different Mylar absorber thickness and for a thin aluminum absorber.

3.5.2 Setup testing

One of the first experiments was to investigate the influence of the detector solid angle on the count rate of the detector. The distance between the sample and the detector could be manually adjusted and was determined using the ruler that was installed on the detector. The starting distance between the sample and the detector was (186 ± 5) mm, when the indication on the detector ruler was at zero. The uncertainty on this distance is an estimation based on the limited ability to measure various distances. However, relative distances can be measured with a precision of 1 mm. By bringing the detector closer to the sample, one can increase the detector solid angle and perform test measurements at different detector-sample distances. Here, the detector solid angle can be approximated as [24]

$$\Omega = \frac{A_{active}}{\pi r^2},$$

where A_{active} is the detector active area of 50 mm^2 and r is the distance between the sample and the detector. The value of r was determined as

$$r = 186 - d_{ruler},$$

for which different values of d_{ruler} between 52 mm and 92 mm were used. A thick copper sample is used such that the amount of Cu K_α X-ray counts could be monitored. The measurements were performed using a 2 MeV He beam and a sample tilt angle of 10°, which resulted in PIXE spectra that are similar to what is shown in Figure 3.15.

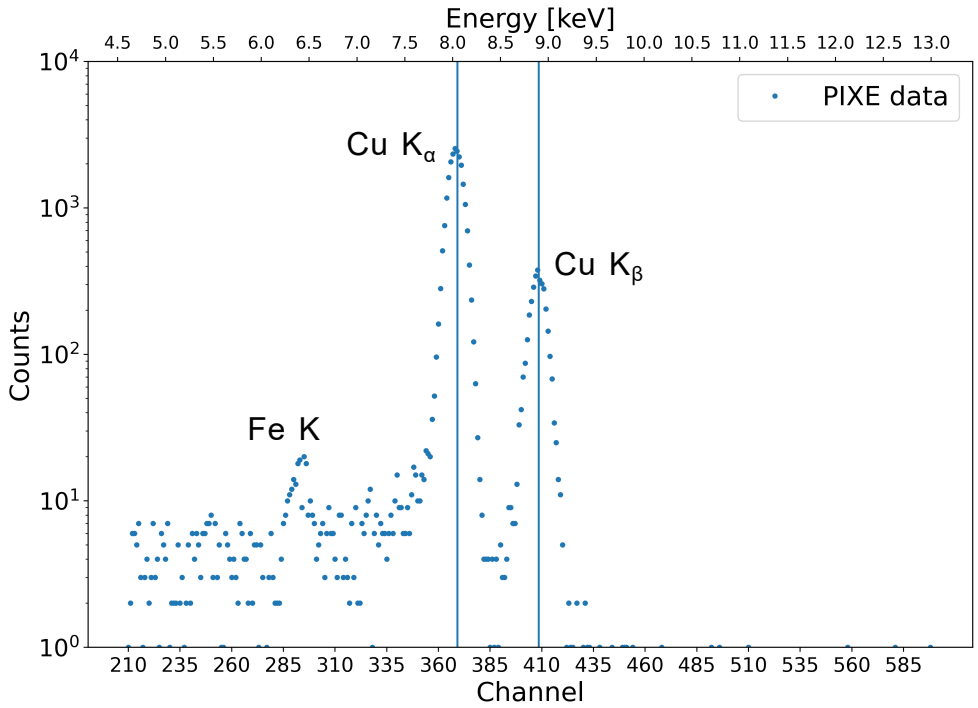

Figure 3.15: PIXE measurement of a thick Cu sample for a detector-sample distance of around 70 mm.

Important to note from Figure 3.15 is the excellent energy resolution that can be seen in the Cu K_α signal. The width of this signal corresponds to an energy resolution of 150 eV. The integrated counts under this X-ray signal are shown as a function of the distance between the sample and the detector in Figure 3.16. The results confirm to have a $1/r^2$ dependence on the distance as can be seen with the fitted function. This is as expected from Equation (2.1) which defines a linear dependence of the counts under an X-ray signal on the detector solid angle.

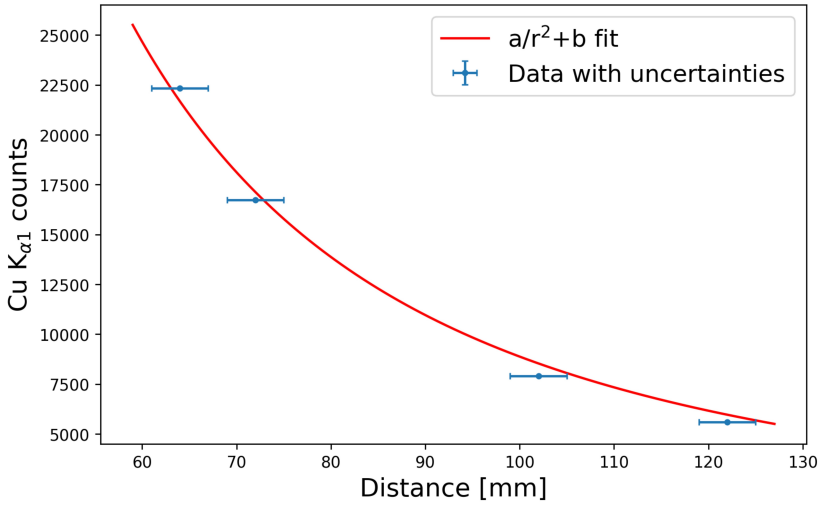

Figure 3.16: X-ray signal intensity dependence on the detector solid angle investigation.

Another experiment that can be done to test the agreement between the measurement and what is expected from the physics, is changing the angle between the beam direction and the sample normal. Here, the path length of the beam inside the thin film will be larger. This is expected to increase the number of counts in the X-ray signals from elements within the thin film and is illustrated in Figure 3.17.

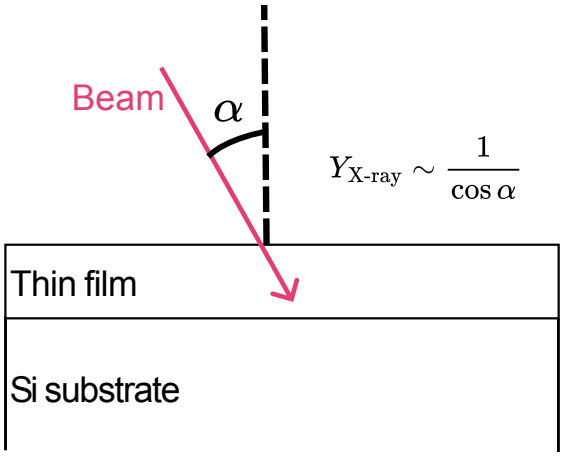

Figure 3.17: Illustration of the tilt angle α defined by the angle between the beam direction and the sample normal.

A thin film of FeCo on a Si substrate is used in the sample tilt angle experiment, where tilt angles of 10° and 80° are used. The expected increase in X-ray count

related to the larger path is determined by the $1/\cos(\alpha)$ ratio [24]. The two measured spectra are shown in Figure 3.18, where there is a clear increase in the intensity of FeCo signals from the thin film. The counts increased by a factor of $\frac{cos10°}{cos80°} = 5.6$, which is as expected from the increased path length. This implies that one can increase the measured signal intensity for a layer near the surface with a factor 5, when the sample tilt angle is changed from 10° to 80°. The low detector dead time of 1 % also confirms that the absorber is sufficient to attenuate the strong signal from the Si substrate.

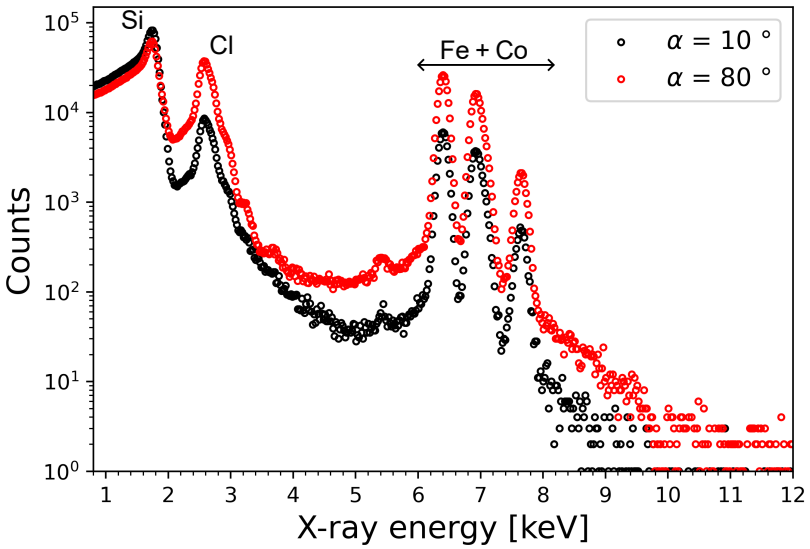

Figure 3.18: PIXE measurements of the same FeCo sample with different experimental tilt angles α.

The final performance experiment was a measurement of the detector dark current or leakage current. It is typical for semiconductor detectors to exhibit small detector currents that originate from free charges that are thermally excited from the valence band into the conduction band. The cooling that was introduced in the previous part already decreases the intensity of this current, but one should still inspect this due to the small Ge bandgap of 0.66 eV [19].

A data acquisition of 30 minutes without the presence of the ion beam in the chamber results in 3 counts for the energies higher than 1 keV. However, the spectrum does shows a small signal from dark current and electrical noise at a detector channel 10 which would correspond to an X-ray energy of 200 eV. The intensity of this signal is low and agrees with the expectations. The ramp frequency which is the time between two resets of the preamplifier voltage was around 4 to 5 seconds, depending on how long the bias voltage had been applied. This voltage increase

represents the noise and dead current that the detector is experiencing, as mentioned in Section 3.4.

The different detector performance tests that were performed show that the detector is behaving as expected. This means that the data acquisition parameters that were mentioned in Section 3.3, result in a setup that can be used to measure the X-ray signals from a thin film.

Chapter 4

Analysis software for PIXE spectra

This chapter discusses the process of analyzing PIXE spectra and converting the intensity of X-ray signals into elemental concentrations. Scientists at Guelph have developed a data analysis software called GUPIX that can be used for this exact task. To understand how this software can be used for the analysis of PIXE spectra, the fitting procedure is introduced in the first section. The counts under the fitted signal also need to be converted into concentrations. This standardization process is covered in the second section together with the uncertainty evaluation. The software abilities that are covered in both sections also motivate the choice to use GUPIX for this research.

4.1 Fitting procedure

The analysis of a PIXE spectrum is done with a computational method. Here, a model that represents the geometry, detector properties and theoretical yields can be fitted to the spectrum. The model that GUPIX [54, 55, 56, 57, 58] offers is based on the lineshape of the detector and the energy calibration parameters. This means that GUPIX does not fit a theoretical simulation to the data but either a Gaussian determined by the detector parameters. This Gaussian is used to model the detector broadening on the natural lineshape of the X-ray signal. The natural lineshape of a characteristic X-ray can be represented as a Lorentzian L defined as

$$L = \frac{\Gamma}{(x - x_0)^2 + \left(\frac{\Gamma}{2}\right)^2}, \tag{4.1}$$

where x_0 is the energy of the characteristic X-ray and Γ the natural width of the signal obtained from [59]. The detector broadening is modeled by convoluting the

Lorentzian from Equation (4.1) with a Gaussian which has a width that reflects the energy resolution of the detector [54]. The natural lineshape of the Ga K_α X-ray is shown in Figure 4.1, together with the modeled detector broadening. Note that the software needs predefined experimental details about the elements that are present inside the thin film, before a fit can be performed.

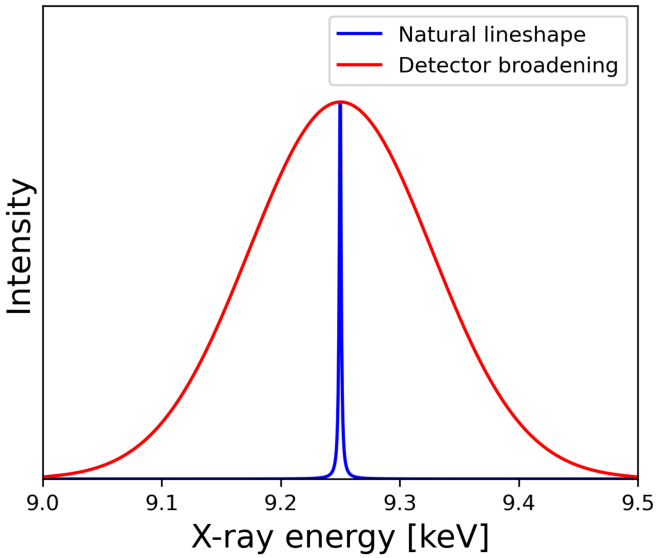

Figure 4.1: Natural lineshape of the Ga K_α X-ray and the resulting signal in the detector as the convolution of the lineshape with a Gaussian. For clarity, the intensity is normalized to have the same maximum, not the same total intensity.

The fitting procedure [54] starts by generating a Gaussian shaped signal centered around the energy of the m-th X-ray of element n. This is referred to as the principle line of the element and is defined by the user. The location of the central channel X_0 of the Gaussian is determined by the energy calibration parameters P_a and P_b of the detector which are defined as [54]

$$X_0 = P_a + P_b \cdot E_x,$$

where E_x is the actual X-ray energy. The width of the Gaussian is defined as [54]

$$\sigma = \sqrt{P_c + P_d \cdot E_x},$$

where P_c and P_d resemble the noise and the statistical nature of the charge formation that both determine the detector resolution. Generally, for HPGe detectors it has been shown [54] that $P_d = 4.6 \cdot 10^{-4} P_b$, which eliminates one of the parameters. The parameters P_a, P_b and P_c are already three of the four fit parameters that are

optimized to fit the position and width of the Gaussian's to the data. The last fit parameter in the fitting procedure is the height h of the Gaussian. GUPIX also offers the possibility to include an exponential low energy tail and a shelf in the model of the lineshape. The model parameters are then optimized by means of a conventional least-square fit to the principle peak of the element. The chi-squared for the fit is defined as [54]

$$\chi^2 = \frac{1}{d} \sum \frac{(Y - Y_{mod})^2}{\sigma_x^2}, \tag{4.2}$$

where d is the number of degrees of freedom and σ_x is the variance of the counts or yields Y in channel x. When the principle peak area is determined, the sub-peaks of the element are also simulated. Here, the software starts from the fitted principle line and converts this fitted Gaussian according to the relative fluorescence yield of each sub peak. The intensity ratio R_{mn1} of the m-th line of element n to the principle line is defined as [54]

$$R_{mn1} = N \cdot R_{mn} \cdot T_{mn} \cdot \epsilon_{mn},$$

where R_{mn} is the relative emission rate, T_{mn} the transmission of the m-th X-ray line through the absorber and ϵ_{mn} the detector efficiency for the energy of the m-th line. N is a renormalization parameter in this definition. The software also needs the absorber thickness and detector details for this conversion.

An important detail of the expression from Equation (4.2), is that the experimental X-ray signals will be superimposed on a slowly varying background caused by bremsstrahlung. GUPIX gets around this background by using a top-hat filter [54] that is optimized to filter out the slowly varying component. The filter function is shown in Figure 4.2, where UW and LW define respectively the positive filter coefficients $f_s = 1/\mathrm{UW}$ and the negative coefficient $f_s = -\frac{1}{2 \cdot \mathrm{LW}}$. It has been shown [54] that UW = 1 FWHM and LW = 0.5 FWHM are the optimal filter dimensions, where FWHM represents the full width at half max of the Gaussian.

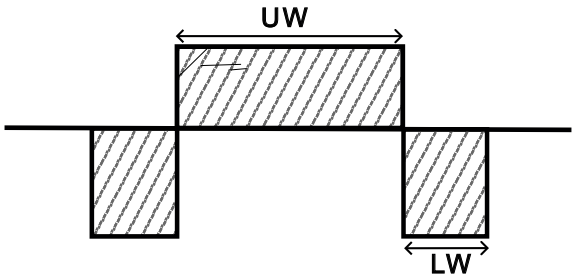

Figure 4.2: Top-hat filter function. Inspired from [54].

These filter functions are then applied to the measured data by the convolution defined as

$$\text{Filter}(Y(x)) = \sum_{s=-t}^{s=t} f_s Y(x+s),$$

where $t = \text{UW}/2 + \text{LW}$. The effect of this convolution on the raw data is illustrated in Figure 4.3. The top part of this figure represents a Gaussian shaped X-ray signal on some linear background and the bottom part is the filtered result. The fitting procedure starts by applying this filter to the spectrum after which the principle line fitting process, described at the start of this section, is applied. For this, the software needs some starting values for the calibration parameters P_a, P_b and P_c of the model which are obtained by performing a linear channel-energy fit using two visible X-ray signals in the spectrum.

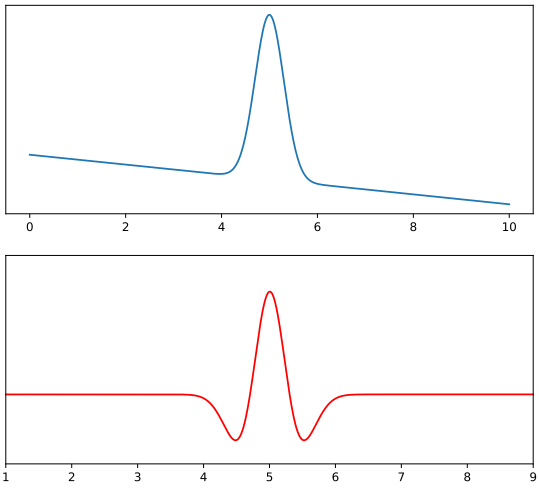

Figure 4.3: Top: Gaussian imposed on a linear background. Bottom: Result after applying the top hat filter to the blue curve. Inspired from [54].

An example of this is shown in Figure 4.4, where the spectrum had a Si K_α X-ray signal and a Ge K_α X-ray signal. The fit uses the channel number that the detector assigned to both X-ray energies and obtains a good estimation of P_a and P_b from the linear fit coefficients. These energy calibration parameters allow the software to locate the central channel of the principle X-ray line of each element. An initial guess for the height of the modeled Gaussian is obtained from the amount of counts in the peak channel of the principle line [54]. The areas of the principle lines corresponding to the elements in the thin film are then the essential

result of the fitting procedure. Applying a filter to the spectrum can affect the uncertainties of a fitting process. It is therefore important to define the uncertainties that arise from the GUPIX fitting process. In a regular unfiltered fitting procedure, one can view the variance of Y from Equation (4.2) as $\sigma_x^2 = Y(x)$ which is given by the statistical nature of the X-ray counts. However, the filter procedure implies that this variance should be modified. According to Schamber [60], the correct modification is obtained when replacing the variance in the denominator of Equation (4.2) by the approximation

$$\sigma_x^2 = \sum_{s=-t}^{s=t} f_s^2 Y(x+s).$$

The f_s coefficients from this expression are again the filter coefficients defined by the filter function that is applied to the unfiltered spectrum.

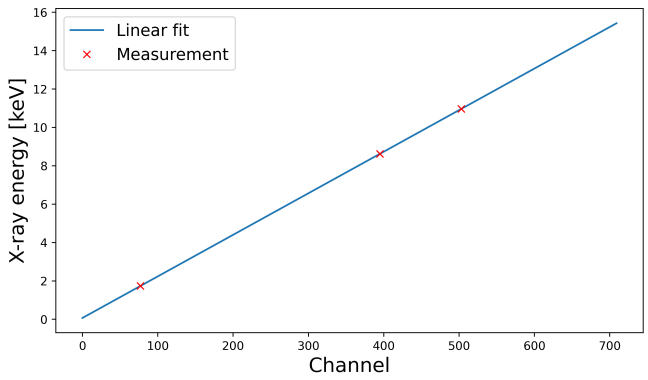

Figure 4.4: Energy calibration by means of a linear fit to the channel values of well defined X-rays in a PIXE measurement.

4.2 Uncertainty analysis

GUPIX offers two uncertainty estimates on the determined area of the principle peak. The first uncertainty is the fit uncertainty, which is determined from the squares of the diagonal element of the error matrix [54]. The filter effect on these error matrix elements corresponds to a scaling correction determined by the values of UW and LW. This fit uncertainty reflects the uncertainties in the peak height and width parameters. The second uncertainty is the statistical uncertainty, which is generally reflected by the square root of the peak area. However, this can significantly differ for peaks that have a slight overlap. The statistical uncertainty

that the software determines offers an alternative measure for the statistical error in the peak area as an attempt to take these effects into account. First, a region of interest is defined around the peak, corresponding to 2·FWHM about the central part. The total area N in this region can be written as [54]

$$N = P + O + B,$$

where P is the peak intensity, O the area of partly overlapping peaks and B the continuum background intensity. The statistical error on the determined peak area P is then defined as [54]

$$\sigma_P = \sqrt{P + 20 + 2B} + 0.01(O/P),$$

where the factor two contribution of the background reflects the error in the estimation and the subtraction. The second term in this uncertainty reflects the systematic error involved in the slight peak overlap, which is estimated as ±1 % of the overlapping area relative to the determined peak area. After performing a fit, one should always inspect the provided fit and statistical uncertainties and then combine them to obtain a total uncertainty on the fitted principle peak area.

4.3 Pile up and escape peaks

The previous discussion of the peak area fit procedure did not take into account that a fraction of the signal can also appear at different energies in the spectrum. This can happen due to pile up peaks or escape peaks which were introduced in Chapter 3 of this work. It is important that these effects are taken into account in the final peak area determination to prevent an underestimation of the elemental concentration.

GUPIX models the escape peaks from the Ge medium by providing each X-ray parent peak with an additional Gaussian displaced by the binding energy of the shell that caused the characteristic Ge X-ray. The relative intensity of the escape peak to the parent peak is determined by the fraction η of emitted Ge K or Ge L radiation which escapes from the detector defined as [61]

$$\eta = \frac{1}{2}\left(1 - \frac{\mu_{Ge}}{\mu_i}\ln\left(1 + \frac{\mu_i}{\mu_{Ge}}\right)\right).$$

Here, μ_i is the mass absorption coefficient in the Ge detector medium for a given incident X-ray energy and μ_{Ge} is the mass absorption coefficient in Ge for the energy of the characteristic Ge X-ray that could cause the escape peak. This expression reflects the fact that X-rays with a higher attenuation coefficient interact

closer to the detector surface such that the attenuation coefficient of the emitted Ge X-ray is not large enough to prevent it from escaping.

Pile up is not a detection effect but rather an artifact from the signal handling. GUPIX models this by adding an artificial element to the spectra that can have $N(N+1)/2$ lines in the case of a spectrum with N X-ray lines [54]. Each line from this artificial element can have an energy determined by the different possible combination of the X-ray energies from these N lines. Due to the fact that GUPIX takes the thin film elements as an input, it can try to fit a Gaussian pile up peak to signals that appear to be a superposition of two X-ray energies. Combining the area from the modeled escape and pile up peaks with the fitted principle peak areas, results in a more accurate area estimation of the peak from each element.

4.4 Conversion to elemental concentrations

GUPIX offers different elemental analysis schemes [55] depending on the nature of the measured sample. For PIXE measurements with thin films, it is possible to determine the theoretical X-ray yields using the X-ray production cross section calculated at the initial energy of the ion beam. This approximation can be made as long as the energy loss in the layer is only a small fraction of the initial energy. In the case of a 10 nm IGZO thin film, the energy loss of an impinging 2 MeV proton is only 0.03 % of the initial energy, which is why this approximation can be used for the measurements of this work. The conversion of the fitted principle peak area to elemental concentration is based on

$$Y_Z = C_Z \cdot t(Z) \cdot \epsilon(Z) \cdot Y_1(Z) \cdot \Omega \cdot Q, \tag{4.3}$$

which is obtained by using the thin film approximation to simplify the integral from Equation (2.1) and combining the ionization cross section and fluorescence yield in the theoretical yields $Y_1(Z)$. As noted in Chapter 2, an accurate charge measurement, detector efficiency, and transmission parametrization can allow one to convert the yields or fitted principle peak into the areal density of the element. Important to note is that the setup from Chapter 3 only provides a beam charge measurement before passing through beam defining slits. This means that only an estimation of the beam charge can be provided to GUPIX which does not allow for the conversion of peak area to accurate areal densities. In this work, we are mostly interested in obtaining relative concentrations which can be seen as relative areal densities from different elements. This can be obtained from the ratio of the fitted peak areas that correspond to the different elements which results in

$$\frac{Y_{Z_1}}{Y_{Z_2}} = \frac{C_{Z_1} \cdot \epsilon(Z_1) \cdot Y_1(Z_1) \cdot t(Z_1)}{C_{Z_2} \cdot \epsilon(Z_2) \cdot Y_1(Z_2) \cdot t(Z_2)}. \tag{4.4}$$

The fact that the beam charge and the detector solid angle have the same influence on every X-ray line from the different elements, allows one to use the expression from Equation (4.4) to convert the relative peak areas into elemental concentrations.
An example of the above described procedure is the determination of the concentrations of W and Pt in a sample with a PtW thin film layer. Here, two measurements are performed with a 2 MeV proton beam on a PtW thin film and the results are shown in Figure 4.5.

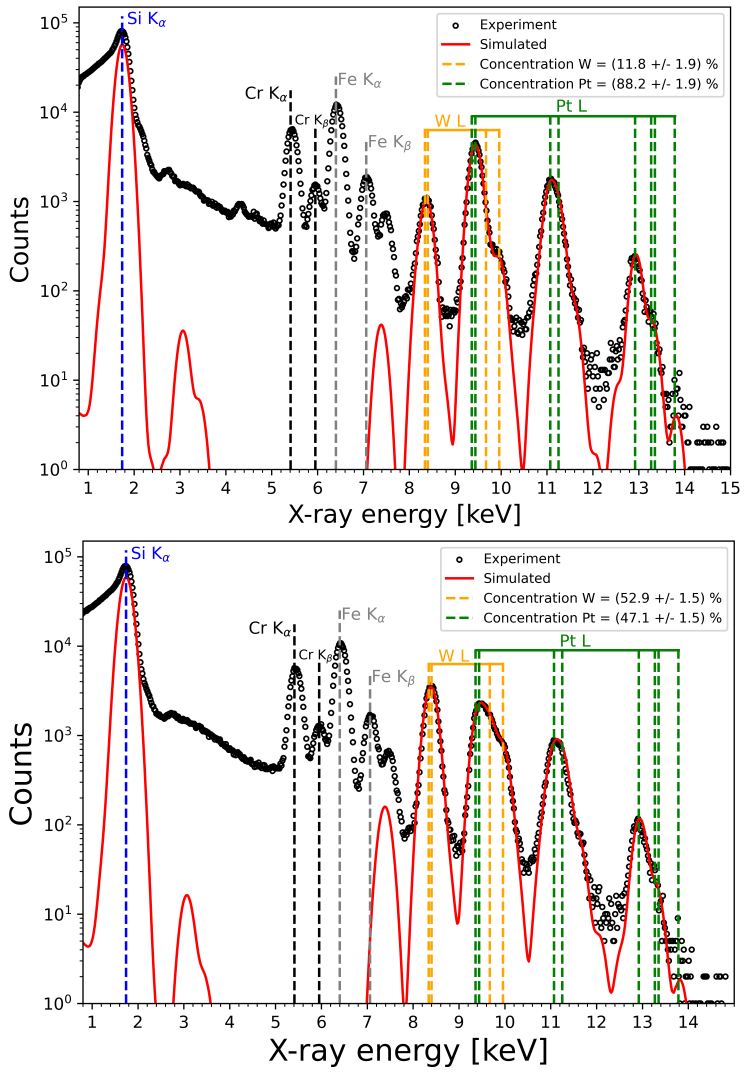

Figure 4.5: Analysis of the measured PIXE spectra from two thin film PtW samples with different concentrations. The setup from Chapter 3 was used.

Each measurement involves a PtW sample which had different Pt and W concentrations in the thin PtW layer. The spectra are obtained using the experimental setup described in Chapter 3. The fit to the spectra which used the detector parameters from the detector file of a GUL detector and the Mylar absorber thickness as input is also shown on this figure. Using the thin film approximation to convert the fitted areas into elemental concentrations, one can conclude that the experimental setup is able to capture the different Pt and W concentrations inside the two thin films. Figure 4.5 also shows that GUPIX was successful in fitting the experimental data and the uncertainties on the obtained concentrations have a realistic magnitude for a PIXE analysis.

4.5 Limit of detection

The definition of the limit detection (LOD) for PIXE has been investigated in the literature [51]. Here, the limit of detection can be understood by starting from the instrumental detection limit (IDL) defined as

$$IDL = \bar{I_{bl}} + k\sigma_{bl}, \tag{4.5}$$

where $\bar{I_{bl}}$ and σ_{bl} are respectively the number of counts in the principle peak of the X-ray and the standard deviation of the background intensity. If one defines $k = 3$ in Equation (4.5), then this implies that there is a 99% confidence level that the remaining signal after background subtraction is the peak from the characteristic X-ray. The limit of detection of an element corresponding to an X-ray signal in the spectrum is also one of the output parameters of a GUPIX spectrum fit. Here, an estimation of the minimum detectable areas of the principle peaks is provided. The calculation of this LOD is done using 3 standard deviations of the background counts in a region that is defined by 1 FWHM from both sides of the center of the Gaussian.

The background is determined by summing the difference between the spectrum counts and the modeled Gaussian over each channel in the 1 FWHM region [54]. Here, an average background B_{av} is determined which is used to limit the individual background counts in each channel such that fluctuations in individual channel background are suppressed. Calculating this average background, reducing individual channel background counts to this value and recalculating the average, has the effect of smoothing out any differences between data and fit. This provides the user with a more accurate representation of the continuum background. An overlapping peak would also have a negative effect on the LOD. This contribution is estimated by summing the differences in counts between the filtered spectrum and the modeled principle line. Combining these contributions one obtains the

uncertainty in the area which must be overcome by the characteristic X-ray peak in order to be detected. This uncertainty σ_a is given as [54]

$$\sigma_a = \sqrt{B + O} + 0.01 * O, \tag{4.6}$$

where O is the area of partly overlapping peaks, B the continuum background intensity and the second term is again reflecting a possible systematical error in the determined overlap area. The GUPIX software does then provide the LOD for each fitted principle X-ray line defined as

$$LOD = 3\ \sigma_A \approx 3\sqrt{B}, \tag{4.7}$$

where $3\sigma_A$ is the minimum detectable area at 99% confidence level [54].

When the thin film elements are inserted into the software, one can also include elements that are not present in the measured spectrum. The software will then also provide a LOD for these elements, calculated as $3\sqrt{B}$ [54]. The background parameter B is then determined as the integrated counts in the region where the X-ray line corresponding to this element would appear. These values for the LOD are very important because they dictate the minimum amount of an element that should be present inside a thin film before it can be detected.

Chapter 5

Signal to background investigation

Having acquired the necessary scientific knowledge about the test setup from Chapter 3, the next step is to study the observed signals and backgrounds that are present in the PIXE measurements. This chapter starts by introducing the reader to the theoretical framework of the ionization cross section which will be used to interpret the intensity of the X-ray signals. The theory section also discusses a semi-empirical parameterization for the bremsstrahlung that is produced in PIXE measurements with a 3 MeV proton beam. These models allow for a better understanding of the signal to background ratios that are observed. However, one needs to verify whether the experimental spectrum is free of any additional background that could be caused by the experimental setup. The second section will thus start by studying the external background signals and their dependence on the beam properties. After having reduced the external background sources, one can investigate the remaining background using the semi-empirical bremsstrahlung parameterization from the theory chapter. Lastly, the chapter ends with a combined picture of the signal to background ratios for PIXE experiments with a proton beam against the measurements with a He-ion beam.

5.1 Theory

5.1.1 ECPSSR

The most accurate theory for the calculation of inner shell ionization cross sections is called energy loss coulombian perturbative steady state relativistic (ECPSSR) theory [62]. The model starts from the PWBA, that was introduced in Chapter 3, to calculate the ionization cross section but now the perturbation Hamiltonian is

represented by the coulomb field in the interaction between the projectile and the inner shell electron. In this approximation, the ionizing particle is described by a planar wave before and after the ionization process. The ionization cross section in the PWBA behaves as [63]

$$\frac{d\sigma(\Omega)}{d\Omega} \sim 8\pi z^2 \left(\frac{e^2}{\hbar v}\right)^2, \tag{5.1}$$

where z is the atomic number of the projectile and v is the relative velocity of the projectile and the electron. Then, the model uses specific correction factors [64] to correct for the approximations that were made in this PWBA calculation. The correction factors consist of a coulomb deflection factor [65] which corrects the approximation of the initial and final state projectile as planar waves. This correction is significant in the case of heavy target elements. The model [64] also corrects for the binding energy, the energy loss of the projectile [66] and relativistic effects in the wave function of the inner shell electron.

For the study done in this work, the ionization cross section can be determined with the ISICS software [67, 68] which uses numerical integration methods to calculate the PWBA cross section and corrects it with correction factors from a database. The software allows the user to determine ionization cross sections for different target-projectile combinations as a function of projectile energy, which is useful to understand the intensity of the signals in a PIXE measurement.

5.1.2 Semi-empirical bremsstrahlung model

The cross sections of the bremsstrahlung background processes, that were introduced in Chapter 2, are complex since they not only depend on the energy of the projectile but also on the energy of the produced bremsstrahlung X-ray. However, Murozono and Ishii [35] derived approximate functions that were fitted to the theoretical background cross sections induced by a 3 MeV proton beam in different targets. The functions are given by

$$\begin{aligned}
\ln(\sigma^{SEB}) &= \sum_{i=0}^{5} P_i^{SEB} \hbar\omega^i \\
\ln(\sigma^{QFEB}) &= \sum_{i=0}^{5} P_i^{QFEB} \hbar\omega^i \\
\sigma^{AB} &= \exp\left(\sum_{i=0}^{1} P_{i+1}^{AB} \hbar\omega^i\right) + \exp\left(\sum_{i=0}^{1} P_{i+3}^{AB} \hbar\omega^i\right),
\end{aligned} \tag{5.2}$$

with $P_i^X = \sum_{k=0}^{3} p_k^i Z^k$. Here, p_k^i are the obtained fit parameters from the fit to the theoretical cross section, of bremsstrahlung process X, corresponding to a target with atomic number Z. The values of the p_k^i coefficients are given in the literature. Note that the approximate function of atomic bremsstrahlung in Equation (5.2) consists of two terms. These terms represent the AB from K- and L-shell electrons.

This model allows for the quick calculation of the production cross sections from the bremsstrahlung processes in different target, which is useful for the interpretation of the background that is observed in PIXE measurements. The main drawback is that these cross sections are only valid for the case of a 3 MeV proton beam instead of the 2 MeV proton and He-ion beams that is used in this chapter. However, these cross sections can be seen as an upper limit since the intensity of the background has been shown to scale with the beam energy [69]. The approximate curves in the case of silicon are shown in Figure 5.1.

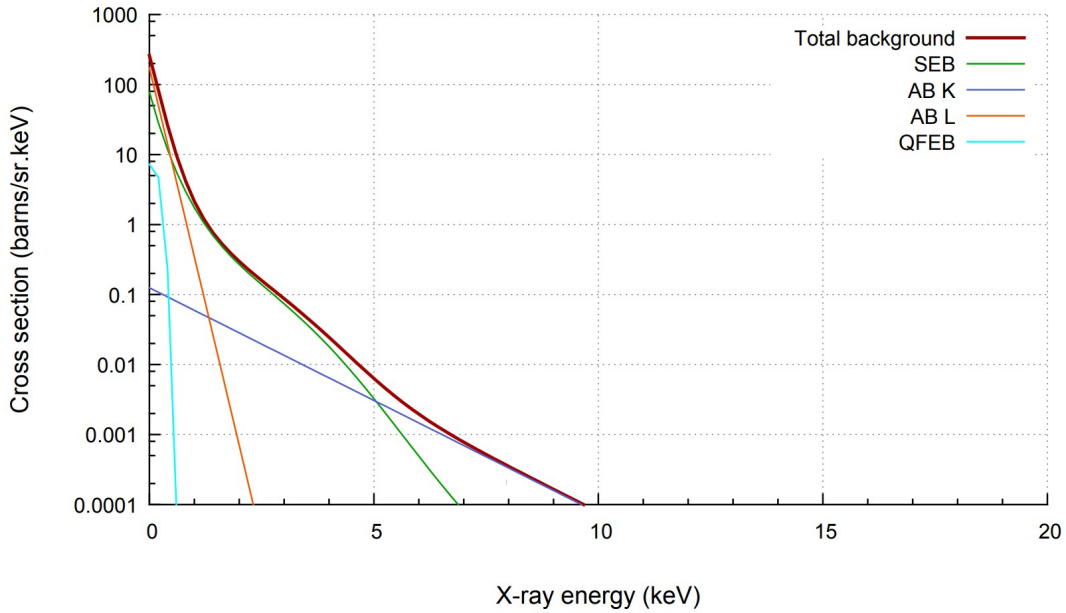

Figure 5.1: Theoretical electron bremsstrahlung production cross sections of QFEB, SEB and AB for a 3 MeV proton beam in silicon. Calculated using the fit parameters from [35] in the approximate functions.

5.2 Proton versus He beam measurements

5.2.1 Experiment chamber background

In the initial PIXE measurements of this work, the spectra always contained very intense signals from Cr, Fe and Ni X-rays. The signals were present even when samples were used that did not contain any of these elements, as can for example be seen in Figure 4.5. Additionally, the signals seemed to decrease in intensity when a He-ion beam was used. It was recognized that each of these elements can be present in the walls of the experimental chamber or in the sample holder of the setup. If this background is the result of X-rays that are created in the walls of the experiment chamber, then this difference can be understood by considering two things.

Firstly, a beam particle can only reach the walls of the chamber after one or multiple scattering events in the sample. An elastic scattering event of a 2 MeV He-ion or proton on a Si atom results in an energy of respectively 1.1 MeV and 1.7 MeV. The calculation of these energies was done using SIMNRA [70]. This difference in energy can be explained by the larger mass of the He-ion compared to the proton, which allows more energy to be transferred to the Si nuclei. Neglecting any additional energy loss, one can assume that a He-ion and a proton with these energies reach the walls. The second consideration is the energy dependence of the ionization cross section. The importance of this energy dependence is illustrated in Figure 5.2.

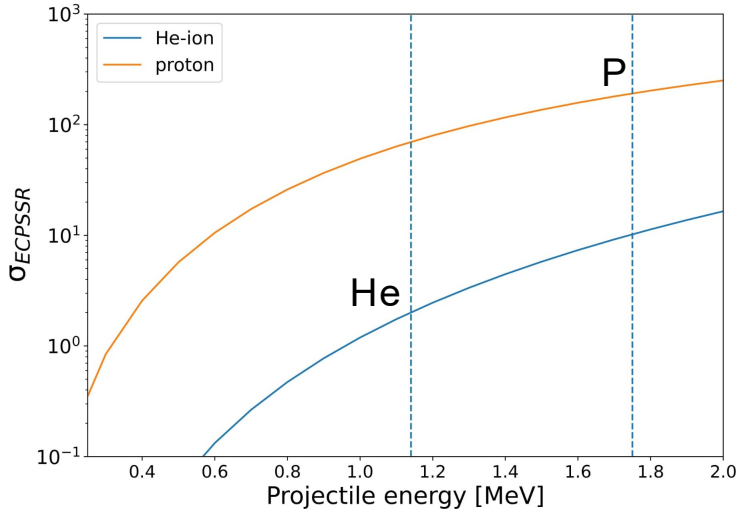

Figure 5.2: Theoretical K-shell ionization cross sections of Fe for a He and proton beam as a function of their energy. Calculated using the ISICS software [68].

In an attempt to shield the detector from these external X-rays, a plastic tube was designed to serve as a shield in front of the detector. This resulted in the PIXE proton spectra shown in Figure 5.3, where the distance between the shield in front of the detector and the sample was varied. The spectra illustrate how the shielding does seem to have some effect on the Fe, Cr and Ni signals when the detector is brought closer to the sample. The intensity from the signals corresponding to the elements in the sample did increase for the measurement with a smaller detector-sample distance which is as expected from the solid angle test of Chapter 3. The fact that the intensity of the other X-rays decreased does not only prove that the shield works but also that the Fe, Cr and Ni X-rays do not originate from the sample.

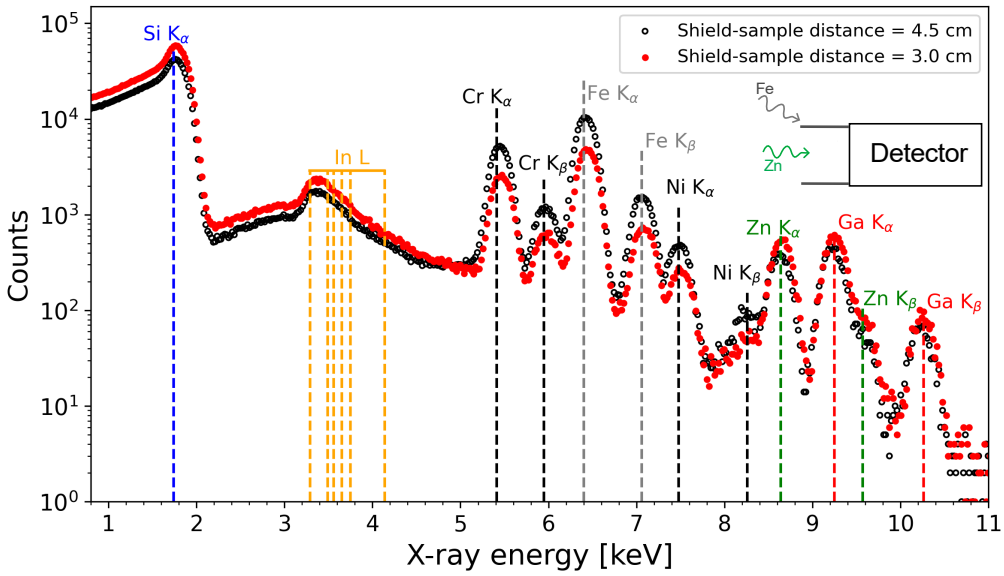

Figure 5.3: PIXE measurements of an IGZO sample with an additional shield in front of the detector. Each measurement has a different distance between the sample and the shield.

However, the remaining intensity of the external X-ray signals in Figure 5.3 indicates that these X-rays do not only originate from the chamber. The last possible part of the setup which could contain these elements is the sample holder. To investigate this hypothesis, a plastic foil was used to cover the sample holder such that the beam could only produce X-rays from the sample. Ions interacting with the plastic can only induce characteristic X-rays with an energy below 300 eV due to the light elements that are present in the plastic. This resulted in the PIXE spectrum, which is shown in Figure 5.4 together with the measurement without a plastic cover.

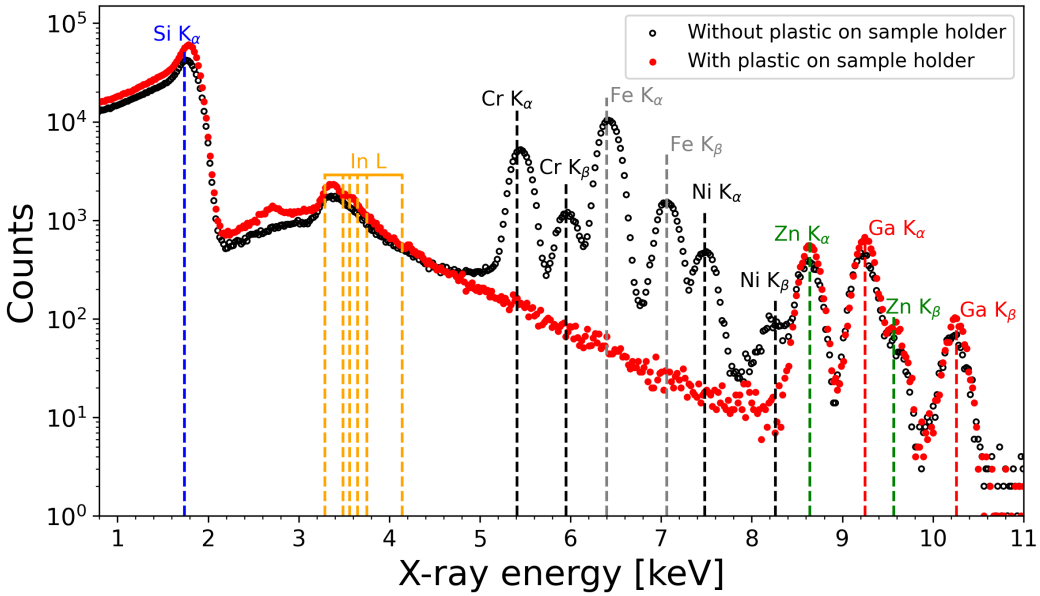

Figure 5.4: PIXE measurement of IGZO sample with and without a plastic foil to cover the sample holder.

Finally, the contribution from the external X-ray signals is significantly reduced. This was unexpected because the beam should only interact with the sample due to the fact that its extent is defined to be$\sim$ 1 mm after passing through beam defining slits. A final test without a plastic cover on the holder and the slits fully opened, resulted in the same effect as shown in Figure 5.4. This insight leads to the conclusion that a large part of the external X-rays are the result from protons interacting with the holder after a small angle scattering event at the slits. This scattering could increase the extent of the beam. Nevertheless, this origin is also in agreement with the less intense external X-ray signal that was observed for the He-ion beam case. This can again be explained by the fact that He-ions will loose more energy compared to the protons in the small scattering events at the slits, resulting in small He ionization cross sections due to the large relative velocity difference between the He ion and the inner shell electron. This effect comes from the velocity dependence shown in Equation (5.1).

With the source of the external background being eliminated, the remaining X-rays are governed by the elements in the sample and the slowing down of the projectile in the Si substrate.

5.2.2 Electron bremsstrahlung

The bremsstrahlung model from the theory section is only valid for a proton beam energy of 3 MeV. However, since the intensity of the bremsstrahlung background has been shown to scale with the initial beam energy, one can interpret these cross sections as an upper limit for the case of 2 MeV proton PIXE measurement. Using the basic picture that is provided in Chapter 2, the extent of the SEB contribution is influenced by the amount of energy that a 2 MeV proton can transfer to an electron at rest. This maximal energy is 6.5 keV but the bremsstrahlung background from figure 5.4 is present up to 10 keV. The bremsstrahlung X-rays above 6.5 keV are regarded in the literature as coming from electrons that already had a velocity before the interaction.

The literature [36] states that SEB is the dominant contribution in between 2 and 6 keV. With this knowledge, one can try to fit an exponential function to the background in this region. The approach of fitting an exponential to the background is inspired by the work of Wittmaack [69] and also by the semi empirical model from the theory section. The result of the fit in the case of an IGZO PIXE measurement is shown in Figure 5.5.

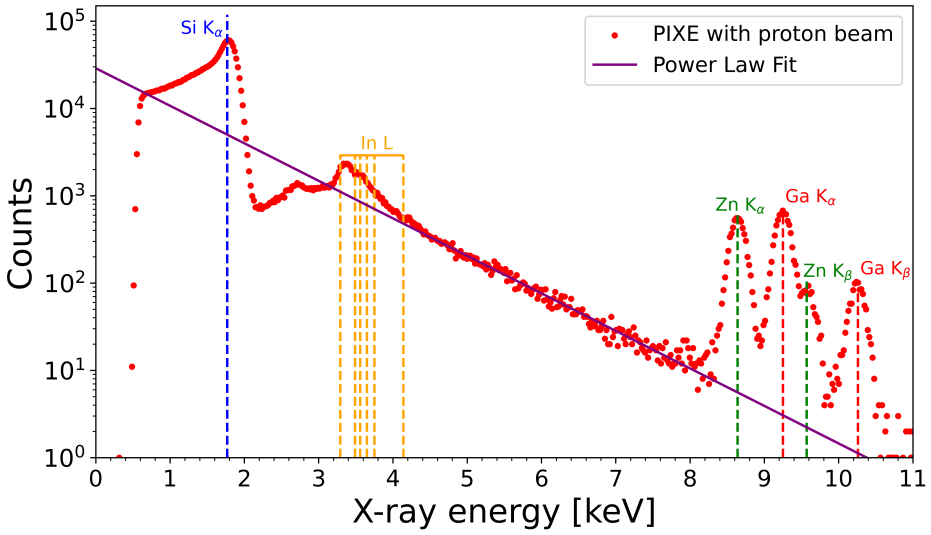

Figure 5.5: PIXE measurement of an IGZO sample obtained with 2 MeV proton beam. The low energy bremsstrahlung fit is shown in red together with the data.

One can clearly observe a good agreement between the exponential fit and the spectrum. However, the intensity of the background starts to decrease at energies lower than 3 keV and does not follow the expected signature of the SEB cross section resembled by the exponential fit. This is understood to be the result of the

Mylar absorber in front of the detector. The total background intensity $Bg(E)$ at a given X-ray energy E is given by

$$Bg(E) = \sigma_{brem}(E) \cdot T(E) \cdot \epsilon_{det}(E),$$

where T is the transmission through the Mylar absorber that was discussed in Chapter 3 and $\epsilon_{det}(E)$ the detector efficiency. The decrease in background intensity around 3 keV is thus the result of the X-ray energy dependence of the transmission beginning to overcome the background bremsstrahlung cross section energy dependence. The absorber influence on the background was not visible in the fit energy region because the transmission curve from Figure 3.14 reveals that mostly the low energy X-rays are attenuated.

The background in the PIXE measurement with a proton beam can be compared to the measurements with a He-ion beam that are shown in Figure 5.6. The background shape and intensity from this spectrum is clearly different from the proton beam case. However, this can be expected from the literature [34]. In the

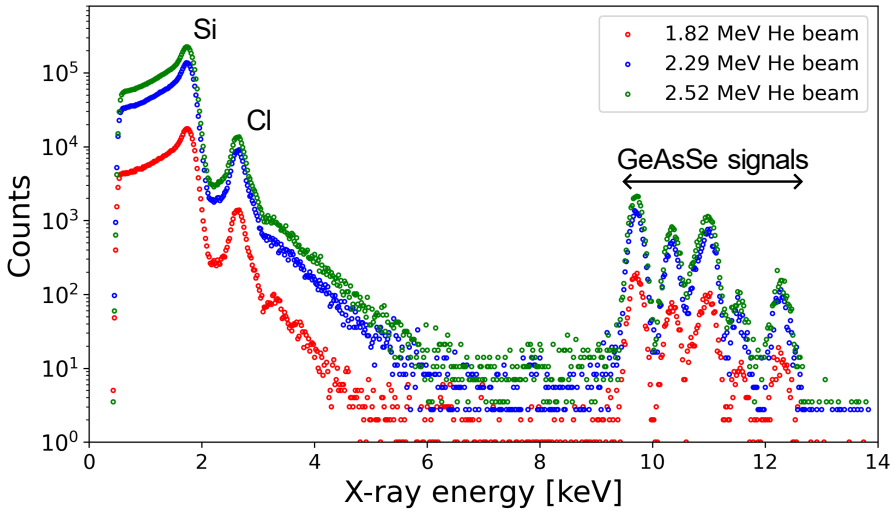

Figure 5.6: PIXE measurement of a GeAsSe sample obtained with He ion beams of different initial energies.

work of Ishii, the cross sections of the electron bremsstrahlung background from a proton and a He beam were compared as a function of projectile velocity. This way, Ishii illustrated that the cross sections for the same velocity are similar. This implies that the difference in background intensity with the proton beam case is again caused by the fact that the $\sim$ 2 MeV He ions have a smaller velocity than the 2 MeV protons. The dominant SEB contribution in the bremsstrahlung background is the result of electrons that are ionized from their shell and the amount of

these electrons is determined by the ionization cross section from Equation (5.1). The velocity dependence of this cross section is thus one of the determining factors for the background intensity difference in the proton versus He-ion comparison.

Important to note before moving to the next subsection is the low energy background that is visible at energies below the Si X-ray. This intense background is visible in both the proton beam case of Figure 5.5 and the He-ion beam case of Figure 5.6. The interesting thing is that it seems unlikely that this background is the result of bremsstrahlung, since the energy limit of the QFEB contribution is expected to be below 1 keV based on the curve from Figure 5.1. More measurements have to be performed in order to find the exact origin of this background.

5.2.3 Signal to background comparison

The insights from the previous sections can be combined in a general signal to background comparison between PIXE with a proton and a He ion beam. This can be done by investigating the signal to background ratios that are observed in the PIXE measurements from Figure 5.7. The spectra from Figure 5.7 are

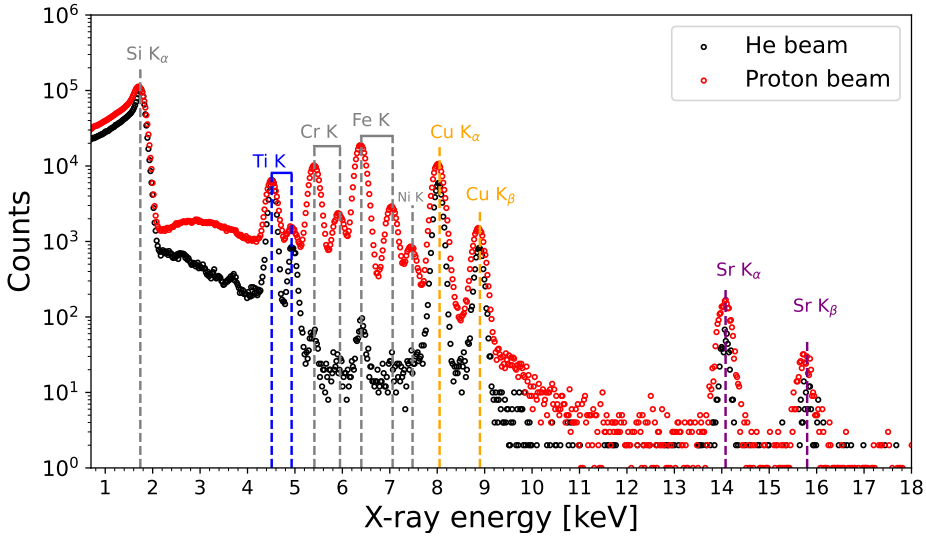

Figure 5.7: Comparison of proton and He ion beam PIXE measurements of a SrTiO sample.

measured from a thin film of SrCuTi on a Si substrate, where a 2 MeV proton and He-ion beam are used. The bremsstrahlung background is less intense in the He-ion beam case, as was observed in the previous subsection. The strong external X-ray

signals from Fe, Cr and Ni that were discussed at the start of this section are also clearly visible in the proton beam PIXE measurement of Figure 5.7. In order to investigate the influence of the nature of the beam on the signals from the elements inside the thin film, one can analyze both spectra with GUPIX and compare the obtained counts under the respective signals. The results of this analysis for the spectra of Figure 5.7 are shown in Figure 5.8. Here, Y_P are the X-ray signal counts in the proton case and Y_{He} in the He-ion beam case. The results in this figure are

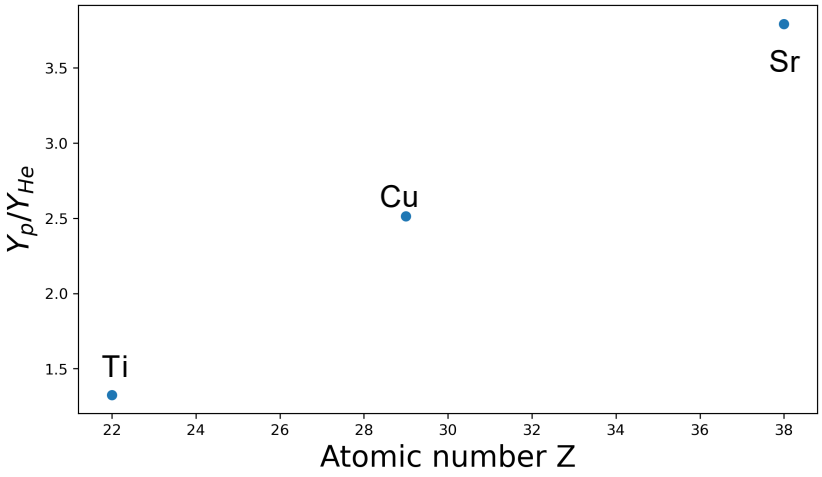

Figure 5.8: Ratio of the 2 MeV proton and He-ion beam X-ray counts under the PIXE signals from the elements inside a SrCuTi thin film.

crucial to understand the beam influence on the characteristic X-ray signals. The ratio Y_p/Y_{He} for a given thin film element with atomic number Z is determined by

$$\frac{Y_p}{Y_{He}} = \frac{Q_p \cdot \sigma_p(Z)}{Q_{He} \cdot \sigma_{He}(Z)}, \tag{5.3}$$

where Q is the beam charge and σ_p the ionization cross section for the K-shell of an element with atomic number Z. The expression from Equation (5.3) is obtained using the relation from Equation (4.3). The conventional PIXE setup from Chapter 3 does not provide an accurate beam charge measurement but both of the measurements from Figure 5.7 had a similar beam charge before passing through the slits. Nevertheless, the decreasing trend in the yield ratio's for the lighter elements in Figure 5.8 can only be the result of a changing ionization cross section. This is the case because the beam charge ratio for each element remains constant because the beam current has the same effect on every signal from an element that is present inside the thin film. For the heavier elements, one observes that the proton beam measurement has the advantage. This is expected from the fact

that a proton of 2 MeV will have a larger velocity than a He-ion of the same energy combined with the relative velocity dependence from Equation (5.1). However, the significance of the advantage that the proton beam offers compared to the He-ion beam seems to decrease for the lighter elements. A possible explanation for this behavior is the fact that the inner shell electrons of hydrogen like atoms have a velocity v that scales as $v \sim Z$ [19]. This implies that the lower velocity of the 2 MeV He-ion becomes more comparable to the velocity of the inner shell electrons, causing the ionization probability to increase. Here, the dependence of Equation (5.1) on the projectile atomic number starts to overcome the velocity dependence.

The results from Figure 5.8 indicate how a He-ion beam can become more useful for the characterization of light elements with PIXE measurements. However, the inability of the conventional PIXE setup to measure the beam current makes it hard to accurately determine the atomic numbers range for which the He-ion beam is more efficient compared to the proton beam. On the other hand, the background comparison from the previous section indicates that He-ions do induce a less intense bremsstrahlung background compared to the protons. From these two insights, one can conclude that PIXE measurements with 2 MeV He-ion beam would result in an improved signal to background ratio for the elements with an atomic number below $Z = 21$. The large ionization cross section of the 2 MeV proton beam is expected to result in a better signal to background ratio for elements between Z=25-49 due to the low background intensity at the energies of their K-lines. Generally, the signal to background ratio is not a good parameter to investigate the influence of the beam nature on PIXE measurements because the signal of a characteristic X-ray is dependent on the concentration inside the thin film, while the background at the same energies is not. This is why the ranges that are stated in this paragraph are mostly based on the comparison of the characteristic X-ray signals. These ranges are also based on the fact that the larger ionization cross section of the proton beam allows the experimentalist to measure for a shorter amount without affecting the counting statistics of the experiment.

The atomic number ranges stated from the previous paragraph have to be more accurately defined in further research. In this context, a setup that can provide a more accurate beam current measurement can be used such that it becomes possible to compare the signal intensities from the proton and He beam PIXE measurements.

Chapter 6

Conventional PIXE applications

After investigating the influence of the beam on the signals and the background of the PIXE measurements, the setup from Chapter 3 can be used to determine elemental concentrations inside a thin film. The GUPIX software from Chapter 4 can again be utilized for the analysis of the PIXE measurement. To illustrate the strength of PIXE, the research focus is on the characterization of IGZO and GeAsSe thin films that were described in Chapter 1. However, in order to determine accurate values of absolute concentrations instead of relative concentrations, one needs to first calibrate the PIXE setup. The setup calibration process is discussed in the first section of this chapter, as one of the approaches in state of the art PIXE. The second section discusses the analysis of a GeAsSe thin film using a self-consistent approach. Here, the strength of conventional PIXE is used to extend the characterization results that were obtained with RBS and ERD. This results in an accurate characterization of a GeAsSe thin film which is an important example of how conventional PIXE can already be used without moving to a substrateless setup.

6.1 Setup calibration for IGZO sample analysis

In Chapter 2, it was stated that PIXE can be used to determine concentrations of elements in a thin film. However, this can only be done when accurate beam charge measurements and solid angle values are provided. The conventional PIXE setup that was built for this work does not offer these properties. In addition, large uncertainties in the ionization cross section and fluorescence yields databases cause the need for standard measurements that are used as a reference. Here, one can use RBS measurements to calibrate the PIXE setup such that the obtained concentrations are converted in absolute concentrations. For this, a sample containing the element of interest and a reference element is used. The same technique of

elemental calibration has previously been done in the work of Harayama et al. [71] but this calibration is unique for every PIXE setup.

In order to calibrate the PIXE setup, one has to define the correction factor h for a given element as

$$h_{\mathrm{el/ref}} = \frac{C_{\mathrm{PIXE}}(\mathrm{el})}{C_{\mathrm{PIXE}}(\mathrm{ref})} \frac{C_{\mathrm{RBS}}(\mathrm{ref})}{C_{\mathrm{RBS}}(\mathrm{el})}. \tag{6.1}$$

Here, $C_{\mathrm{PIXE}}(\mathrm{el})$ and $C_{\mathrm{PIXE}}(\mathrm{ref})$ are the concentrations that are derived from a GUPIX fit to the PIXE measurement of a sample containing a thin film of the element of interest and the reference element. The analysis procedure is the same as discussed in Chapter 4. The other concentrations in Equation (6.1) are from RBS measurements of the same sample. Important to note is that a well-calibrated PIXE setup would yield $h_{\mathrm{el/ref}} = 1$ for every element present in a measurement because the concentration of the element would be the same as that obtained from the RBS measurement. The definition from Equation (6.1) assumes that RBS can determine absolute concentrations because the correction factor is then used to correct the PIXE concentration.

In this section, the discussion is directed towards the calibration of the conventional PIXE setup from Chapter 3 for the accurate characterization of IGZO samples. To achieve this, three samples have to be analyzed, one for each of the InGaZn elements, with PIXE and RBS measurements. Each sample will contain an additional Ti layer as the reference element which was specified in Equation (6.1). The PIXE experiments are performed with a 2.3 MeV proton beam and the RBS measurements use a 1.52 MeV He-ion beam. Examples of the results from the PIXE measurement on the Ti/Zn calibration sample and the RBS measurement on the Ti/Ga calibration sample are shown in Figure 6.1. These spectra illustrate the choice of Ti as the reference element for the calibration procedure. The Ti signal in the RBS and PIXE spectra does not overlap with any of the other elemental signals.

The elemental concentrations which are determined from the PIXE spectra of the Ti/Zn, Ti/Ga and Ti/In calibration samples are shown in Table 6.1. These are the concentrations that are used for the calculation of $h_{\mathrm{Zn/Ti}}$, $h_{\mathrm{Ga/Ti}}$ and $h_{\mathrm{In/Ti}}$. With the concentrations obtained from the RBS results on the same samples, the calibration factors can be calculated. The relative uncertainties on these correction factors are obtained using the expression

$$\frac{\Delta h_{\mathrm{el/ref}}}{h_{\mathrm{el/ref}}} = \sqrt{\left(\frac{\Delta C_{\mathrm{PIXE}}(\mathrm{el})}{C_{\mathrm{PIXE}}(\mathrm{el})}\right)^2 + \left(\frac{\Delta C_{\mathrm{PIXE}}(\mathrm{ref})}{C_{\mathrm{PIXE}}(\mathrm{ref})}\right)^2 + \left(\frac{\Delta C_{\mathrm{RBS}}(\mathrm{el})}{C_{\mathrm{RBS}}(\mathrm{el})}\right)^2 + \left(\frac{\Delta C_{\mathrm{RBS}}(\mathrm{ref})}{C_{\mathrm{RBS}}(\mathrm{ref})}\right)^2},$$

where $\Delta C_{\mathrm{PIXE}}(\mathrm{el})$ and $\Delta C_{\mathrm{PIXE}}(\mathrm{ref})$ are the uncertainties which are stated in Table 6.1.

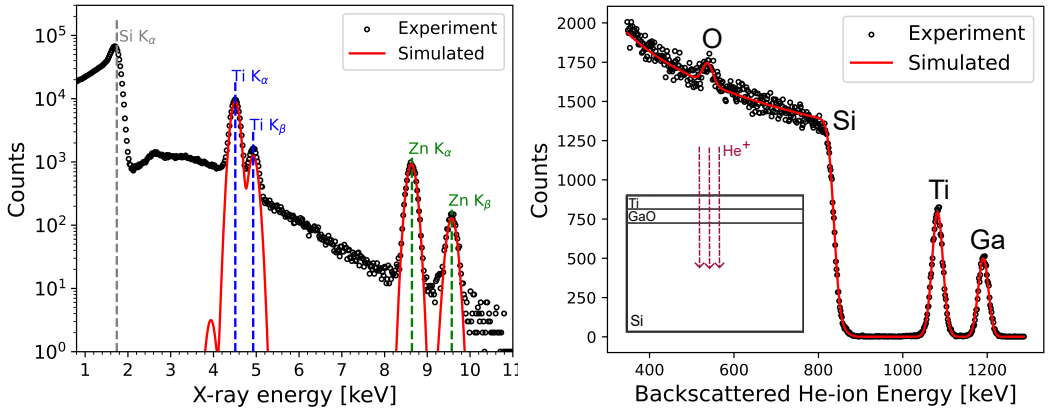

Figure 6.1: Right: RBS measurement of the Ti/Ga calibration sample together with the simulated spectrum. Left: PIXE spectrum of the calibration sample with Ti on top of Zn. Ti is the reference element for the calibration procedure.

ref/el sample	$C_{\mathrm{PIXE}}(\mathrm{el})$ [%]	$C_{\mathrm{PIXE}}(\mathrm{ref})$ [%]
Ti/Zn sample	31.36 ± 1.62	68.64 ± 1.62
Ti/Ga sample	27.50 ± 1.84	72.50 ± 1.84
Ti/In sample	17.76 ± 1.63	82.24 ± 1.63

Table 6.1: Obtained concentrations from the PIXE measurements of the three calibration samples.

For the accurate characterization of an IGZO sample, the obtained elemental concentrations need to be corrected with respect to an element that is present in the thin film and not with respect to Ti. However, the definition of the correction factor from Equation (6.1) allows one to use the relation

$$h_{\mathrm{Ga/Zn}} = \frac{h_{\mathrm{Ga/Ti}}}{h_{\mathrm{Zn/Ti}}}.$$

From the calculated values of $h_{\mathrm{Zn/Ti}}$, $h_{\mathrm{Ga/Ti}}$ and $h_{\mathrm{In/Ti}}$ one can determine $h_{\mathrm{Ga/Zn}}$ and $h_{\mathrm{In/Zn}}$. Applying these correction factors to the concentrations of Ga and In, obtained from a PIXE measurement with the conventional PIXE setup from Chapter 3, would result in accurately determined concentrations. The concentration of Zn remains uncorrected because concentrations are relative to each other. The obtained correction factors for IGZO samples are shown in Table 6.2.

$h_{\mathrm{Ga/Zn}}$	$h_{\mathrm{In/Zn}}$
1.024 ± 0.030	0.664 ± 0.020

Table 6.2: Results of the calibration process for the accurate characterization of IGZO thin films.

The correction factors from Table 6.2 give an indication of how well the detector efficiency and the transmission through the absorber were modeled. The $h_{\mathrm{Ga/Zn}}$ correction factor is close to unity and indicates a correction of 2.4 % to the obtained Ga concentration of an IGZO sample. The magnitude of this correction is expected from the 1-3 % uncertainty in the database for the K-shell ionization cross section that GUPIX uses for the analysis. However, the $h_{\mathrm{In/Zn}}$ correction factor suggests that a correction of 43.6 % should be applied to the In concentration. One aspect that could account for this large correction is the 5-15 % uncertainty in the database for L-shell ionization cross sections. This is the case because the L-lines of indium were used to determine the concentration of indium in the calibration sample.

On the other hand, the large correction could also reflect an improper detector efficiency modeling. This can be understood by inserting the PIXE yield expression from Equation (4.3) in Equation (6.1), which results in

$$h_{El/Ref} = \frac{Y(\mathrm{El})}{Y(\mathrm{Ref})} \cdot \frac{\varepsilon(\mathrm{Ref}) \cdot t(\mathrm{Ref}) \cdot Y_1(\mathrm{Ref})}{\varepsilon(\mathrm{El}) \cdot t(\mathrm{El}) \cdot Y_1(\mathrm{El})} \cdot \frac{A_{\mathrm{RBS}}(\mathrm{Ref})}{A_{\mathrm{RBS}}(\mathrm{El})}.$$

The previous paragraph discussed the influence of the theoretical yields Y_1 on the correction factor but did not take the detector efficiency and absorber transmission into account. The incorrect modeling of the detector efficiency would not be noticeable in the $h_{\mathrm{Ga/Zn}}$ correction factor because the X-rays energies from Ga and Zn are comparable to each other. The fact that these X-ray energies are already in the regime where the detector efficiency is close to unity also support this statement. On the other hand, the indium L-line that was used for the calibration has an energy of 3.24 keV compared to the 8.62 keV energy of the Zn K-line. The detection efficiency of these low energy X-rays starts to heavily depend on the thickness of a possible Ge dead layer or of the metal detector contacts. It is thus possible that the large correction factor is related to the fact that the Ge dead layer value that was mentioned in Chapter 3 is rather an underestimation of the reality.

6.2 Self-consistent approach

In the case of sample characterization it is often beneficial to combine the obtained results from different IBA analysis experiments of the investigated sample. This is most effective when done in a self-consistent way, where the strengths of each IBA technique are utilized to obtain a complete and accurate characterization of the sample. The concept of a self-consistent approach has been investigated in the literature [72, 73] and is sometimes also referred to as Total-IBA. In this section, the aim is to apply this approach for the analysis of a GeAsSe thin film using the conventional PIXE setup from Chapter 3. The approach will involve the combination of RBS, ERD, and PIXE measurements of the GeAsSe thin film but the discussion is mostly oriented toward the usefulness of PIXE, rather than a detailed discussion of the RBS and ERD results.

The RBS experiment was performed with a 1.52 MeV He-ion beam and the energies of the backscattered He-ions are shown in the RBS spectrum of Figure 6.2. The bottom part of Figure 6.2 shows the result of the conventional PIXE measurement of the same GeAsSe sample with a 2.3 MeV proton beam. From the RBS spectrum, one can clearly observe how the energies of the backscattered He-ions from Ge, As and Se atoms do not serve as a suitable parameter to distinguish the individual contributions to the spectrum. The signals corresponding to the three elements result in a combined signal from which the total integrated counts can be used to determine the combined areal density of the three elements or, in other words, the total number of atoms per square centimeter. This is illustrated by the simulated fit to the experimental data which is also shown in Figure 6.2, where the individual simulated contributions from Ge, As and Se are shown in different colors. There is no guarantee that these individual signals resemble the reality because the simulation only has the combined signal to fit.

However, the characteristic X-rays prove their worth as unique atomic fingerprints, because the individual contributions from Ge, As and Se to the PIXE spectrum from Figure 6.2 can be distinguished. The extent of the background in this PIXE spectrum clearly illustrates the use of the proton beam in the measurement. The characteristic X-ray signals from these elements are fitted using GUPIX as described in Chapter 4. The fitted principle peak areas are converted to individual concentrations, resulting in the quantitative values shown in Table 6.3. The uncertainties on the concentrations are obtained by propagating the fit and statistical uncertainty from GUPIX. Note that the PIXE spectrum also exhibits a signal from Cl, which is also present in the RBS spectrum. The large background on which it is superimposed proves to be difficult for quantification, which is why the RBS data is used for the quantification of this element.

The concentrations from Table 6.3 clearly manifest how the simulation of the RBS spectrum underestimates the Ge signal compared to the As signal. The RBS Ge signal, from backscattered He ions on Ge atoms, should be stronger than the Se signal.

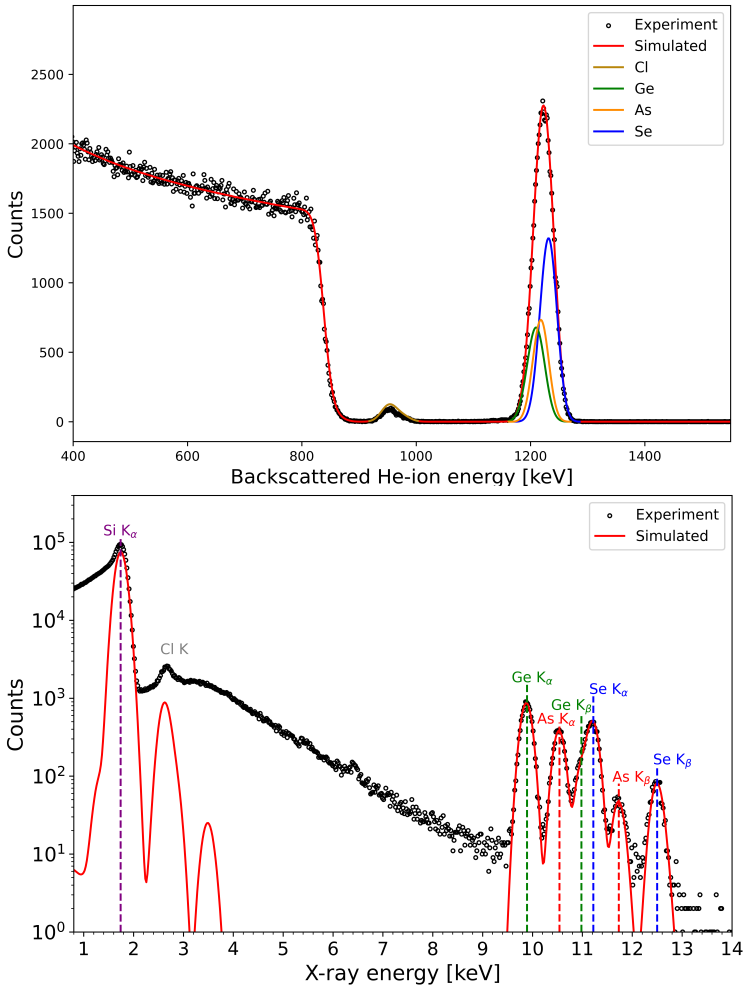

Figure 6.2: Top: RBS measuerment of the GeAsSe sample. Bottom: Conventional PIXE measurement of the same sample.

Ge concentration [%]	As concentration [%]	Se concentration [%]
35.33 ± 1.62	20.35 ± 1.62	44.32 ± 1.62

Table 6.3: Individual Ge, As and Se concentrations in the investigated GeAsSe sample obtained from the conventional PIXE measurement.

The bremsstrahlung background of the conventional PIXE measurement prevents the characterization of the lighter elements. To complement the RBS and PIXE analysis, an ERD experiment is performed with a 11 MeV Br^{+5}-beam to eject the oxygen, carbon and hydrogen nuclei from the sample. The use of a Br beam is motivated by the fact that it is a heavier element than Ge, As and Se which makes it kinematically possible to eject them from the target together with the lighter elements. Measuring the energy of each of the ejected nuclei together with the time that they needed to travel a fixed distance, results in the ERD spectrum shown in Figure 6.3. The definition of classical kinetic energy dictates that nuclei with different mass will define different curves in this 2D parameter space. Thus, measuring the additional time parameter allows ERD to distinguish individual elemental contributions, as clearly illustrated in Figure 6.3.

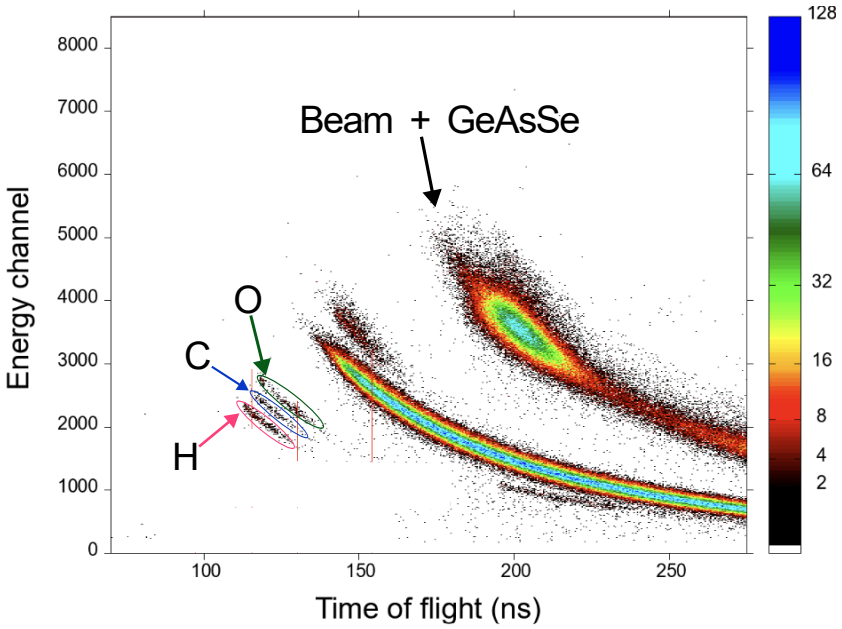

Figure 6.3: ERD measurement of the GeAsSe sample. The horizontal axis is the time that each ejected ion needed to travel a fixed distance and the vertical axis is the measured energy that was matched to each time measurement. (Spectrum recorded by K. Kantre)

Apart from the overlap of the Ge, As, Se and Br signals, one can also observe the concentrated signals from O, C and H. The amount of counts in the signals of O, C and H can be converted into elemental concentrations or areal densities. Data analysis software does this by interpreting the counts, corresponding to an element, with different energies as coming from different depths inside the sample.

Combining the total areal density of Ge+As+Se from the RBS analysis and the elemental concentrations obtained with the conventional PIXE setup from Chapter 3, allows the total areal density of Ge+As+Se to be converted into individual elemental areal densities. The concentrations for the light elements are then obtained from ERD. Combining the resulting elemental areal densities in a simulated fit to the RBS data results in the spectrum shown in Figure 6.4. The figure shows that the individual contributions of the Ge, As and Se signals are now correctly modeled. The simulated Ge signal is more intense than the As signal which is expected from the PIXE concentrations of Table 6.3.

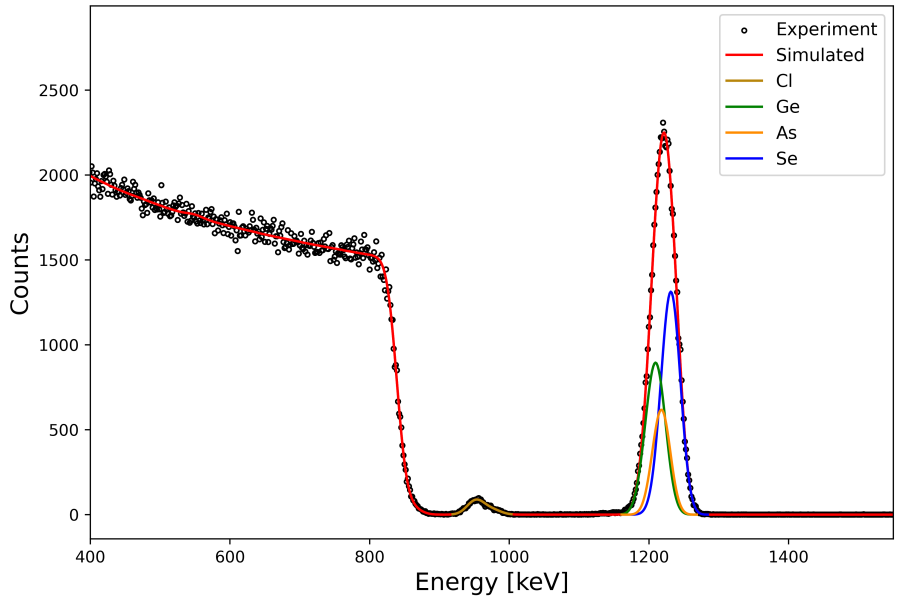

Figure 6.4: Improved fit to the RBS data where the PIXE concentrations of GeAsSe and the ERD concentrations H,C and O were input parameters. (RBS spectrum recorded by M. Bejide)

In addition to providing an important application for the conventional PIXE setup from Chapter 3, this self-consistent analysis also illustrates how powerful substrateless PIXE could be. Without the background from the substrate it would be possible to determine the concentrations of Cl, oxygen and other light elements. Thus, substrateless PIXE could not only serve as a verification method for the ERD results but also provide information for which one would normally need the combination of three different IBA methods.

Chapter 7

Demonstration of PIXE with self-supporting thin films

Combining the insights acquired from the investigation of the PIXE learning setup of the previous chapters allows the development of a new demo setup that can explore the capabilities of PIXE with self-supporting thin films or substrateless PIXE. This final chapter begins with discussing the process that is needed to guide the beam towards the new setup. Next, the fabrication process of a substrateless sample is introduced. With the substrateless sample, the necessary adjustments to the newly developed setup are introduced together with the setup layout. Lastly, the first experimental results of this demo setup are analyzed and interpreted, resulting in improvements in the current defined limit of detection.

7.1 Accessing the ion beam

The demo setup is constructed at the end of an existing beamline which is equipped with the beam steering mechanism that is shown in Figure 7.1. The accelerated MeV ion beam has to be steered towards the correct beamline in order to reach the experimental setup. This is done using a beamline selection magnet which creates a magnetic field that causes the ion beam to bend towards the PIXE beamline. The magnitude of the magnetic field can be tuned by changing the current that is used to generate the magnetic field by means of a coil. The challenge for the steering mechanism shown in Figure 7.1 is to guide the beam through the slits at the entrance of the PIXE beamline. The performance of the beam treatment can be monitored using the Faraday cup [74] which is positioned right after the entrance slit. It consists of a cylindrical cup which has a circular diaphragm attached to the entrance part. The beam particles would be stopped inside the Faraday cup (FC) and induce a current which is proportional to the beam intensity. Applying

a negative voltage to the diaphragm at the entrance increases the accuracy of the beam charge measurement because it reduces the probability that secondary electrons could escape the cup. Note that this is a destructive method of measuring the beam charge so it is not possible to do an experiment in the setup when the FC is inserted in the beamline. This is handled by a system that can retract the cup.

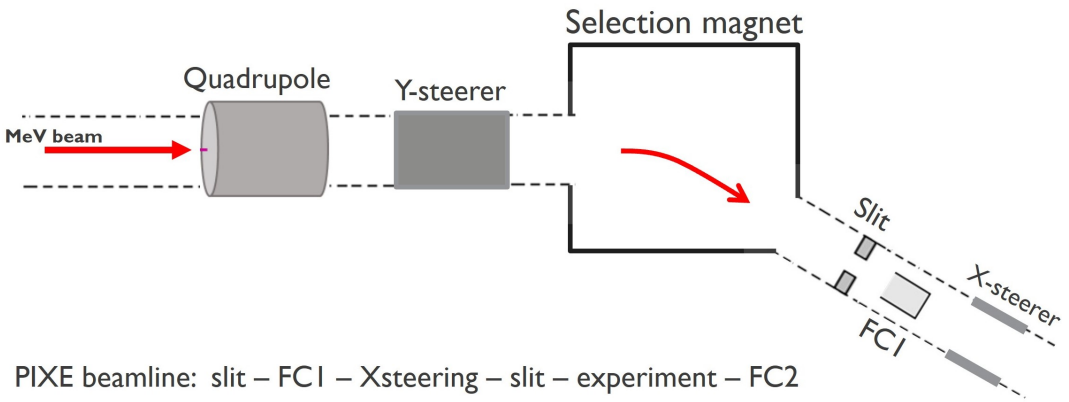

Figure 7.1: Layout of the beam steering part of the beamline.

The first step is thus to optimize the FC current signal by varying the current of the selection magnet. The centralized position of the cup also allows the experimentalist to optimize the vertical position of the beam with respect to the edge of the beamline. This can be done using the electrostatic Y-steerer positioned before the magnet. Once a signal is obtained in the cup, the measured current can be optimized by varying the voltage difference across the Y-steerer and the magnetic field of the quadrupole magnet which is used to focus the beam.

With the optimized beam in the entrance of the PIXE beamline, the cup is retracted after which the X-steerer is used to guide the beam through a beam profile monitor. The beam profile monitor is a complex device which uses a rotating wire to indicate how focused the beam is. This final X-steerer is very important in the process of guiding the beam towards the experimental setup. A well aligned experimental setup would not need any correction in the x-direction.

7.2 Experimental setup

7.2.1 Substrateless sample

The innovative approach of substrateless PIXE is that a large part of the Si substrate is removed. This is done by using a method called selective wet etching [75], which results in the substrateless or self-supporting thin film that is shown on the right hand side of Figure 7.2.

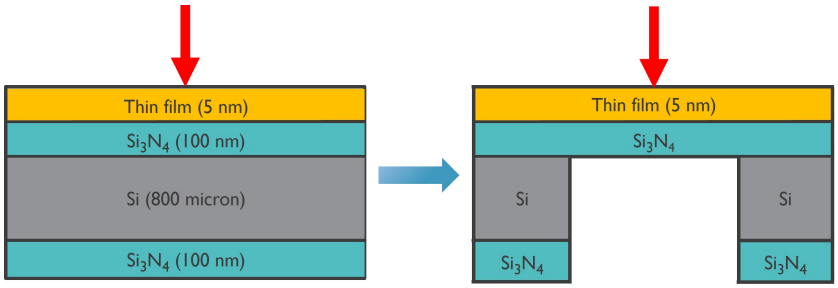

Figure 7.2: On the left side: The thin film on a Si substrate. On the right side: The obtained self-supporting thin film which rests on top of a pellicle.

The resulting central part of the sample is also called the pellicle. The process that is used to fabricate this pellicle is shown in Figure 7.3. Here, one starts with a Si substrate that has an additional layer of Si_3N_4 on the top and bottom surfaces. First, a part of the bottom Si_3N_4 layer is etched away by using a photoresist screen that is partly exposed to light. This selectively removed part of the photoresist enables the dry etching processes to create a well-defined cavity in the Si_3N_4 layer.

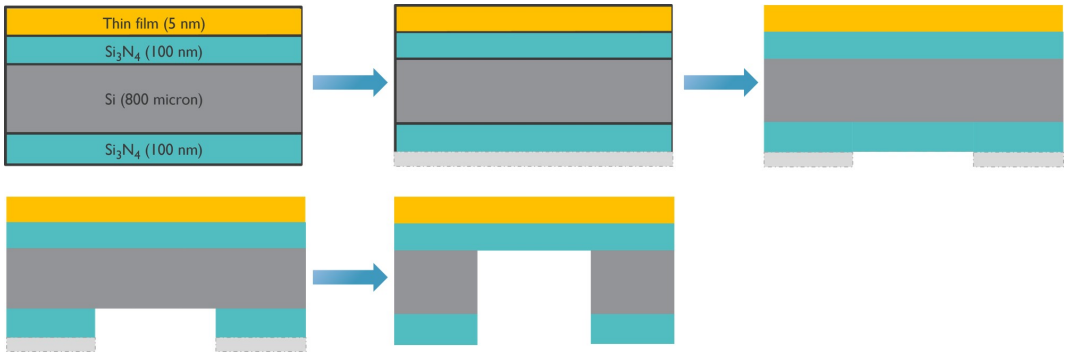

Figure 7.3: Fabrication process of the pellicle on which the thin film supports.

The next step in the process is to extend this cavity into the Si substrate. For this step, selective wet etching with KOH is used as an anisotropic wet etch technique. Anisotropic wet etching means that the chemicals will interact with the material

in a preferred direction. In our case, hydroxides are very efficient in breaking the Si bonds in the substrate, which will be the most efficient in the ⟨100⟩-direction of the silicon crystal [75]. The high etching rates of the {100} planes is due to the diamond like crystal structure of Si, which is shown Figure 7.4. Here, the (100), (110) and (111) planes are also shown, which illustrates how the (100)-planes in the Si crystal are less densely packed compared to the (111)-planes. This difference in packing explains the anisotropic behavior of the KOH wet etch process. Having a mono-crystal silicon substrate that is oriented along the ⟨100⟩-direction will thus allow the cavity to be extended towards the final Si_3N_4 layer.

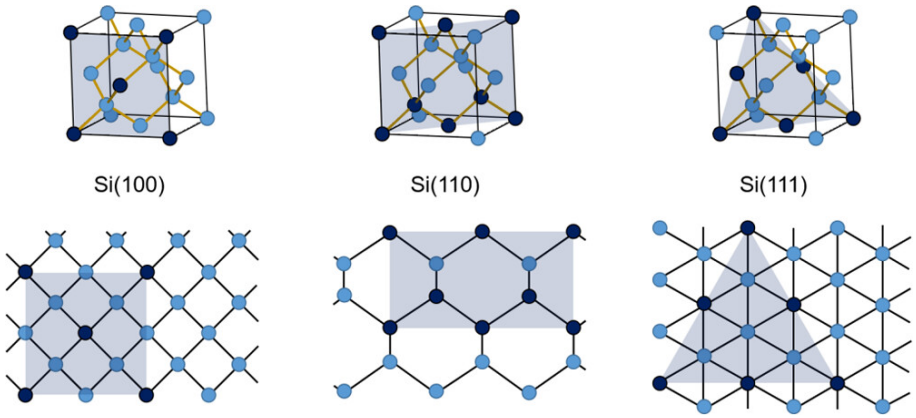

Figure 7.4: Crystallographic structure of a silcone crystal. Taken from [75].

The process will not have an effect on this Si_3N_4 layer due to the different bonds that are present in the material, creating a mask to protect the IGZO thin layer at the top. In the end, one obtains a self-supporting sample that can be used to analyze the thin film in transmission mode. This means that the ion will be able to traverse through the sample, after which it has to be collected in a proper way without the creation of any additional X-rays. For this reason, we developed a new demo setup to perform PIXE with self-supporting thin films.

7.2.2 Setup layout

After having fabricated the pellicles using the process that was described in the previous part, one needs an experimental setup to perform a PIXE measurement. The setup that was introduced in Chapter 3, is only optimized for PIXE measurements of a thin film that is mounted on a Si substrate. When the substrate is removed the beam will be able to penetrate through the sample and cause Fe, Cr and Ni X-ray excitation in the back of the experimental chamber. The sample holder with which the setup is equipped is also not optimized for substratless PIXE because the beam would be stopped in the sample holder which would act

as an artificial substrate. Additionally, the slit setup has been proven to cause background X-ray signals from the sample holder due to small angle scattering. Taking all of these factors into account, the self-supporting or substratless PIXE setup that is constructed during this work is shown In Figure 7.5.

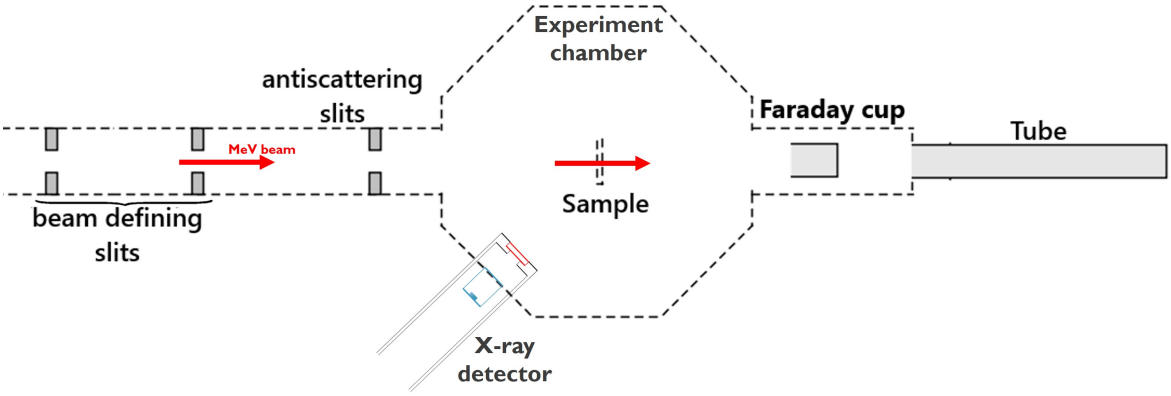

Figure 7.5: Layout of the substrateless PIXE demo setup.

The first thing that can be noticed about the layout from Figure 7.5 is the combination of three beam defining slits. In this layout, only the first two are used to define the extent of the ion beam, while the third slits are optimized such that only the small angle scattered beam particles are stopped. However, one of the two beam-defining slits eventually needed to be removed because it was not centralized inside the beamline and the fact that there was no additional Faraday cup in-between the second and third slits made the beam guiding complicated. The first slit on the left is the PIXE beamline entrance slit that was also shown in Figure 7.1. This figure already indicated the dual slit configuration that was used in the end. Note that Figure 7.5 does not consider the X-steerer which is stationed after the entrance slit. The Faraday cup at the end of the experimental chamber allows for a measurement of the beam current which is representative for the experiment in the case of a stable beam. Lastly, there is a long tube that is connected at the end of the setup which is used to collect the ion beam. The dimensions of this tube will make it very hard for any beam particles to backscatter towards the experiment chamber.

Using the dual slit setup, the beam was guided through the second slit and detected in the final Faraday cup at the end of the chamber. The end of the beam collection tube had a window with a fluorescence sample attached to it. This allows one to see the fluorescence light when the beam interacts with the sample, creating a light spot of the extent of the beam. The ion beam travels from the entrance of the PIXE beamline through meters of beamline all the way to the end

of the small tube at the end of the chamber, which would be impossible with a misaligned setup. Here, the newly constructed setup is first aligned using a laser that enters from a window on the backside of the selection magnet from Figure 7.1. After aligning the horizontal and vertical positions of the different parts of the beamline, the laser spot was visible on the window at the end of the tube from Figure 7.5.

Having aligned the beamline and optimized the beam in the final FC, the next step is to transfer the substrateless sample into the experiment chamber. The sample is mounted onto a sample holder as shown on the left part of Figure 7.6. It is important to note that the sample holder is rotated such that sample is on the backside which is facing towards the end of the chamber.

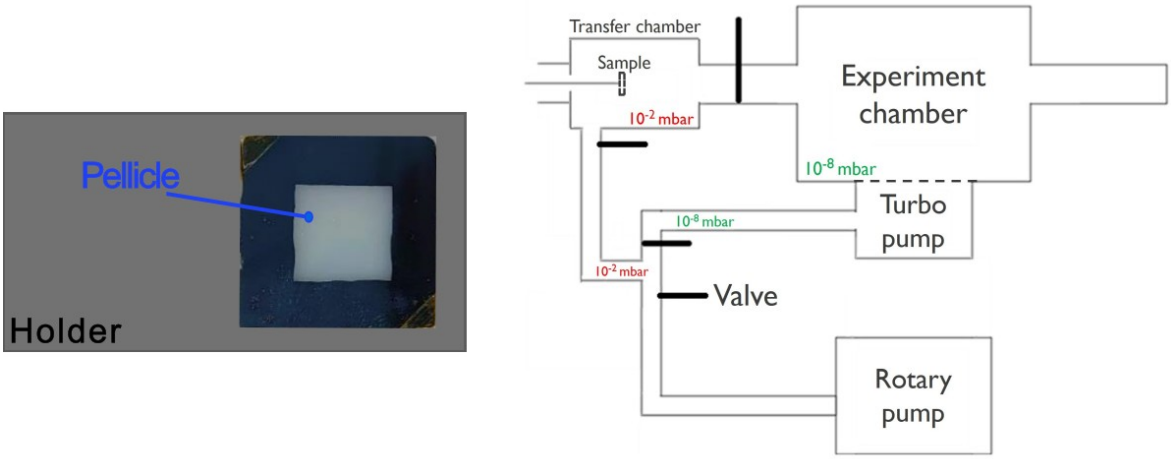

Figure 7.6: Left: Substrateless sample mounted on backside of sample holder. Right: Sample transferring and vacuum system.

The reason for this decision is as follows, the transparent pellicle part of the sample is extremely fragile which means that it is not possible to safely install a shielding plastic over the edges. This plastic shielding is crucial to reduce the possible background contribution from small angle scattering at the slits, as was shown in Chapter 5. Additionally, it would be very hard to determine whether the measured PIXE spectrum is the result of the beam impinging on the substrate part on the edges of the sample or the substrateless part at the center. Attaching the sample on the backside of the sample holder allows one to create a hole in the holder such that the beam can pass through and impinge only the central substrateless part of the sample. The plastic shielding covers the frontside of the holder such that no additional X-rays from the sample are created which allows the experimentalist to verify the position of the beam on the pellicle by measuring the thin film X-rays.

The sample is transferred inside the experiment chamber using the mechanism that is shown on the right part of Figure 7.6.

Important to keep in mind during the transfer process, is that one has to consider the pumping system that was constructed with the demo setup, which is also shown on the right of Figure 7.6. Two pumps are used to create a vacuum with a pressure of 10^{-8} mbar inside the experiment chamber. The rotary pump is capable of providing a minimal pressure of 10^{-2} mbar [74] inside the experiment chamber, after which the turbo-molecular pump [74] is turned on to decrease the pressure further to the desired value. The valves that connect the transfer chamber to the experiment chamber and the rotary pump are closed during this process. Then, the sample holder is brought into the transfer chamber and closed off from the outside room pressure. Next, the valve connecting the experiment chamber to the rotary pump is closed and the rotary pump is exposed to the pressure in the transfer chamber as shown on the right in Figure 7.6. The obtained pressure of 10^{-2} mbar in the small transfer chamber allows one to open the valve to the experiment chamber without significantly reducing the pressure there. This sample transfer system allow the experimentalist to transfer the sample inside and outside the experiment chamber without breaking the vacuum.

Finally, the demo setup from Figure 7.5 is ready to push the current state of the art of PIXE and investigate the potential of substrateless PIXE. As an additional safety measure, the HPGe detector is installed at the very end of the preparation process such that the connection port can be used to make sure that the alignment laser, which represents the beam, is visible on the sample in the experiment chamber.

7.3 Experimental results

7.3.1 Substrateless IGZO

With the substrateless IGZO sample installed in the center of the experimental chamber from Figure 7.5, the first experiments could be performed. Initially, two measurements are made using a 2.3 MeV He-ion beam which induced a current of 20 nA in the final Faraday cup. This Faraday cup was retracted during the measurements to prevent any beam particles from backscattering towards the sample. One of the PIXE measurements is performed on a conventional IGZO thin film with a Si substrate, while the other uses the substrateless sample on the left of the figure 7.6. The obtained PIXE spectra from both of these measurements are shown in Figure 7.7.

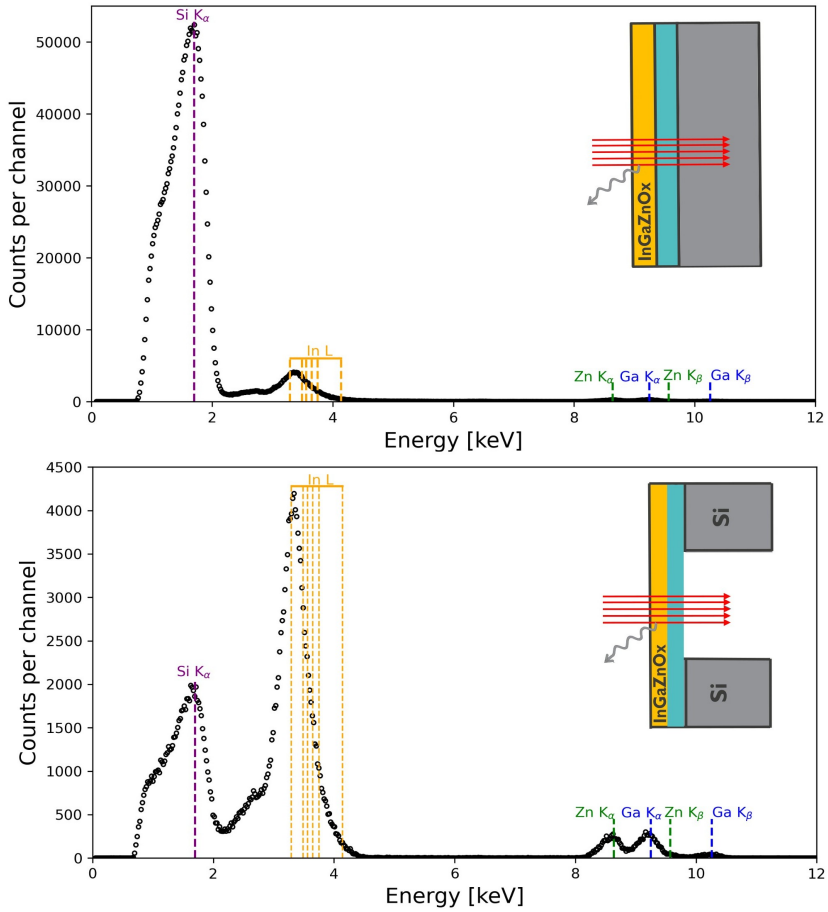

Figure 7.7: Top: Conventional PIXE measurement of a IGZO thin film sample. Bottom: Substrateless PIXE measurement of IGZO thin film on a pellicle.

The top part of the figure is the measurement in the manner of conventional PIXE, which shows the intense signal from the substrate, and the bottom part is the substrateless PIXE measurement. Both spectra are shown with the X-ray counts on linear scale to indicate the large intensity difference between signals of the Si X-ray and the X-rays that originate from the elements inside the IGZO thin film. In the case of the substratless PIXE result, one can clearly observe that the intensity of the Si X-ray has decreased with a factor of 25, together with the bremsstrahlung intensity compared to the conventional PIXE measurment. The L-lines from indium are now the dominant contribution in the spectrum and the remaining Si signal is the result of the 120 nm Si_3N_4 layer on which the IGZO thin film supports.

The intense L-line signal can be understood from the large X-ray production cross sections of L-shell X-rays. However, the oxygen K_α X-ray which should result from the oxygen in the IGZO sample is not visible yet in the bottom spectrum of Figure 7.7. This might seem problematic at first sight but can be explained by the 52 μm Mylar absorber that is still positioned in front of the detector. One of the original functions of this absorber in the sense of conventional PIXE was to attenuate the intense Si K_α and low energy bremsstrahlung background that originated from the Si substrate. Without this absorber, the detector would oversaturate, negatively impacting the measurement of the IGZO signals. The large absorber attenuation coefficient for the low energy X-rays is expected to prevent the 520 eV oxygen K_α X-rays from reaching the HPGe detector.

The substratless measurement seems to indicate that the thickness of the absorber can be reduced and the high energy loss of the potentially backscattered He-ions also allows a thinner absorber to be used. To investigate this, additional measurements are performed with a Mylar absorber of 26 μm. The results of these measurements are shown in Figure 7.8. Here, the conventional PIXE measurement is again compared to the substrateless PIXE result. Interesting to observe is the conventional PIXE measurement which is influenced by a detector dead time of 20 %. The low energy background from the substrate has increased significantly in intensity as one would expect. This can also be concluded in the substrateless case where the Si signal is now of comparable magnitude as the L-line signal from indium. The main conclusion from Figure 7.8 is the fact that the true intensity of the Si substrate has been underestimated. Reducing the substrate of 1 mm to a SIN pellicle of 120 nm, does decrease the intensity of the Si substrate signal by almost two orders of magnitude but the initial signal was already heavily attenuated by the 26 μm Mylar absorber. The remaining intensity of the Si signal can be explained by two limiting factors. First, the Si_3N_4 pellicle still has a thickness of

120 nm compared to the 10 nm of the IGZO thin film so it should be expected that the Si X-ray signal is more intense than the IGZO X-ray signals. Intuitively, one may expect the large substrate reduction to impact the intensity of the background more significantly but the strong beam energy dependence of the X-ray production cross section prevents this. The fact that the cross section decreases for the lower beam energies implies that a significant part of the Si K_α contribution is induced in the first small part of the original Si substrate. Reducing the substrate thickness will thus only eliminate the Si X-rays which intrinsically already had a lower production cross section. In some sense, the large X-ray production cross section for the light elements which has the potential to make PIXE sensitive to light elements, is the very thing that in the end also limits the reduction of the substrate background.

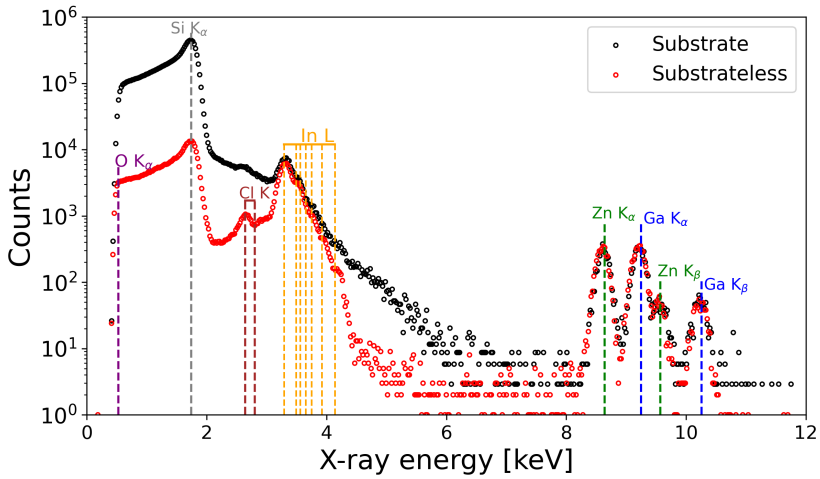

Figure 7.8: Comparison of conventional and substrateless PIXE measurement of an IGZO thin film. The Myler absorber thickness was reduced to 26 μm.

There is however more to learn from the substrateless result of Figure 7.8. The bremsstrahlung background has significantly been reduced between 2 keV and 8 keV which allows one to observe all the features of the indium L-line signals. This decrease is expected to make substrateless PIXE more sensitive to the elements heavier than Si, which can already be seen from the chlorine signal. On the other hand, one can observe a background between 2 keV and 4 keV which seems to have a different X-ray energy dependence than the original bremsstrahlung background. More measurements have to be performed to deduce the origin of the background. Additionally, the low energy background below 1.74 keV seems to have scaled down with the same magnitude as the Si K_α X-rays. This background was previously denoted to low energy bremsstrahlung processes but it still seems to prevent the measurement of the oxygen signal. Lastly, the strong cut off below an X-ray energy

of 500 eV, expected to be the result of the low energy absorption edges of H and C in the Mylar absorber, was still present in a final substrateless IGZO measurement without the Mylar absorber. One can thus conclude that the cutt off is the result of a lower energy limit that is set by the electronics of the detector. The X-rays of these low energies correspond to voltage pulse signals with such a low amplitude that they are filtered out with the detector noise.

7.3.2 Substrateless STO

The previous section revealed that the substratless PIXE results indicate a larger sensitivity to the elements heavier than silicon, compared to what could be achieved with conventional PIXE. To investigate this further, measurements were performed on a SrTiO (STO) substrateless sample. This sample had the same build as the substratless IGZO sample. Similar to the measurements from Figure 7.8, the Myler thickness of 26 μm was used. The results of the measurements are shown in Figure 7.9. At first sight, the results of Figure 7.9 seem to lead to the same conclusions as the results from Figure 7.9. However, upon further investigation one can observe some differences. First of all, the conventional PIXE measurement has an unusual bremsstrahlung background shape between 2 keV and 8 keV and additional noise is also present for the higher X-ray energies, especially around the K-line signals from Sr. This is an appropriate example of what the effect of a large detector dead time can be on the measured spectrum. The dead time in this case was 30 % compared to the 1 % dead time of substrateless PIXE measurement which is also shown in Figure 7.9.

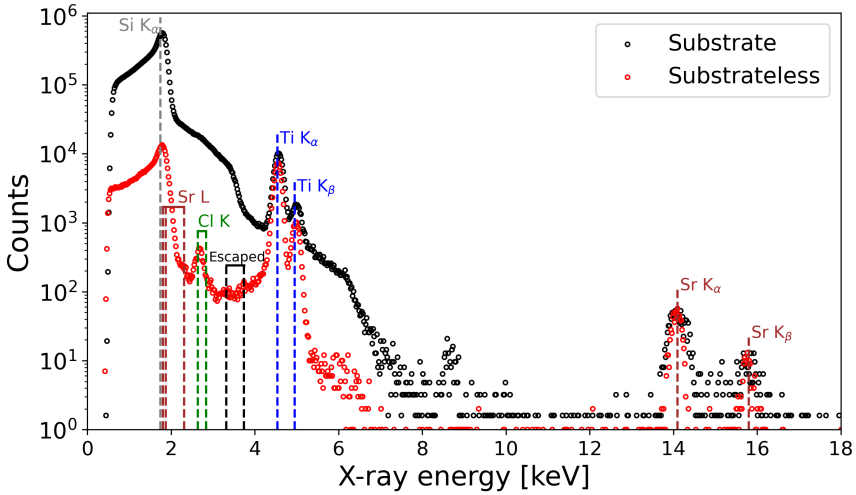

Figure 7.9: Comparison of conventional and substrateless PIXE measurement of an STO thin film. The Myler absorber thickness was 26 μm.

Secondly, the background between the Si K-line and the In L-lines in Figure 7.8, seems to be more intense than the substrateless result from Figure 7.9. This comparison can be made with respect to the Si K-line intensity which is similar for both of the substrateless measurements in both figures. This difference suggests that the background could be unrelated to the 120 nm Si_3N_4 pellicle. Regardless, the substrateless measurement from Figure 7.9 allows one to see the total features of the Ti K-lines due to the reduced bremsstrahlung background. Next to the Ti K-lines, there are two small signals which are the result of Ti K_α and K_β radiation which did not fully deposit their energy in the HPGe detector. Instead, one of the characteristic L_α X-rays which were induced in the energy deposition process escaped the active area of the detector. This conclusion is made due to the energy at which these escape peaks appear in the spectrum. They each have an energy that is 1.20 keV lower than their respective Ti K_α and K_β mother signals, which is the energy of the Ge L_α X-ray.

The increased sensitivity of substratless PIXE to the elements heavier than silicon is clearly visible in the Cl signal that is manifested in the spectrum of Figure 7.9. This signal was not visible in the conventional PIXE measurement and could be an artifact from the deposition process of the thin film. The statement about the increased sensitivity of substateless PIXE, can be further supported by comparing the measurement with the result of an RBS experiment that was obtained with another setup. The RBS measurement of the same substrateless STO sample is shown in Figure 7.10 and consists of the signals from the Ti and Sr inside the STO layer.

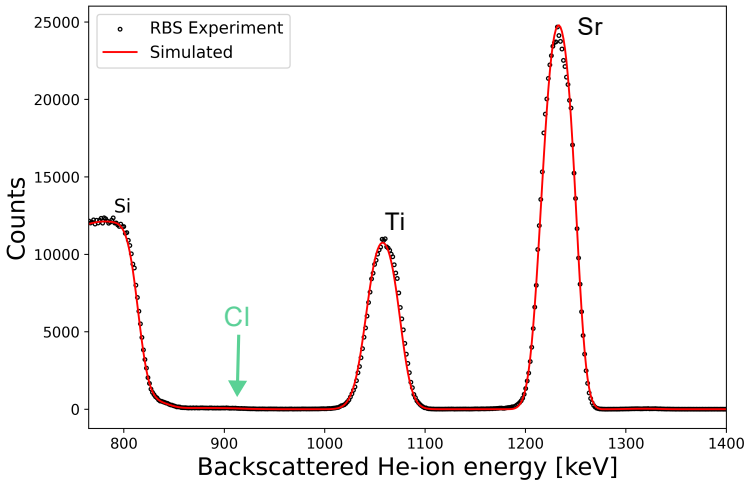

Figure 7.10: RBS measurement of the substrateless STO sample, obtained using a different setup that was optimized for RBS experiments.

Here, the Cl signal is not significant enough for the quantization of the amount of Cl in the sample. This implies that RBS is not sensitive enough to detect the low amount of Cl which is present inside the STO sample, but substratless PIXE is.

7.3.3 Improved limit of detection

In order to quantify the sensitivity improvements of substrateless PIXE, one can determine the limit of detection of the measured thin film signals. The new LOD values from the substrateless PIXE measurements are shown in Figure 7.11, together with the RBS LOD and conventional PIXE LOD values from the literature [76]. The red curve is obtained using the GUPIX procedure of obtaining LOD values for elements which are not present inside a spectrum, which was described in Chapter 4. The LOD values for chlorine and Ti have vastly improved. One can expect similar improvement for the other elements between $Z = 16$ and $Z = 28$, which have K-lines that are normally imposed on the bremsstrahlung background from conventional PIXE. The increase in LOD is now determined by the X-ray production cross section and no longer by the background.

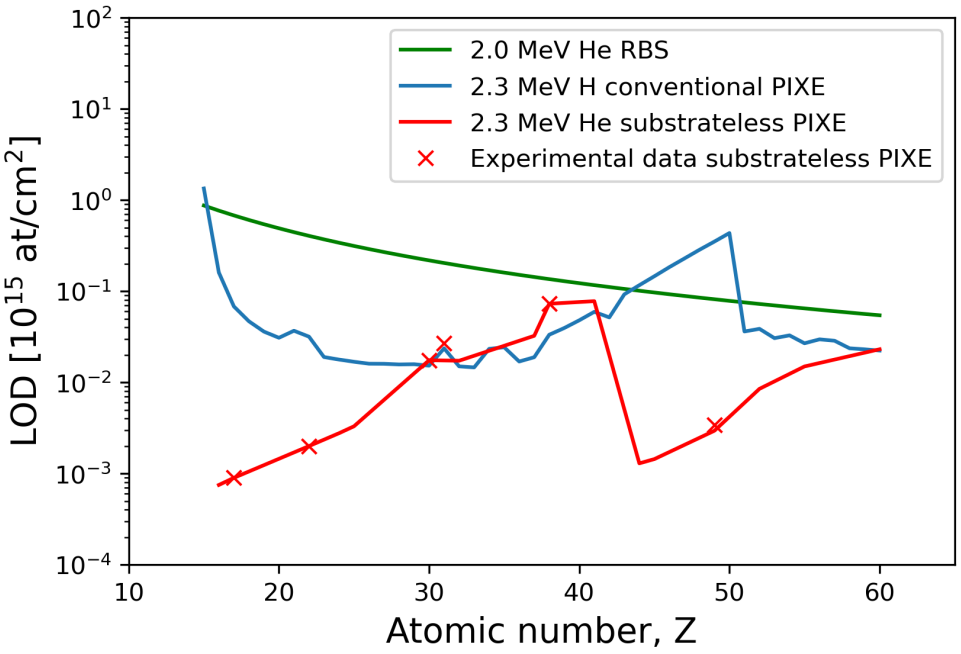

Figure 7.11: Comparison of the obtained limit of detection obtained with the demo setup and literature values [76] for conventional PIXE and RBS.

For Zn and Ga we see a similar LOD compared to conventional PIXE which is due to the fact that the intensity of the background at the energy of these characteristic

X-rays was already very low. Investigating substrateless PIXE with a proton beam in future research can be interesting because one would expect a stronger effect for Ga and Zn compared to the He-ion beam case. This can be understood from the fact that the background for PIXE with protons continues to slightly higher energies and because the X-ray production cross section with a proton beam would be larger. For Sr, we see that He-ion substrateless PIXE actually does less well than conventional PIXE with a proton beam, which can be fully explained by the lower ionization cross section of He relative to protons that was also mentioned in Chapter 5. The advantage of substrateless PIXE is no longer valid for these atomic number ranges because the background intensity was already very low at these X-ray energies. For Indium one also observes a large improvement and similar improvements are expected for the elements between $Z = 41$ and $Z = 50$. This is motivated by the fact that the L-lines of these heavy elements were also imposed on the bremsstrahlung background from conventional PIXE.

7.3.4 Low energy background

The substrateless PIXE results that have been discussed in this section seem to indicate that the low-energy tail below the Si X-ray is a definitive limitation for the detection of oxygen X-rays. However, a further investigation of the substrateless PIXE measurements results in the comparison that is shown in Figure 7.12. The top part of the figure compares substrateless PIXE measurements that are obtained from the same IGZO sample but where a different Mylar absorber thickness was used. At first sight, it may seem that the measurement with a thicker absorber has the expected result. The bottom part of the figure shows the same measurement with a 52 μm Mylar absorber, but this spectrum is now compared to the 26 μm Mylar measurement that has been multiplied with the additional transmission that an extra 26 μm of Mylar would induce. This principle is based on

$$I(52\ \mu m)_{expected} = I_0 \cdot e^{\mu_{Mylar} \cdot 26} \cdot e^{\mu_{Mylar} \cdot 26} = I_0 \cdot e^{\mu_{Mylar} \cdot 52} = I(52\ \mu m)_{measured},$$

where μ_{Mylar} is the attenuation coefficient as a function of X-ray energy which is obtained from the XCOM database [47]. Important to note is that the low energy tail contribution from the 52 μm Mylar absorber measurement does not resemble the shape that is expected from theory. One can conclude the same thing for the background between 2 and 4 keV but the intensities of the X-ray signals that originate from the sample do scale with the expected factor. Thus, the comparison of the bottom part from Figure 7.12 leads to the conclusion that the low-energy tail is not the result of the physics of the ion beam interaction with the substrateless sample, but from the physics of the interaction of the Si X-ray in the detector medium which takes place after the Mylar absorber.

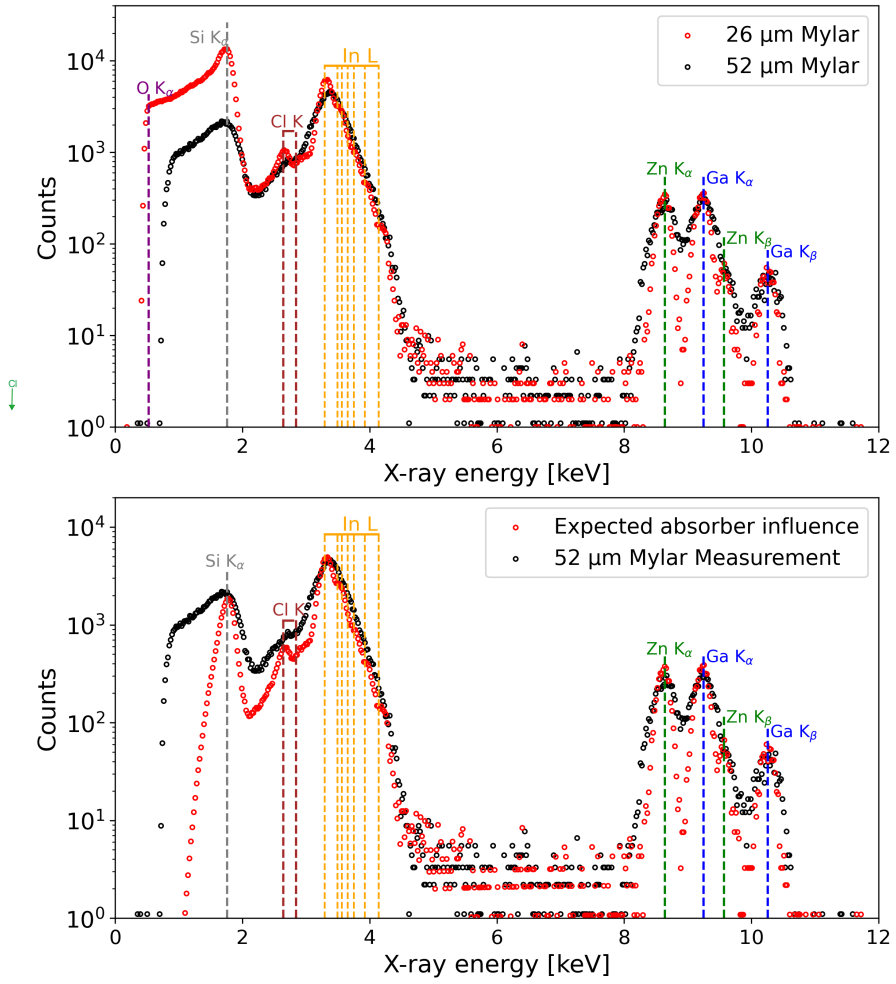

Figure 7.12: Top: comparison of substrateless IGZO measurements for two different Mylar absorber thickness values. Bottom: Comparison of theoretically expected spectrum with an increased absorber thickness, starting from the 26 μm measuerment, and the experimental obtained 52 μm Mylar spectrum.

The low-energy tail is a part of the Si X-ray lineshape and is attributed to a significant Ge dead layer at the detector surface. The reason behind the intensity of this low-energy tail feature can be understood from Figure 7.13. The Si X-ray with an energy of 1.74 keV will interact very close to the surface of the detector due to the fact that it has an energy which is just above the Ge L-line absorption edge of 1.22 KeV [19]. This can be understood from the discussion on absorption edges from Chapter 3. The large Ge attenuation coefficient will generally cause the X-rays to interact very close to the detector surface. Here, it produces a photoelectron as illustrated in Figure 7.13 which can be emitted in different directions. Ge

detectors that are not optimized for the detection of these low-energy X-rays will have a Ge dead layer with a significant thickness at the electrical contact. If the photoelectron or auger electrons can travel a distance in the detector which is similar to the range shown in Figure 7.13, then a part of their energy will not be deposited in the active Ge detector area which means that a part of the charge carriers that contribute to the voltage signal are lost. This process can induce an intense low energy tail below the characteristic X-ray signals with an energy below 3 keV and the intensity of this tail is expected to increase for the lower energies [48]. From Figure 7.13 one can also observe that the indium signal also seems to have a low-energy tail.

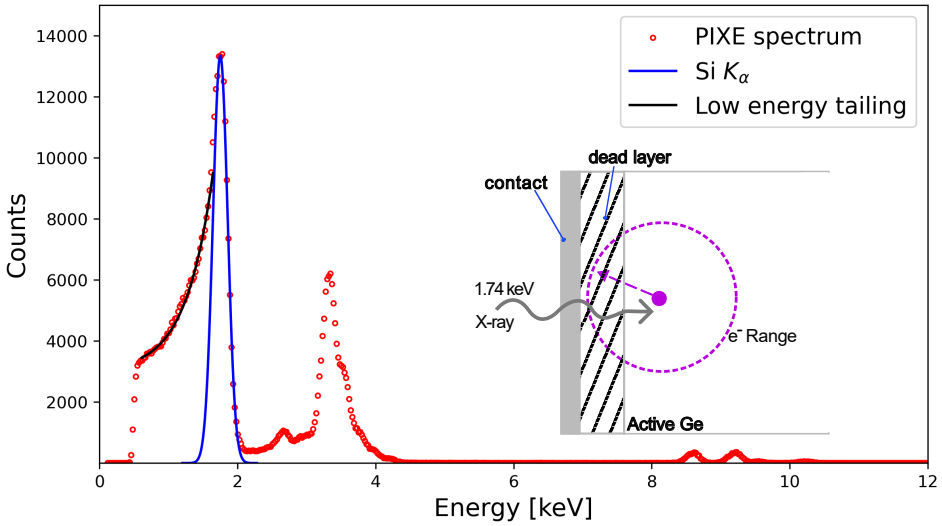

Figure 7.13: The result of a Gaussian fit to the Si K_α signal together with an exponential curve fit to the low energy tail.

The final insight that leads to the conclusion that the low-energy tail is a detector effect is the fact that the HPGe detector that has been used is not the GUL0055 [43] but the GL0055 [77] which is only optimized for the detection of X-ray with an energy larger than 3 keV. This is a well known problem in Ge detectors [78, 79, 80] but the literature [80] shows that the intensity of this tail can be reduced when the electrical contacts are implanted into the Ge crystal. This also explains the large calibration factor from Chapter 6 because the detector file that was used as an input for GUPIX, is the detector file for a GUL detector. The file contains a thin Ge dead layer, whereas the GL HPGe detector is expected to have a thicker dead layer which results in improper detection efficiency modeling. This limitation seems to be definitive for the substratless PIXE setup with the HPGe detector.

However, the SDD that was mentioned in Chapter 3 has an entrance window which is optimized for the measurement of X-rays with an energy below 1 keV. This would allow the 520 eV X-ray to be less intensely attenuated compared to the HPGe detector entrance window as shown in Figure 7.14. Additionally, the smaller attenuation coefficient that the low-energy X-rays feel in the Si crystal compared to the Ge crystal result in an attenuation length which is two orders of magnitude larger. This implies that the energy deposition process of a 520 eV X-ray can be less sensitive to detector surface effects of the SDD when compared to the HPGe detector. The small entrance window also suggests that the SDD is optimized for the measurement of these low energy X-ray.

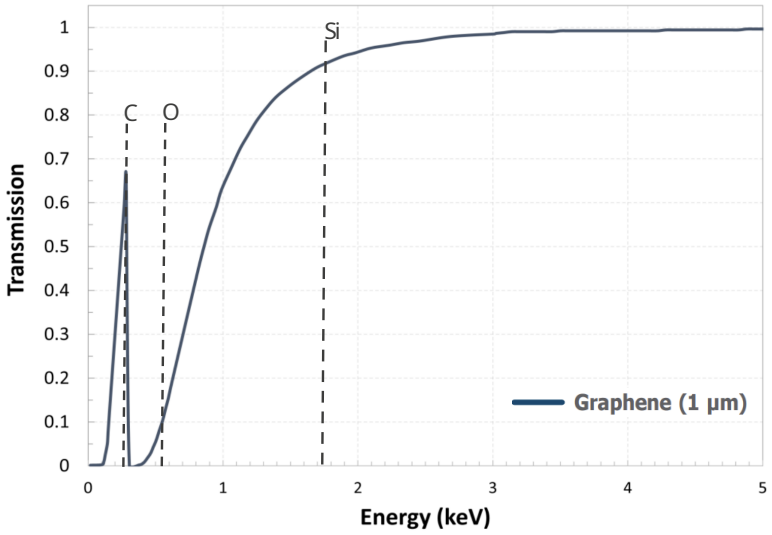

Figure 7.14: The tranmsission curve for the entrance window of the SDD from rayspec, optimized for measuring low energy X-rays. Data obtained from [44].

In future research, one can optimize the substratless PIXE setup and use both the SDD and the HPGe detector. This could allow for the measurement of the oxygen X-ray. If the low energy tail from the Si signal is less intense, then the oxygen signal could become visible. Another alternative is to reduce the pellicle thickness in order to suppress the Si X-ray contribution even further.

Conclusion

The aim of this master thesis was to investigate the performance of PIXE for the characterization of semiconducting thin films. For this purpose, the research began with the construction of the conventional PIXE setup described in Chapter 3. The initial performance experiments with this setup resulted in good agreement between the measurements and what is expected from the theory. The GUPIX analysis of two PIXE spectra that were measured from two samples that each contained different concentrations of Pt and W illustrated how the conventional PIXE setup can determine the difference in Pt and W concentration. Lastly, a detailed study of the observed signal and background intensities from PIXE measurements obtained with a proton and He-ion beam of the same energy was performed. This resulted in the conclusion that a 2 MeV He-ion beam is expected to become more efficient for the production of characteristic K-shell X-rays for elements that have an atomic number below $Z = 21$. The less intense bremsstrahlung background from the He-ion beam case became less important for the elements with larger atomic numbers due to the large proton beam ionization cross section for K-shell X-ray. Further research has to be conducted in order to determine the concrete atomic numbers of the elements for which the He-ion beam becomes more efficient to produce K-shell X-rays.

With an understanding of how the beam nature influences the observed signal and background intensities from conventional PIXE spectra, the experimental setup from Chapter 3 could be used to investigate the ability of conventional PIXE to characterize semiconducting thin films. This was discussed in Chapter 6, where the setup was first calibrated for the accurate determination of elemental concentrations from an IGZO thin film. The calibration was performed with a method from the literature that used three calibration samples. However, the obtained $h_{In/Zn}$ calibration factor suggested that a correction of ~ 40 % should be applied to the In concentrations of the IGZO samples that are obtained with the conventional PIXE setup. This could be due to large uncertainties in the theoretical X-ray production cross sections of L-lines or to improper detection efficiency modeling. Nevertheless, the $h_{Ga/Zn}$ calibration factor had a value close to unity. The Total-

IBA analysis illustrated the importance of conventional PIXE measurements for the characterization of GeAsSe thin films. This results in accurately modeled RBS data from the GeAsSe sample, shown in Figure 6.4.

The final goal of this work was to investigate the potential of substrateless PIXE to characterize light elements inside a thin film. Here, the demo setup described in Chapter 7 was constructed to perform substrateless PIXE measurements. The measurements of substrateless IGZO and STO thin films that were obtained with this setup resulted in an improved limit of detection for Cl, Ti and In. The oxygen signal was still not visible because of an intense low-energy tail below the Si X-ray. However, further investigation showed that this low-energy tail is the result of a detector effect inside the HPGe detector. The effect causing the intense low energy tail is illustrated in Figure 7.13 and is the result of the large attenuation coefficient of the Si X-ray in the Ge detector medium. However, the reduced background and improved limit of detection values indicate the potential of substrateless PIXE. The setup has to be optimized in future research, where an SDD with a thinner entrance window could be used to detect oxygen X-rays. The smaller attenuation coefficient that the low-energy X-rays experience in the Si detector has the potential to significantly decrease the intensity of the low-energy tail.

Acknowledgements

I would like to thank my Imec promotor, Johan Meersschaut, for his constructive guidance during this master thesis project. The ion beam analysis team led by him provided me with a productive and challenging learning space. Their feedback on my research progress during the regular scientific presentations helped me to think critically about my work. I would also specifically like to thank Karim Kantre, for the collaboration in the lab which provided me with the necessary tools to construct the new experimental setup. Whenever I needed an RBS measurement, I could always count on Matias Bejide to help me with the experiment, for which I am very grateful. Generally, I would like to thank the whole team for their support and kindness. Another important acknowledgment is given to Professor Tytgat, who gave me the opportunity to present my progress to the detector physics team at the VUB. Lastly, I like to thank Quan, Ruben, Max, Louis, Filip, Judith and Eline for the insightful conversations during the breaks.

Before ending this part, I would like to thank my parents and my girlfriend for their tremendous support during this thesis. As a final acknowledgment I would like to thank Mai-Lan, Yanna, Yoëlle and Patricio for the many necessary evenings together that helped me remember the importance of enjoying the moments that are given to us.

Bibliography

[1] G.e. moore, *Cramming More Components onto Integrated Circuits,* electronics, vol. 38, no. 8, 1965, pp. 1–14.

[2] Gordon E Moore et al. Progress in digital integrated electronics. In *Electron devices meeting*, volume 21, pages 11–13. Washington, DC, 1975.

[3] Thomas N Theis and H-S Philip Wong. The end of moore's law: A new beginning for information technology. *Computing in science & engineering*, 19(2):41–50, 2017.

[4] Yuan Taur, Douglas A Buchanan, Wei Chen, David J Frank, Khalid E Ismail, Shih-Hsien Lo, George A Sai-Halasz, Raman G Viswanathan, H-JC Wann, Shalom J Wind, et al. Cmos scaling into the nanometer regime. *Proceedings of the IEEE*, 85(4):486–504, 1997.

[5] David J Frank, Robert H Dennard, Edward Nowak, Paul M Solomon, Yuan Taur, and Hon-Sum Philip Wong. Device scaling limits of si mosfets and their application dependencies. *Proceedings of the IEEE*, 89(3):259–288, 2001.

[6] Wilfried Haensch, Edward J Nowak, Robert H Dennard, Paul M Solomon, Andres Bryant, Omer H Dokumaci, Arvind Kumar, Xinlin Wang, Jeffrey B Johnson, and Massimo V Fischetti. Silicon cmos devices beyond scaling. *IBM Journal of Research and Development*, 50(4.5):339–361, 2006.

[7] Thi Thu Thuy Nguyen, Olivier Renault, Bernard Aventurier, Guillaume Rodriguez, Jean Paul Barnes, and François Templier. Analysis of igzo thin-film transistors by xps and relation with electrical characteristics. *Journal of Display Technology*, 9(9):770–774, 2013.

[8] Kar G.S. Belmonte, A. Disrupting the dram roadmap with capacitor-less igzo-dram technology. *Nat Rev Electr Eng 2*, page 220–221, 2025.

[9] 황은석 . *InGaZnO based charge trap device for NAND flash memory application.* PhD thesis, 서울대학교 대학원 , 2018.

[10] Yao, p., wu, h., gao, b. et al. fully hardware-implemented memristor convolutional neural network. nature 577, 641–646 (2020). https://doi.org/10.1038/s41586-020-1942-4.

[11] Yukun Li, Haotian Wang, Mingyue Shao, Yuhao Wang, Sannian Song, Yuan Xue, and Zhitang Song. Modulation of gese and as 2 se 3 motifs to optimise geasse ots performance and its mechanism. *Journal of Materials Chemistry C*, 13(2):735–742, 2025.

[12] The promise of ots-only memories for next-gen compute. *EDN*, 2023.

[13] Sergiu Clima, Taras Ravsher, Daniele Garbin, Robin Degraeve, Andrea Fantini, Romain Delhougne, Gouri Sankar Kar, and Geoffrey Pourtois. Ovonic threshold switch chalcogenides: connecting the first-principles electronic structure to selector device parameters. *ACS Applied Electronic Materials*, 5(1):461–469, 2022.

[14] Taras Ravsher, Daniele Garbin, Andrea Fantini, Robin Degraeve, Sergiu Clima, Gabriele Luca Donadio, Shreya Kundu, Hubert Hody, Wouter Devulder, Jan Van Houdt, et al. Self-rectifying memory cell based on sigeasse ovonic threshold switch. *IEEE Transactions on Electron Devices*, 70(5):2276–2281, 2023.

[15] Thomas B Johansson, Roland Akselsson, and Sven AE Johansson. X-ray analysis: Elemental trace analysis at the 10- 12 g level. *Nuclear Instruments and Methods*, 84(1):141–143, 1970.

[16] F. Folkmann, C. Gaarde, T. Huus, and K. Kemp. Proton induced x-ray emission as a tool for trace element analysis. *Nuclear Instruments and Methods*, 116(3):487–499, 1974.

[17] Keizo Ishii. Pixe and its applications to elemental analysis. *Quantum Beam Science*, 3(2), 2019.

[18] H Haraguchi and K Inagaki. Analysis for environmental monitoring: Analysis of sediment, river water and seawater samples by icp-ms and icp-aes. *Bunseki*, 7:494, 1998.

[19] J.W. Mayer T.L. Alford, L.C. Feldman. Fundamentals of nanoscale film analysis: Fundamentals and techniques. Springer, US, 2007.

[20] Laricchiuta, g. innovation in ion beam analysis for nanoelectronic materials. iioimport 2019; phd thesis, ku leuven.

[21] Simone Giangrandi, Timo Sajavaara, Bert Brijs, Kai Arstila, André Vantomme, and Wilfried Vandervorst. Low-energy heavy-ion tof-erda setup for quantitative depth profiling of thin films. *Nuclear Instruments and Methods in Physics Research Section B: Beam Interactions with Materials and Atoms*, 266(24):5144–5150, 2008.

[22] H. Paul and J. Sacher. Fitted empirical reference cross sections for k-shell ionization by protons. *Atomic Data and Nuclear Data Tables*, 42(1):105–156, 1989.

[23] Javier Miranda and Gregory Lapicki. Experimental cross sections for l-shell x-ray production and ionization by protons. *Atomic Data and Nuclear Data Tables*, 100(3):651–780, 2014.

[24] John L Campbell Sven A. E Johansson and Klas G Malmqvist. *Particle-induced X-ray emission spectrometry (PIXE)*. Wiley, New York, 1995.

[25] Philip F Kane and Graydon B Larrabee. *Characterization of solid surfaces*. Springer Science & Business Media, 2013.

[26] A Kahoul, M Nekkab, and B Deghfel. Empirical k-shell ionization cross-sections of elements from 4be to 92u by proton impact. *Nuclear Instruments and Methods in Physics Research Section B: Beam Interactions with Materials and Atoms*, 266(23):4969–4975, 2008.

[27] A Abassi, K Akmoum, A Kahoul, S Daoudi, B Deghfel, Y Kasri, I Derradj, A Bendjedi, A Hamidani, K Meddouh, et al. Universal empirical fit to lα, lβ and lγ x-ray production cross section by protons impact within updated experimental data: Three dimensional (z-dependence), collective and individual formulae. *Radiation Physics and Chemistry*, 190:109823, 2022.

[28] RW Fink, RC Jopson, Hans Mark, and CD Swift. Atomic fluorescence yields. *Reviews of Modern Physics*, 38(3):513, 1966.

[29] Principles E.P. Bertin and 1975) P.83 Practice of X-Ray Spectrometric Analysis (Plenum Press, New York.

[30] WALTER BAMBYNEK, BERND CRASEMANN, R. W. FINK, H. U. FREUND, HANS MARK, C. D. SWIFT, R. E. PRICE, and P. VENUGOPALA RAO. X-ray fluorescence yields, auger, and coster-kronig transition probabilities. *Rev. Mod. Phys.*, 44:716–813, Oct 1972.

[31] J. H. Hubbell, P. N. Trehan, N. Singh, B. Chand, D. Mehta, M. L. Garg, R. R. Garg, S. Singh, and S. Puri. A review, bibliography, and tabulation

of k, l, and higher atomic shell x-ray fluorescence yields. *Journal of Physical and Chemical Reference Data*, 23(2):339–364, 1994.

[32] Eberhard Haug and NJ: World Scientific 2004. Werner Nakel. The Elementary Process of Bremsstrahlung / Eberhard Haug, Werner Nakel. 1st ed. River Edge.

[33] George B. Rybicki and Alan P. Lightman. *Radiative Processes in Astrophysics*. Wiley, New York, NY, 1985.

[34] K Ishii, S Morita, and H Tawara. Bremsstrahlung induced by proton and he 3-ion bombardments in the 1-4-mev/amu energy range. *Physical Review A*, 13(1):131, 1976.

[35] K Murozono, Keizo Ishii, H Yamazaki, S Matsuyama, and S Iwasaki. Pixe spectrum analysis taking into account bremsstrahlung spectra. *Nuclear Instruments and Methods in Physics Research Section B: Beam Interactions with Materials and Atoms*, 150(1-4):76–82, 1999.

[36] David D. Cohen, Eduard Stelcer, Rainer Siegele, Mihail Ionescu, and Michael Prior. Experimental bremsstrahlung yields for mev proton bombardment of beryllium and carbon. *Nuclear Instruments and Methods in Physics Research Section B: Beam Interactions with Materials and Atoms*, 266(8):1149–1153, 2008. Ion Beam Analysis.

[37] A Yamadera, K Ishii, K Sera, M Sebata, and S Morita. Quasifree-electron bremsstrahlung induced by the projectile field. *Physical Review A*, 23(1):24, 1981.

[38] Keizo Ishii and S Morita. Continuum x rays produced by light-ion—atom collisions. *Physical Review A*, 30(5):2278, 1984.

[39] Glenn F. Knoll. *Radiation Detection and Measurement*. John Wiley & Sons, Hoboken, NJ, 4th edition, 2010.

[40] Leonard I. Schiff. *Quantum Mechanics*. McGraw-Hill, New York, 3rd edition, 1968. Available online at `https://archive.org/details/ost-physics-schiff-quantummechanics`.

[41] Martyn T. Swinhoe William H. Geist, Peter A. Santi. *Nondestructive Assay of Nuclear Materials for Safeguards and Security*. Springer Cham, 2024.

[42] L Szentmiklósi, T Belgya, Zs Révay, and GL Molnár. Digital signal processing in prompt-gamma activation analysis. *Journal of Radioanalytical & Nuclear Chemistry*, 264(1), 2005.

[43] High purity germanium (HPGe) detectors CANBERRA industries. Available online at https://www.mirion.com/products/technologies/spectroscopy-scientific-analysis/gamma-spectroscopy/detectors/hpge-detectors-accessories/u-lege-ultra-low-energy-germanium-detectors.

[44] Silicon Drift Detectors RAYSPEC. Available online at https://rayspec.co.uk/x-ray-detectors/silicon-drift-detectors/silicon-drift-detectors-sdd-principle-operation/.

[45] P. Lechner, C. Fiorini, R. Hartmann, J. Kemmer, N. Krause, P. Leutenegger, A. Longoni, H. Soltau, D. Stötter, R. Stötter, L. Strüder, and U. Weber. Silicon drift detectors for high count rate x-ray spectroscopy at room temperature. *Nuclear Instruments and Methods in Physics Research Section A: Accelerators, Spectrometers, Detectors and Associated Equipment*, 458(1):281–287, 2001. Proc. 11th Inbt. Workshop on Room Temperature Semiconductor X- and Gamma-Ray Detectors and Associated Electronics.

[46] Masanori Kobayashi, Nobuyuki Hasebe, Takuji Hiramoto, Takashi Miyachi, Satoshi Murasawa, Hiroyuki Okada, Osamu Okudaira, Naoyuki Yamashita, Alexey A Berezhnoy, Eido Shibamura, et al. Germanium detector with stirling cryocooler for lunar gamma-ray spectroscopy. *Nuclear Instruments and Methods in Physics Research Section A: Accelerators, Spectrometers, Detectors and Associated Equipment*, 548(3):401–410, 2005.

[47] Martin J Berger, J H Hubbell, Stephen M Seltzer, J S Coursey, and D S Zucker. Xcom: Photon cross section database (version 1.2). 1999.

[48] J.L. Campbell, G. Cauchon, M.-C. Lépy, L. McDonald, J. Plagnard, P. Stemmler, W.J. Teesdale, and G. White. A quantitative explanation of low-energy tailing features of si(li) and ge x-ray detectors, using synchrotron radiation. *Nuclear Instruments and Methods in Physics Research Section A: Accelerators, Spectrometers, Detectors and Associated Equipment*, 418(2):394–404, 1998.

[49] SM Osadchii, AA Petukhov, and VB Dunin. Measurement of the energy resolution of silicon x-ray detectors using absorption edge spectra. *Measurement Techniques*, 62(5):465–469, 2019.

[50] N. Strokan, V. Ajdačić, and B. Lalović. Measurements of the fano factor in germanium. *Nuclear Instruments and Methods*, 94(1):147–149, 1971.

[51] WJ Teesdale, JA Maxwell, A Perujo, JL Campbell, L Van der Zwan, and TE Jackman. Limits of detection and quantitation in pixe analysis of thick

targets. *Nuclear Instruments and Methods in Physics Research Section B: Beam Interactions with Materials and Atoms*, 35(1):57–66, 1988.

[52] R. Heller, N. Klingner, N. Claessens, C. Merckling, J. Meersschaut. Differential evolution optimization of Rutherford backscattering spectra. J. Appl. Phys. 2022 132 October. https://doi.org/10.1063/5.0096497.

[53] JF Ziegler, JP Biersack, and Matthias Ziegler. SRIM, the stopping and range of ions in matter. SRIM Co., 2008.

[54] J.A. Maxwell, J.L. Campbell, and W.J. Teesdale. The guelph pixe software package. *Nuclear Instruments and Methods in Physics Research Section B: Beam Interactions with Materials and Atoms*, 43(2):218–230, 1989.

[55] J.A. Maxwell, W.J. Teesdale, and J.L. Campbell. The guelph pixe software package ii. *Nuclear Instruments and Methods in Physics Research Section B: Beam Interactions with Materials and Atoms*, 95(3):407–421, 1995.

[56] John L Campbell, Theodore L Hopman, John A Maxwell, and Zdenek Nejedly. The guelph pixe software package iii: Alternative proton database. *Nuclear Instruments and Methods in Physics Research Section B: Beam Interactions with Materials and Atoms*, 170(1):193–204, 2000.

[57] J.L. Campbell, N.I. Boyd, N. Grassi, P. Bonnick, and J.A. Maxwell. The guelph pixe software package iv. *Nuclear Instruments and Methods in Physics Research Section B: Beam Interactions with Materials and Atoms*, 268(20):3356–3363, 2010.

[58] J.L. Campbell, D.J.T. Cureatz, E.L. Flannigan, C.M. Heirwegh, J.A. Maxwell, J.L. Russell, and S.M. Taylor. The guelph pixe software package v. *Nuclear Instruments and Methods in Physics Research Section B: Beam Interactions with Materials and Atoms*, 499:77–88, 2021.

[59] Manfred Otto Krause and JH Oliver. Natural widths of atomic k and l levels, k α x-ray lines and several kll auger lines. *Journal of Physical and Chemical Reference Data*, 8(2):329–338, 1979.

[60] F.h. schamber, in: X-ray fluorescence of environmental samples, ed. t.g. dzubay (ann arbor science publ., michigan, 1977).

[61] Gerd I Johansson. Modifications of the hex program for fast automatic resolution of pixe-spectra. *X-Ray Spectrometry*, 11(4):194–200, 1982.

[62] D.D. Cohen and M. Harrigan. K- and l-shell ionization cross sections for protons and helium ions calculated in the ecpssr theory. *Atomic Data and Nuclear Data Tables*, 33(2):255–343, 1985.

[63] Yousef Y Saaty. *The Plane Wave Born Approximation for Determining Atomic K-Shell Ionization Cross-Sections by Positive Ion Impact*. PhD thesis, Graduate School, 1975.

[64] S. Ouziane, A. Amokrane, and M. Zilabdi. Experimental measurements of x-ray production cross-sections by protons of energies between 1 and 2.3 mev and comparison with theoretical predictions of pwba and ecpssr models. *Nuclear Instruments and Methods in Physics Research Section B: Beam Interactions with Materials and Atoms*, 161-163:141–144, 2000.

[65] Grzegorz Lapicki and William Losonsky. Coulomb deflection in ion-atom collisions. *Physical Review A*, 20(2):481, 1979.

[66] Werner Brandt and Grzegorz Lapicki. Energy-loss effect in inner-shell coulomb ionization by heavy charged particles. *Physical Review A*, 23(4):1717, 1981.

[67] Zhiqiang Liu and Sam J Cipolla. Isics: A program for calculating k-, l-and m-shell cross sections from ecpssr theory using a personal computer. *Computer Physics Communications*, 97(3):315–330, 1996.

[68] Matej Batič, Maria Grazia Pia, and Sam J. Cipolla. Isicsoo: A class for the calculation of ionization cross sections from ecpssr and pwba theory. *Computer Physics Communications*, 183(2):398–404, 2012.

[69] K Wittmaack and B Hietel. Optimisation of peak-to-background ratios in proton-induced x-ray analysis of material deposited on thin and thick backings. *Nuclear Instruments and Methods in Physics Research Section B: Beam Interactions with Materials and Atoms*, 161-163:814–818, 2000.

[70] M. Mayer. Simnra user's guide, version 7.03.

[71] Isao Harayama, Daichiro Sekiba, Qiang Zhao, Andre Vantomme, Wilfried Vandervorst, and Johan Meersschaut. Calibration of pixe yields using cu as a reference. *Nuclear Instruments and Methods in Physics Research Section B: Beam Interactions with Materials and Atoms*, 406:115–118, 2017.

[72] Carlos Pascual-Izarra, Miguel A Reis, and NP Barradas. Simultaneous pixe and rbs data analysis using bayesian inference with the datafurnace code. *Nuclear Instruments and Methods in Physics Research Section B: Beam Interactions with Materials and Atoms*, 249(1-2):780–783, 2006.

[73] Marcos V Moro, Radek Holeňák, L Zendejas Medina, Ulf Jansson, and Daniel Primetzhofer. Accurate high-resolution depth profiling of magnetron sputtered transition metal alloy films containing light species: A multi-method approach. *Thin Solid Films*, 686:137416, 2019.

[74] International Atomic Energy Agency. Instrumentation for PIXE and RBS, 2000. IAEA TECDOC 1190.

[75] Xiezheng Yu, Yinghua Ye, Peng Zhu, Lizhi Wu, Ruiqi Shen, and Chen-guang Zhu. Wet anisotropic etching characteristics of si {111} in koh-based solution. *ACS omega*, 2025.

[76] J Meersschaut, M Käyhkö, HP Lenka, T Witters, Qiang Zhao, André Vantomme, and Wilfried Vandervorst. Rbs and pixe analysis of chlorine contamination in ald-grown tin films on silicon. In *AIP Conference Proceedings*, volume 1525, pages 190–194. American Institute of Physics, 2013.

[77] Low energy Ge (LEGe) detector CANBERRA industries. Available online at `https://www.mirion.com/products/technologies/spectroscopy-scientific-analysis/gamma-spectroscopy/detectors/hpge-detectors-accessories/lege-low-energy-germanium-detector`.

[78] Johann Plagnard, Christophe Bobin, and Marie-Christine Lépy. Accurate efficiency calibration of a low-energy hpge detector using a monochromatic x-ray source. *X-Ray Spectrometry: An International Journal*, 36(3):191–198, 2007.

[79] Asad Shariff, Bengt G Martinsson, Vaida Auzelyte, Mikael Elfman, Per Kristiansson, Klas G Malmqvist, Christer Nilsson, Jan Pallon, and Marie Wegdén. Evaluation of low-energy tailing parameters of a hpge x-ray detector to be used in gupix software library for pixe analysis. *Nuclear Instruments and Methods in Physics Research Section B: Beam Interactions with Materials and Atoms*, 219:110–114, 2004.

[80] CE Cox, BG Lowe, and RA Sareen. Small area high purity germanium detectors for use in the energy range 100 ev to 100 kev. *IEEE Transactions on Nuclear Science*, 35(1):28–32, 1988.